UNIVERSITY of CALIFORNIA
Santa Barbara

Characterizing Structure and Properties of Woven Ceramic Matrix Composites

A Dissertation submitted in partial satisfaction of the
requirements for the degree

Doctor of Philosophy
in
Materials

by

Michael Nicholas Rossol

Committee in charge:

Professor Frank W. Zok, Chair
Professor Carlos G. Levi
Professor Matthew R. Begley
Professor Tresa M. Pollock

March 2015

The dissertation of Michael Nicholas Rossol is approved.

Professor Carlos G. Levi

Professor Matthew R. Begley

Professor Tresa M. Pollock

Professor Frank W. Zok, Committee Chair

March 2015

Characterizing Structure and Properties of Woven Ceramic Matrix Composites

by

Michael Nicholas Rossol

for Rachel

Acknowledgements

I would like to acknowledge and thank: the Pratt & Whitney Center for Excellence in composites for funding; the National Hypersonics Science Center for providing material and funding for the work on characterizing weave variability; David Marshall and Brian Cox for their help, support, and insightful discussions; David Poerschke for all of his help with the FIB and TEM, as well as insightful discussions regarding intermediate temperature oxidation; my committee members for their insightful comments and suggestions, and always providing an open door for questions; and most importantly my advisor, Frank Zok, for providing the guidance, but also the freedom to develop my unique strengths.

I would like to thank: Varun Rajan and John Shaw for being phenomenal collaborators and friends, their help in lab and out was invaluable; Noah Philips for his mentorship and friendship; Brett Compton, Nell Gamble, Tony Fast, Matthew Blacklock, Renaud Renaldi, and Mark Novak for their help and insights; Pete Maxwell, Mark Cornish, and Deryck Stave for their technical support; and Kirk Fields for his limitless help and insights regarding mechanical testing and his companionship on (and off) the tennis courts.

Finally, I would like to thank all of the my wonderful friends and family, both new and old, for their unconditional love and support. In particular: my parents, Ed Rossol and Jean Lowe, for instilling in my a desire to learn and a love of challenges; my brothers (full and half), Scott, Josh, Paul, Sam, and Aron, for their never-ending companionship and friendship; Beth, Michael, and Ariana, for welcoming me into your family with open arms; and most importantly, my wife, Rachel, for her endless love and support, I could not have done this without her.

Curriculum Vitæ

Michael Nicholas Rossol

Education

2005–2009	B.S. in Materials Science and Engineering University of Washington Seattle, WA
2009–2015	Ph.D. in Materials University of California, Santa Barbara Santa Barbara, CA

Publications

M. N. Rossol, D. L. Poerschke, and F. W. Zok. Intermediate Temperature Embrittlement in SiC/SiCN Composites with Polymer-Derived Matrices, *In preparation*.

J. H. Shaw, **M. N. Rossol**, D. B. Marshall, and F. W. Zok. Effects of Warp Wavelength on Damage and Failure in an Angle-Interlock C/SiC Composite, *In preparation*.

J. H. Shaw, **M. N. Rossol**, D. B. Marshall, and F. W. Zok. Effects of Preform Shear on Tensile Properties of a Woven C/SiC Composite, *In Preparation*.

M. N. Rossol, V. P. Rajan, and F. W. Zok. Effects of Weave Architecture on Mechanical Response of 2D Ceramic Composites, *Submitted to Composites Part A, December 2014*.

M. N. Rossol, T. Fast, D. B. Marshall, B. N. Cox, and F. W. Zok. Characterizing In-Plane Geometrical Variability in Textile Ceramic Composites. *In press, Journal of the American Ceramic Society*.

J. H. Shaw, **M. N. Rossol**, D. B. Marshall, and F. W. Zok. Effects of Tow-Scale Holes on the Mechanical Performance of a 3D Woven C/SiC Composite. *In press, Journal of the American Ceramic Society*.

V. P. Rajan, J. H. Shaw, **M. N. Rossol**, and F. W. Zok. An Elastic-Plastic Constitutive Model for Ceramic Composite Laminates. *Composites Part A*, 66:44–57, 2014.

B. N. Cox, H. A. Bale, M. Begley, M. Blacklock, B. C. Do, T. Fast, M. Naderi, M. Novak, V. P. Rajan, R. G. Rinaldi, R. O. Ritchie, **M. N. Rossol**, J. H. Shaw, O. Sudre, Q. Yang, F. W. Zok, and D. B. Marshall. Stochastic Virtual Tests for High-Temperature Ceramic Matrix Composites. *Annual Review of Materials Research*, 44:479–529, 2014.

R. R. Collino, N. R. Phillips, **M. N. Rossol**, R. M. McMeeking, and M. R. Begley. Detachment of Compliant Films Adhered to Stiff Substrates via Van Der Walls Interactions: Role of Frictional Sliding during Peeling. *Journal of the Royal Society Interface*, 11(97), 2014.

M. N. Rossol, J. H. Shaw, H. Bale, R. O. Ritchie, D. B. Marshall, and F. W. Zok. Characterizing Weave Geometry in Textile Ceramic Composites Using Digital Image Correlation. *Journal of the American Ceramic Society*, 96(8):2362–2365, 2013.

V. P. Rajan, **M. N. Rossol**, and F. W. Zok. Optimization of Digital Image Correlation for High-Resolution Strain Mapping of Ceramic Composites. *Experimental Mechanics*, 52(9):1407–14215, 2012.

A. Cooper, N. Bhattarai, F. M. Kievit, **M. N. Rossol**, and M. Zhang. Electrospinning of Chitosan Derivative Nanofibers with Structural Stability in an Aqueous Environment. *Physical Chemistry Chemical Physics*, 13(21):9969–9972, 2011.

Abstract

Characterizing Structure and Properties of Woven Ceramic Matrix Composites

by

Michael Nicholas Rossol

Ceramic matrix composites (CMCs) with woven fibers are of interest for aerospace applications due to their low density, high strength and melting temperature, as well as broad flexibility in placement of fiber tows to match anticipated stress fields. Even when placed according to design, tows experience non-uniformities in stresses and strains due to their waviness. The added complexity of constructing complex weaves can further lead to undesirable variability in the weave structure. The present study seeks to extend the current understanding of structure-property relations in woven CMCs.

It begins with the implementation of 3D digital image correlation (DIC) to characterize full-field strains and displacements with sub-tow spatial resolution. This enables the characterization of strain heterogeneities that develop in woven CMCs. 3D DIC is extended to characterize the variability in tow placement within 3D weaves. This variability exists at both short- and long-

wavelengths. Short-wavelength variations are intrinsic to the weaving process and result in local variations in the packing density of the tows. Long-wavelength variations are attributed to shear deformation during handling after weaving. Discrete Fourier transforms of the intrinsic variations are used to provide a statistical representation of the weave structure. Using these statistics, along with the Monte Carlo method, virtual specimens are generated.

The effects of weave structure on surface strain evolution are investigated experimentally on a SiC/SiC CMC and through a meso-scale finite element model. Experimentally, strain elevations and failure initiation are observed on wavy segments of surface tows. Model predictions show similar features and indicate that strains are elevated in response to bending and straightening of the wavy tow segments. Tow straightening is accommodated by out-of-plane motion of the tows and can be suppressed to some extent by the underlying (sub-surface) plies. The constraint in the present material is low, because of porosity and micro-cracks present in the matrix-rich regions between the plies.

Additionally, the study addresses the intermediate temperature embrittlement phenomenon endemic to SiC/SiC CMCs, in both water vapor and dry air environments. Oxidant ingress occurs through existing porosity and micro-cracks in the matrix, prior to the formation of stress-induced matrix damage. This process is sluggish, reducing the oxidant activity within the composite,

resulting in preferential oxidation of the Si-based constituents prior to the BN fiber coating. These findings are in contrast to the current understanding in the literature.

Contents

List of Figures

Chapter 1

Introduction

1.1 Materials for aerospace applications

Fiber-reinforced ceramic matrix composites (CMCs) are of interest for aerospace applications because of their low density, high hardness and strength, and high melting temperature. Implementing them into gas turbine aero-engines would enable higher operating temperatures and significant weight reductions. This would lead to greater thermodynamic efficiency and reduced fuel consumption (Eldrid et al., 2001).

Broadly, CMCs can be categorized on the basis of the composition of the constituent fibers. Three types of fibers are commonly used: oxide, SiC, and C.

Oxide fibers are used with oxide matrices. Nextel$^{\mathrm{TM}}$ 610 and Nextel$^{\mathrm{TM}}$ 720 are the highest performing oxide fibers. Respectively, they are made from nominally pure alumina and alumina mullite mixtures. Oxide matrices are most commonly made of alumina, mullite, and/or silica. The upper use temperature of oxide/oxide CMCs is limited by the creep-resistance and the thermal stability of the fibers. Nextel$^{\mathrm{TM}}$ 610 fibers can be used up to 1000 °C (Epstein, 2013), whereas Nextel$^{\mathrm{TM}}$ 720 fibers can be used up to 1200 °C (Marshall and Cox, 2008). Oxide/oxide CMCs are more resistant to oxidation than SiC based composites. They have found several commercial applications. For example, oxide/oxide CMCs are being used to make the center body and mixer (Figure 1.1(a)) in General Electric's (GE's) Passport 20 engine, scheduled to enter service in 2016 (Epstein, 2013). They are also being used to make the exhaust nozzle for Boeing's 787 Dreamliner (Figure 1.1(b)) (Wood, 2013), which began test flights in 2014.

SiC fibers are most commonly used with SiC matrices. They come in several grades, with varying concentrations of oxygen and residual C. They have higher temperature capabilities than oxide fibers (up to $\sim$ 1500 °C). SiC/SiC CMCs are of interest for the hottest regions of aero-engines, where operating temperatures are between 1200° and 1400 °C. In this temperature range, the specific strength of SiC/SiC CMCs is about twice that of oxide/oxide composites and metallic superalloys (Figure 1.2). The first commercial application for SiC/SiC CMCs will be in GE's Leading Edge Aviation Propulsion (LEAP) engine, expected to start test flights in 2016 (Wood, 2013). The LEAP engines will contain high-pressure turbine shrouds made from SiC/SiC CMCs. The weight of these shrouds is about one-third that of corresponding nickel-superalloy shrouds. SiC/SiC CMCs have also been used to make turbine blades that have been tested in the F414 military jet engine in 2000 (Wood, 2013).

Carbon fibers are most commonly used with SiC matrices. They generally exhibit the highest temperature capabilities (in inert environments), highest specific strength (Figure 1.2), and have the lowest cost, but are the least resistant to oxidation. C/SiC CMCs are of interest in short-term, very high temperature applications, such as for rocket nozzles or hypersonic flight vehicles (Marshall and Cox, 2008).

The materials of principal interest in this study are SiC/SiC and C/SiC CMCs. These materials are made using a variety of routes. In all cases, fiber coatings are first deposited, primarily using chemical vapor infiltration (CVI), to ensure a weak bond between fiber and matrix. Thin pyrolytic-C coatings are used on C fibers. BN-based coatings are more resistant to oxidation and are preferred for SiC fibers. The matrices are produced by one of three main routes: CVI, polymer impregnation and pyrolysis (PIP), and melt infiltration (MI). CVI matrices are pure, strong, and hermetic, but contain substantial internal porosity. The porosity is formed as internal spaces become pinched off, preventing further infiltration of the precursor gas. PIP-derived matrices are formed by impregnating the fiber preform with a preceramic polymer. The preceramic polymer is then pyrolyzed to form a ceramic matrix. The process is amenable to existing infiltration methods developed by the polymer matrix composite community. The chemistry of the preceramic polymer can be tailored to produce a variety of Si-based matrices (e.g., SiC, SiCN, Si_3N_4). In SiC/SiC composites, PIP-derived matrices are used in the amorphous state, largely because current SiC fibers cannot withstand the temperatures needed to crystallize the matrices. The preceramic polymers have a low volumetric yield ($\sim$ 30 %)(Naslain, 2004) and thus produce a porous, micro-cracked matrix. Multiple impregnation cycles are needed to obtain the desired matrix densities. The number of cycles can be reduced by incorporating SiC particles during the first impregnation cycle. But even after numerous PIP cycles the matrices still contain residual porosity and micro-cracks. In MI, partially processed composites are infiltrated with molten Si. For example, MI is used with PIP processed CMCs. In reactive melt infiltration, C is added to the matrix with the expectation that it will react in-situ with the molten Si to form SiC. Although the resulting matrices contain little porosity, they invariably contain residual Si. The residual Si limits the upper use temperature to its melting temperature (1414 °C).

Ceramic matrix composites can also be categorized on the basis of *fiber* *architecture*. There are two broad groups: laminates and woven composites. Laminates are made up of sheets of unidirectional fibers. The sheets are stacked, or layed-up, with the desired fiber orientations. Often the sheets are pre-mixed with matrix material, or a matrix precursor, to create a ”prepreg”. Prepregs help to maintain the fiber orientation during lay-up. Laminates are most commonly used for parts with simple shapes, such as flat sheets or parts with large radii of curvature.

Woven composites consist of fiber tows woven together in two or more directions. Relative to their laminated counterparts, woven composites provide increased flexibility for fiber placement to best match the anticipated thermal and mechanical stress fields. Two-dimensional woven composites consist of layers of woven fabrics (e.g., plane and satin weaves). Woven fabrics can be shipped, stored, draped, and pressed into shape prior to the addition of the matrix (Cox and Flanagan, 1997). They provide consistency in fiber placement and orientation, particularly when making parts with complex shapes, such as parts with small radii of curvature.

Three-dimensional woven composites contain reinforcing fibers both in-plane and through-thickness. The weaves consist of layers of straight tows held together by tows woven layer-to-layer or through thickness (e.g., angle interlock and orthogonal weaves). The through-thickness weavers mitigate delamination failures and can enhance heat flow in high heat flux applications (Cox and Flanagan, 1997). Indeed, thin woven C/SiC composites have been demonstrated to sustain temperature gradients exceeding $1000\,\mathrm{K\,mm^{-1}}$ without failure (Marshall and Cox, 2008).

Advances in textile manufacturing have enabled 3D weaving of net-shape parts, such as the integrally woven rocket nozzle tubes shown in Figure 1.3(c-d) (Marshall and Cox, 2008). The tubes are woven by passing tows from the hot section of one tube to the cold section of the next. This prevents separation of neighboring tubes, as well as splitting apart of the hot and cold sections of individual tubes. The weave is designed to support the high internal pressures in the tubes; the fibers follow the maximum principal stress directions and are in proportions that correspond to the ratio of these stresses (2:1 in cylindrical tubes). Three-dimensional weaves also allow for integral forming of holes or slots (for cooling, for example) without cutting fibers (Figure 1.3(a-b)), as well as for integral attachment to other structural elements (Figure 1.3(d)) (Marshall and Cox, 2008).

With increasing weave complexity comes the possibility of increasing defects in tow trajectories and shapes. The nature of these defects and their effects on thermomechanical performance represent key issues that must be addressed in order for these composites to be successfully implemented in critical components.

1.2 Outstanding issues in damage and failure prediction

The mechanics of cracking and fracture in *laminated* CMCs with fully dense matrices is well understood. Comprehensive models and analyses have been developed to describe: *(i)* the onset of matrix cracking in unidirectional CMCs in tension and/or shear (Aveston et al., 1971; Budiansky et al., 1986; Rajan and Zok, 2014); *(ii)* crack tunneling in transverse plies of cross-ply laminates and penetration of those tunneling cracks into axial plies (Xia and Hutchinson, 1994; Xia et al., 1993); and *(iii)* fiber fragmentation, fiber pullout and composite fracture (Curtin, 1991, 1999; Hui et al., 1995). Complementary experimental efforts have been undertaken to validate some of these models (Beyerle et al., 1992a,b; Cady et al., 1995).

Extending the mechanics frameworks developed for laminated composites to *woven* composites presents a number of challenges. Foremost among them are the non-uniformities of stress and strain that arise in wavy tows even under macroscopically-uniform loadings. Using full-field displacement mapping techniques, non-uniformities in strain and their correlation to the underlying weave features have been measured for a number of CMCs, including eight-harness satin weave SiC/SiC (Berbon et al., 2002; Rajan et al., 2014), 3D orthogonal C/C (Qin et al., 2012), and angle-interlock C/SiC (Shaw et al., 2014a). One implication of spatially varying strains is that failure may initiate prematurely, relative to laminated composites, within the most heavily strained regions of the composite. Such effects may be exacerbated by microstructural inhomogeneities within the matrix. In woven CMCs made by PIP, pores and micro-cracks are present over a wide range of length scales, from micrometers between fibers within the tows to a significant fraction of a mm between plies. Analytical approaches of the type developed for laminated composites are difficult to satisfactorily extend to wavy tows and heterogeneous matrices; further progress in predicting deformation and failure can only be made with the use of computational models.

Computational models of woven CMCs need to be able to predict strains at the same size scale as the weave architecture, i.e., at both the unit-cell and tow scales. One approach is the binary model (Cox et al., 1994; Xu et al., 1995). In the binary model, the axial properties of the tows are represented by line elements. The line elements are then embedded in an effective medium. The effective medium represents the matrix, including any porosity, and the transverse properties of the tows. The binary model has been demonstrated to predict strain non-uniformity corresponding to the underlying weave architecture (Flores et al., 2010; Yang and Cox, 2010), but is limited to the prediction of strains at length scales larger than the tow dimensions. Experimental results indicate that crack initiation and propagation in CMCs is governed by the tow geometry (Berbon et al., 2002). Therefore, meso-scale models, in which the tows are modeled explicitly (Cox et al., 2014; Lomov et al., 2000, 2001), are needed.

Some progress in understanding effects of weave architecture on strain variations has been made through studies on *polymer* matrix composites, with both satin and twill weaves (Daggumati et al., 2011; Ivanov et al., 2009; Lomov et al., 2008; Nicoletto et al., 2009). Surface strains, measured by digital image correlation, were found to be greatest at locations at which tows cross one another and lowest in adjacent matrix-rich pockets. The results were compared with predictions of a 3D elastic meso-scale finite element model. Elements within the tows were treated as being transversely isotropic with elastic properties equivalent to those of a comparable unidirectionally-reinforced composite, whereas elements outside the tows were assigned elastic properties matching those of the matrix resin. Although the FE predictions yielded results that were qualitatively consistent with the measurements, the magnitude and distribution of surface strains were found to depend strongly on the number and orientation of underlying plies. Effects of matrix plasticity on these distributions have yet to be investigated.

SiC/SiC CMCs are susceptible to embrittlement at intermediate temperatures (700–900 °C), failing at stresses below that of materials tested at lower or higher temperatures. In this temperature regime, silica formation is sluggish and does not readily seal off preexisting porosity or open matrix cracks. This enables the ingress of oxidants (O_2 and H_2O), leading to oxidation of the fiber coatings. Oxidation of C coatings leaves a gap, exposing the fibers to oxidation (Eckel et al., 1995). BN-based coatings oxidize to form boria. Boria is liquid above 450 °C and has been shown to react with neighboring SiC and/or SiO_2 to form a borosilicate glass (Jacobson et al., 1999a). Boron is easily volatilized in environments containing water vapor. This leads to recession of the BN coatings (Figure 1.4(a)), exposing the fibers to oxidation, and the conversion of borosilicate to silica (Jacobson et al., 1999b). Silica is less permeable to oxidants but more viscous than borosilicate glass. Intermediate temperature embrittlement has been investigated for a variety of systems, from bare fiber tows to woven composites. The key experimental findings follow.

Static stress-rupture tests have been performed on SiC-fiber tows between 500° and 800 °C (Forio et al., 2004; Gauthier and Lamon, 2009; Gauthier et al., 2009; Lamon and R'Mili, 2012). Rupture times for tows tested in dry air decreased with increasing temperature and load; delayed failure did not occur in pure nitrogen. Tests were performed on fibers with varying free-C concentration, e.g., Hi-Nicalon^{TM}, with 17 % free C, and Hi-Nicalon^{TM} Type S, with 3 %

free C. Rupture times decreased with increasing free C.

Morscher (1997) performed stress-rupture tests on mini-composites made of a single tow of SiC fibers, BN fiber-coatings, and a CVI-SiC matrix. Mini-composites were tested between 700° and 1200 °C in ambient air. Gaps where the BN layer resided were found between the fibers and the matrix in samples tested at 700 °C, indicating boron volatilization and BN recession. In these samples the in-situ fiber strengths were measured from the size of the fiber fracture mirrors. The results indicated that the average fiber strength was reduced with respect to the room temperature strength. Embrittlement was more severe for samples tested at 900 °C. In these samples, silica formation was observed between the fibers and the matrix. The fiber fracture mirrors emanated from these silica regions. At 1200 °C the composite response was controlled by fiber creep.

Similar results have been obtained on woven SiC/SiC CMCs (Morscher et al., 2000; Ogbuji, 1998, 2003). In woven SiC/SiC CMCs, rupture strengths and times for specimens tested between 800° and 900 °C were reduced with respect specimens tested are room temperature. Silica was observed to form between closely packed fibers. As in the mini-composites, the origins of the fiber fracture mirrors corresponded to the silica-containing regions.

Several theories have been postulated to explain intermediate temperature embrittlement in SiC/SiC CMCs. The first theory proposes that embrittlement occurs due to oxidation-induced slow-crack growth in the fibers (Forio et al., 2004; Gauthier et al., 2009; Lamon and R'Mili, 2012). Two mechanisms contributing to slow-crack growth in the fibers are hypothesized. The first is oxidation of residual C at the SiC grain boundaries which leads to the formation of fine intergranular cracks. The second is the subsequent oxidation of these grain boundaries to form silica (Figure 1.4(d)) (Gauthier et al., 2009). Because of the molar volume increase associated with the conversion of SiC to silica, the intergranular silica scale is expected to "wedge" these cracks open. The proposed mechanisms are consistent with rupture occurring in environments containing oxygen, and with reduced rupture times for fibers with greater free-C concentrations.

In a second theory, Xu et al. (2014) hypothesize that silica formation on the fibers surface generates growth stresses in the fibers (Figure 1.4(b)). As with the intergranular cracking mechanism, the stresses arise mainly from the molar volume expansion during oxidation (the ratio of the molar volumes of SiO_2 and SiC is about 1.8). Upon formation, the SiO_2 scale is under compression, inducing tension in the fibers. The tensile stress in the fibers increases with the oxide thickness. Simultaneously, the SiO_2 relaxes due to viscous flow. The extent of stress elevation in the fibers is dictated by the competing rates of oxide growth and viscous flow, both of which are temperature dependent.

Calculations by Xu et al. (2014) indicate that the oxide-induced tensile stress can reach a significant fraction of the fiber strength over oxidation periods of 10^3–10^4 hours, with the largest stresses developing at temperatures between 800° and 900 °C. The predicted rupture times associated with this mechanism were found to overestimate the values that had been obtained experimentally by Gauthier and Lamon (2009). This suggests the possibility of multiple degradation mechanisms.

A third theory postulates that, in SiC/SiC composites, the resulting silica bonds the fiber to the matrix, inhibiting further slip and causing stress concentrations (Glime and Cawley, 1998; Morscher and Cawley, 2002). The theory is consistent with the observations that fiber fracture frequently initiates adjacent to locations of silica formation. Although activation of the proposed stress concentration requires a change in applied stress, premature failure has been found both in residual strength tests following oxidation (Ogbuji, 1998), and during static loading (Morscher, 1997; Morscher et al., 2000). Morscher (1997) proposed that during stress-rupture tests, the requisite change in stress occurs when some fibers fail independently (perhaps via the mechanisms described previously), thereby increasing the load on the remaining fibers.

A fourth theory, proposed by Xu et al. (2014), hypothesizes that oxidation can continue at the fiber/oxide interface even after the entire gap has been filled. In this case, the volume expansion accompanying the transformation of SiC to silica causes a ”wedging” effect that intensifies the stress in the fiber (Figure 1.4(c)). A model for the stress-intensity factor indicates that time to fracture is non-monotonic. The minimum time to fracture is predicted to occur at temperatures between 840° and 940 °C, dependent on the applied stress. The model also predicts a threshold temperature (between 900° and 1000 °C), above which fracture should not occur.

Most of the experimental studies and the corresponding theories outlined above have focused on oxidation in dry, ambient air environments. Yet it has been shown in other studies that the oxidation rate of SiC in *water vapor* can be an order-of-magnitude greater than that in dry air (Opila, 1999). This is expected to have significant implications on the lifetimes of composites in combustion environments, where water vapor contents are typically 5 % to 10 % (Jacobson et al., 2001).

These experimental studies have focused primarily on CMCs with CVI or MI matrices. These matrices are expected to be hermetic in their as-processed state and hence prevent ingress of oxidants; oxidant ingress can only occur after the matrix cracks. Indeed, some studies have shown that a well-defined threshold for embrittlement is obtained *at* the matrix cracking stress (Heredia et al., 1995). PIP-based matrices, in contrast, contain open porosity and micro-cracks after processing. This raises the possibility of internal oxidation even in the absence of an applied stress. Intermediate temperature embrittlement in PIP-based CMCs has yet to be investigated.

1.3 Dissertation objectives and outline

The goal of the present study is to improve the understanding of the meso-scale structure of fiber reinforcements and the mechanical and thermochemical properties of 2D and 3D woven CMCs. Three specific topics are addressed: *(i)* development and implementation of new techniques to characterize the structure and mechanical response of woven CMCs; *(ii)* effects of weave architecture on damage initiation and evolution in woven CMCs; and *(iii)* understanding the intermediate temperature oxidation and embrittlement of PIP-based SiC/SiC CMCs.

The dissertation is organized in the following way. In Chapter 2, the application of 3D digital image correlation (DIC) to the measurement of full-field strains and displacements in CMCs is examined. Guidelines for proper selection of correlation parameters (subset, step, and filter sizes) is discussed in terms of their effects on strain and displacement errors. Methods for identifying and characterizing surface cracks using DIC are also introduced. Preliminary experimental studies reveal a strong correlation between the locations of surface cracks and characteristic features of the underlying weave architecture. These correlations are investigated in greater detail in Chapter 3.

In Chapter 3, a meso-scale finite element model is developed and calibrated to uniaxial tension tests on a commercial 2D-woven SiC/SiCN CMC. The model is used to probe distributions in surface strains and fiber stresses. The effect of straightening of the wavy tow segments and the constraint of underlying plies are also examined.

Recognizing the potential importance of tow placement in the onset of damage, the attention in Chapter 4 is directed to the characterization of weave defects. Here, a non-destructive characterization technique based on 3D DIC is developed and demonstrated on a 3D woven CMC. Weave defects are identified using measurements of small variations in tow locations relative to that of an ideal weave. The technique is shown to be amenable to large panels of material. The technique is employed to probe a variety of weave features, including holes and shear defects.

In Chapter 5, an experimental study of intermediate temperature oxidation and embrittlement of a 2D woven SiC/SiCN composite with a PIP-derived matrix in a water vapor containing environment is described. Oxidant ingress is found to occur readily, through pre-existing pores and micro-cracks, even in the absence of an applied stress. Detailed fractrography and ceramatography provide insights into the embrittlement mechanisms. Finally, key findings and opportunities for future work are discussed in Chapter 6.

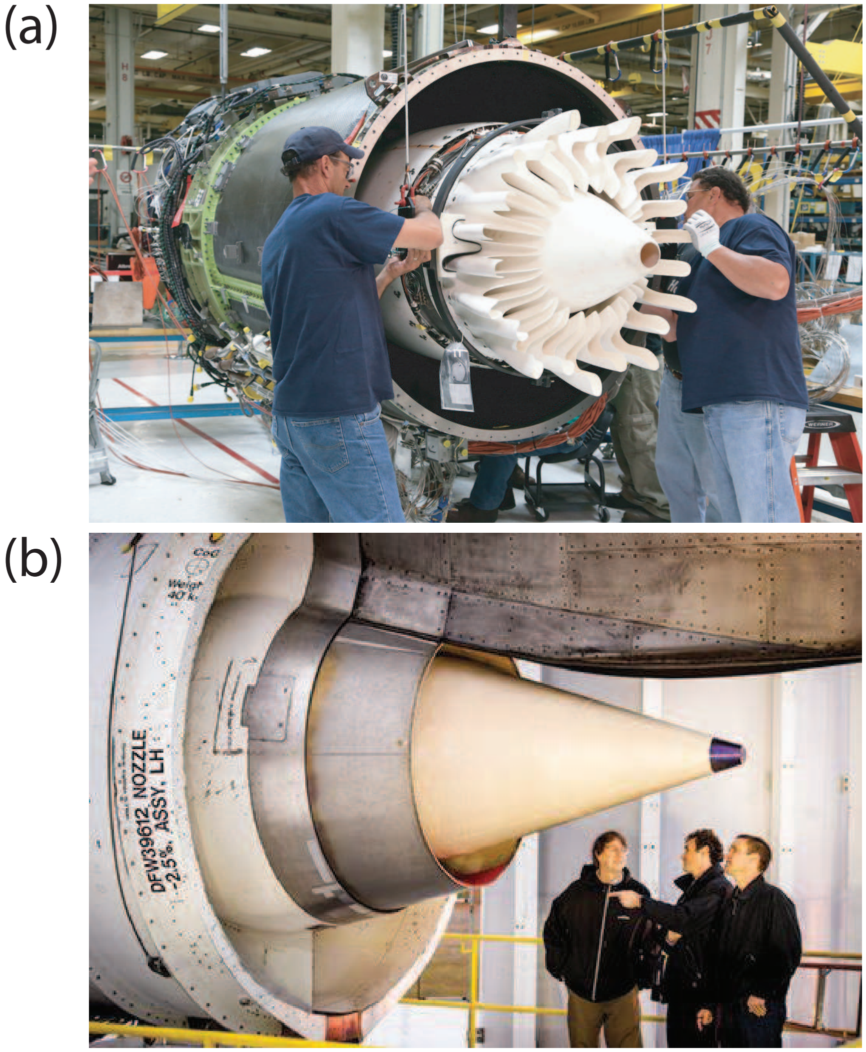

Figure 1.1: Oxide/oxide CMCs in commercial engines: (a) mixer and center body assemblies in General Electric's Passport 20 engine (Eldrid et al., 2001); (b) exhaust nozzle for the Boeing 787 Dreamliner (Wood, 2013).

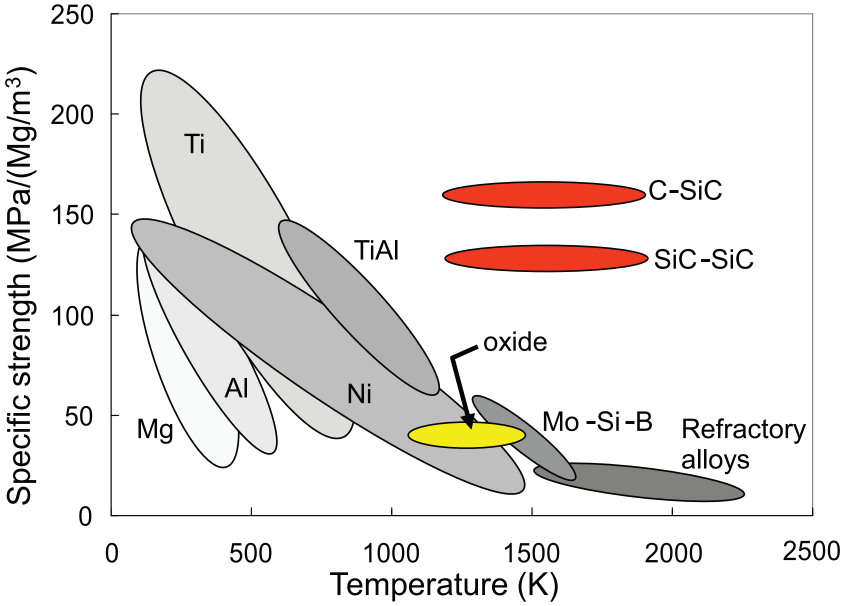

Figure 1.2: Candidate materials for aerospace applications. SiC based CMCs offer the greatest specific strength at the operating temperatures of interest (Marshall and Cox, 2008).

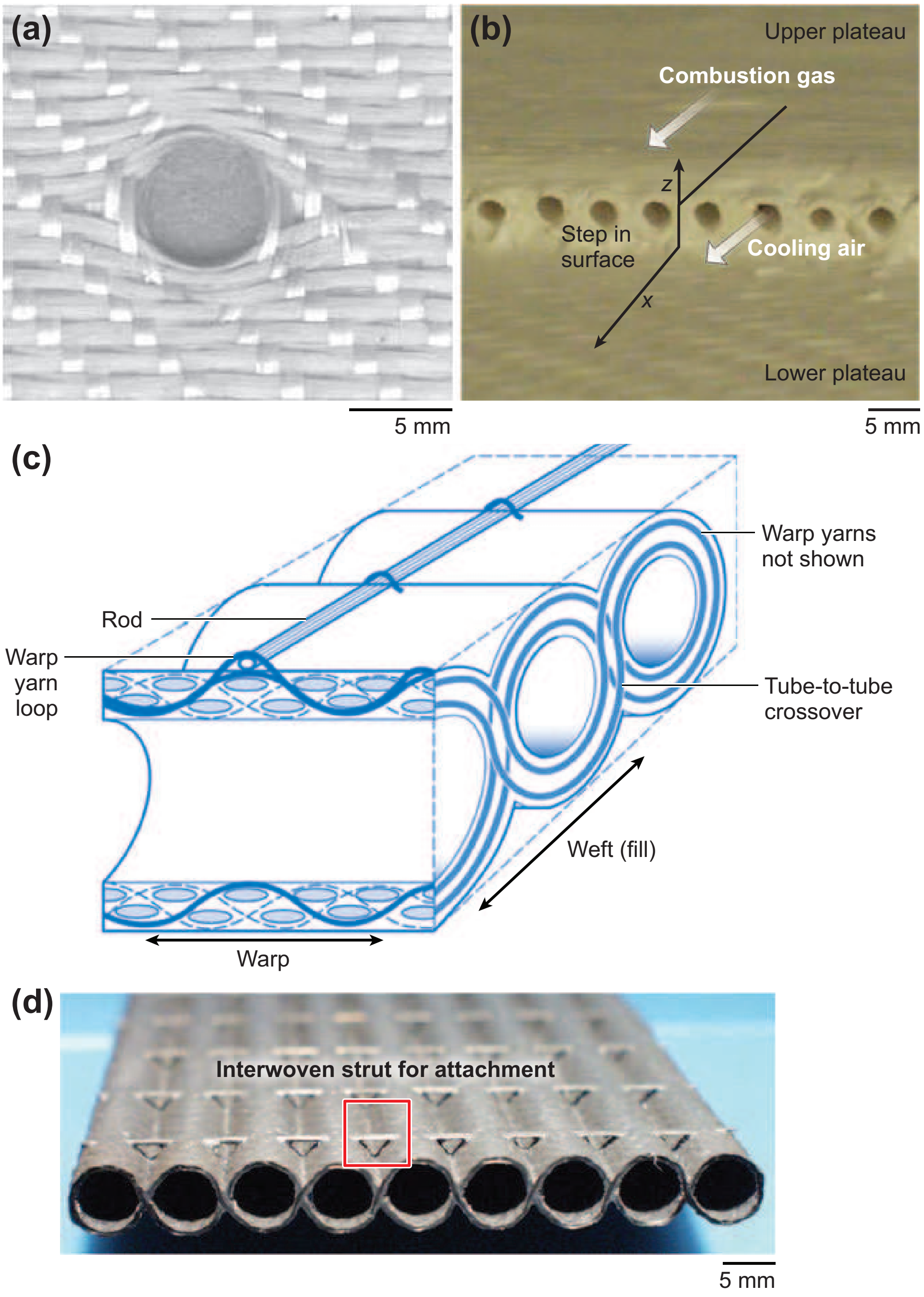

Figure 1.3: Examples of 3D woven structures: (a) a large hole woven into an angle-interlock preform; (b) cooling holes in a composite liner, created by inserting rod-shaped mandrels through the preform prior to matrix processing; (c) schematic of and (d) fully processed C/SiC composite rocket nozzle tubes woven to net-shape, including integrally woven struts to connect tubes to the rocket body (Marshall and Cox, 2008).

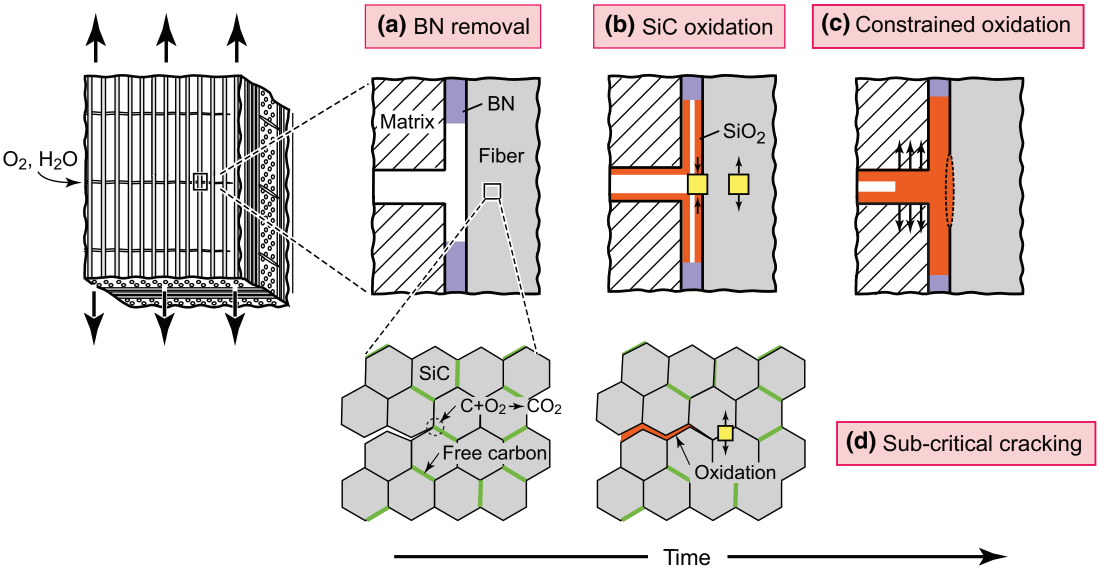

Figure 1.4: Schematic of proposed embrittlement mechanisms in SiC/SiC composies: (a) Process begins with removal of the fiber coating via oxidation (C coatings) or oxidation/volatilization (BN coatings); (b) oxidation of the fiber surface creates growth stresses in the fiber; (c) filling of the gap between fiber and matrix cause a stress concentration by fusing the fiber to the matrix or due to continued oxidation of the fiber; or (d) slow-crack growth in the fiber caused by oxidation along the grain boundaries (Xu et al., 2014).

Chapter 2

Full-field displacement and strain mapping of ceramic composites using digital image correlation

---

This chapter is adapted from a peer-reviewed publication: V. P. Rajan, M. N. Rossol, and F. W. Zok. Optimization of Digital Image Correlation for High-Resolution Strain Mapping of Ceramic Composites. *Experimental Mechanics*, 52(9):1407–14215, 2012. Available at: `http://dx.doi.org/10.1007/s11340-012-9617-1`

2.1 Introduction

As discussed in Chapter 1, extending the existing mechanics frameworks to woven CMCs requires characterization of the strain non-uniformity associated with the tow waviness. Conventional measurement techniques (e.g., strain gages and extensometers) are often inadequate, for three principal reasons.

First, strain distributions in woven fiber composites can be highly heterogeneous and dependent on the weave architecture (Cox and Flanagan, 1997). The local strains in a fiber tow are influenced by numerous factors, including: the orientation of the tow with respect to the loading axis; the amplitude of out-of-plane tow undulation; the local 'environment' around the tow, characterized by the arrangement of neighboring tows and matrix; and the elastic/fracture properties of the composite constituents. Furthermore, the strains are expected to vary spatially over a length scale comparable to the tow dimensions. To formulate high-fidelity models of composite damage and failure, it is necessary to find the maximum strain values at the tow level. The implication is that strains must be resolved spatially at a length scale *smaller* than that of the tows.

Second, strain variations arise in the presence of structural features such as holes or notches. In these cases, the gauge length for strain measurement must be less than the smallest characteristic dimension of the structural feature. Strain gauges and extensometers lack the requisite spatial resolution to meet these requirements in most cases of practical interest.

Third, the mechanical behavior of ceramic composites must be understood at temperatures representative of the targeted service conditions (1200–1500 °C). Although contacting extensometers can be used to obtain global strains, only non-contact methods are viable for measuring strain variations in this domain.

Digital image correlation (DIC) is a non-contact optical technique used to measure surface displacements and strain fields of a test specimen subjected to an external stimulus (load, temperature, etc.) (Sutton et al., 2000). Displacements are obtained by imaging a speckle pattern on the specimen surface during the test and subsequently correlating each image of the deformed pattern to that in the undeformed state (Sutton et al., 2009). Strains are obtained by differentiating displacement fields. The technique combines sub-pixel displacement accuracy (Schreier and Sutton, 2002) with excellent spatial resolution, allowing strains to be measured to within 10^{-4} or less (Ke et al., 2011). In principle, these attributes make DIC eminently suitable for probing strain distributions in woven ceramic fiber/ceramic matrix composites.

Numerous studies have utilized digital image correlation to understand the mechanical behavior of fiber composites (Bisagni and Walters, 2008; Fuchs and Major, 2010; Kazemahvazi et al., 2010; Lagattu et al., 2004; Orteu et al., 2007; Pankow et al., 2011; Ramault et al., 2010). Two recent studies (Anzelotti et al., 2008; Daggumati et al., 2011) have incorporated DIC to examine the mechanical behavior of a 2D C-fiber polymer matrix composite. They confirm the expected features: notably, the heterogeneity of strains at intra-tow and inter-tow length scales as well as the periodicity of strains and its intimate relationship to the fiber architecture. They also demonstrate the suitability of DIC for measuring local strains with high accuracy and spatial resolution.

Two additional important issues have been raised in these and other papers. First, there are inherent trade-offs between spatial resolution and displacement accuracy. Second, there is complex interplay between displacement error, strain error, and the parameters chosen for the speckle pattern, image correlation and strain calculation (Avril et al., 2008; Bornert et al., 2009; Ke et al., 2011; Knauss et al., 2003; Robert et al., 2007; Schreier and Sutton, 2002; Sutton et al., 2000; Wang et al., 2011). Although several studies have attempted to quantify these relationships, most have been limited to correlation errors arising from rigid body translations (Haddadi and Belhabib, 2008; Robert et al., 2007) or no motion at all (Ke et al., 2011). Simulated experiments in which displacements are applied numerically to a computer-generated image have also been conducted (Avril et al., 2008; Bornert et al., 2009; Schreier and Sutton, 2002; Schreier et al., 2000). The latter results represent best-case scenarios since they neglect experimental errors caused by camera vibration, imperfect image contrast, etc.

The overarching objective of this chapter is to establish a framework for design and analysis of DIC experiments that yield high-fidelity strain measurements in woven CMCs. This is accomplished by: *(i)* identifying and analyzing sources of displacement and strain error in mechanical tests that produce uniform strains as well as strain gradients; *(ii)* formulating analytic relationships between these errors and applied strain, speckle size, and DIC algorithm parameters; and *(iii)* utilizing the results to design experiments to probe strain variations in a ceramic composite with the requisite spatial resolution.

The outline of the chapter is as follows. First, the principles of digital image correlation are reviewed. Next, test results on a baseline (homogeneous) material (Al 6061-T6) are analyzed to determine the relationships between displacement and strain error and the DIC algorithm parameters. Three specimen geometries are considered: one with nominally uniform strain (uniaxial tension) and two with strain gradients (open-hole and center-notched tension). Because the latter geometries yield different strain gradients as well as different length scales for strain variation, they provide useful insights and guidance on the feasibility of measuring strain gradients and small-scale strain heterogeneities in woven composites. This part of the study complements previous work focused on errors arising from rigid body motions (Haddadi and Belhabib, 2008; Ke et al., 2011; Robert et al., 2007). Finally, a case study illustrates how the preceding analyses can be used to design tests on a SiC/SiC composite. In addition to revealing the effects of fiber architecture on strain distributions, the tests are used to probe the initiation and growth of cracks. To this end, displacement fields found via digital image correlation are analyzed to locate cracks and measure their opening displacements. Such measurements are crucial for calibrating models of crack bridging in fiber composites.

2.2 Error analysis

2.2.1 Digital image correlation

In-plane surface displacements are measured by tracking the deformation of a speckle pattern through a series of digital images acquired during a mechanical test. If the out-of-plane displacements of the sample are negligible, a single (stationary) camera can be used. Otherwise, to measure out-of-plane displacements and to correctly extract in-plane displacements, stereo images (from two cameras) must be employed. The correlation algorithm attempts to locate a *subset* of the image of the undeformed pattern corresponding to a subset in the image of the deformed pattern. In mathematical terms, it seeks to find (Sutton et al., 2009):

$$\underset{\mathbf{p}}{\arg\min} \sum_{\mathbf{x}\,\in\,\text{Subset}} \left(G(\xi(\mathbf{x},\mathbf{p})) - F(\mathbf{x})\right)^2 \tag{2.1}$$

where G and F are the grayscale intensity values of the deformed and undeformed subsets, respectively; ξ is the shape function that describes the deformation between the subsets; and $\mathbf{p}$ comprises the parameters of the subset shape function, chosen to minimize the *sum of squared differences* (SSD) between grayscale intensity values in the two corresponding subsets (Sutton et al., 2009). The DIC software used in this work (Vic-3D, Correlated Solutions) provides the option of using more complex correlation schemes; these include center-weighting of the sum in Equation 2.1 and accounting for changes in intensity values between images (offsets and scaling). The minimization process results in the assignment of a displacement vector (u, v, w) to the subset *center*. Correlation is subsequently repeated throughout the sample to generate a displacement field over a rectangular array of subset centers, defined as nodal points.

There are several critical parameters for correlation. One is the subset size, h_{sub} (in pixels). As Bornert et al. (2009) have convincingly demonstrated, the spatial resolution of displacement measurement is governed predominantly by the subset size; sinusoidal displacement fields of a wavelength less than h_{sub} cannot be measured. The lower bound on subset size is set by the requirement that each subset contain unique information to distinguish it from neighboring subsets. The rule of thumb adopted in the DIC literature to satisfy this requirement is that $h_{sub} > 3 \cdot h_{sp}$, where h_{sp} is the speckle size (Sutton et al., 2009). Furthermore, to avoid aliasing, each speckle must contain several pixels. The corresponding rule of thumb is $h_{sp} > 3\,\text{pixels}$ (Sutton et al., 2009). Conversely, large speckles necessitate large subset sizes, thereby reducing spatial resolution.

The order of the subset shape function also plays an important role. For an n^{th}-order shape function, displacement errors scale with the $n+1^{\text{th}}$ derivative of displacement (Bornert et al., 2009); the shape function employed by Vic-3D is first order (affine) with an additional term to account for camera perspective. The requirement that second-order derivatives be small (to minimize displacement error) sets an *upper* bound on the allowable subset size.

When displacement fields are numerically differentiated (in the simplest case, by finite differences), the resulting strain fields are usually 'noisy' (Nicoletto et al., 2009). The strain fields are therefore filtered by Gaussian-weighted averaging over a prescribed $N \times N$ array of nodal points. The distance between nodal points is defined as the step size, h_{st} (in pixels), and the gage length over which strain averaging is performed is defined as the filter length, h_f (in pixels) (clearly, $h_f = N \cdot h_{st}$). The effects of h_{sub}, h_{st}, and h_f on displacement and strain error both in uniform strain fields and under large strain gradients are addressed below.

2.2.2 Experimental details

Sample preparation

In this part of the study, tests were performed on 1.5 mm thick sheets of aluminum 6061-T6. Three test configurations were employed: uniaxial tension, open-hole tension, and center-notched tension. Samples were machined via electro-discharge machining. The uniaxial tension test sample had dog-bone geometry with a gauge section of 250 mm long and 25 mm wide. Both the open-hole tension and center-notched tension specimens were machined from rectangular strips, 300 mm long and 50 mm wide. The open-hole diameter was 12 mm, and center-notch was 12 mm in length with a 0.6 mm tip radius. Since the length scale for strain decay in the vicinity of such features is controlled by the root radius, the strain gradient in the center-notched sample is expected to persist over a length scale $1/10^{\text{th}}$ of that in the open-hole test.

Two speckling techniques were employed. In both, samples were first coated with flat white spray paint. Speckles were subsequently applied using either a spray canister with flat black spray paint or a Paasche airbrush with black water-soluble paint.

Mechanical testing and DIC setup

All samples were tested at room temperature on a hydraulic testing machine (MTS 810, Minneapolis, MN) at a nominal strain rate of $10^{-4}\,\mathrm{s}^{-1}$. Samples were clamped with hydraulic grips. Strains on the back-face of the uniaxial tension specimen were measured using a laser extensometer (Electronic Instrument Research, Irwin, PA) over a gauge length of 25 mm.

Images for DIC were taken with a pair of digital cameras (Point Grey Research Grasshopper), each with a CCD resolution of 2448×2048 pixels and a 70–180 mm lens (Nikon ED AF Micro Nikkor). The focal length of the lenses was 70 mm, the aperture setting was F-16, and the angle between cameras was 24°. For all experiments described in this work, either the maximum or the minimum focal length was employed to minimize errors arising from differences in magnification between the two cameras. For the three aluminum alloy specimens, images were taken at similar magnifications: 41 pixels/mm for the open-hole and center-notched tension tests and 36 pixels/mm for the uniaxial tension test. The area of the open-hole and center-notched specimens within the field of view was $50\,\mathrm{mm} \times 50\,\mathrm{mm}$, while that for the uniaxial tension specimen was $50\,\mathrm{mm} \times 25\,\mathrm{mm}$. The area of interest for image correlation was selected to exclude un-speckled regions such as the hole or notch.

Speckle pattern characterization

Two approaches are employed for quantifying the speckle size distribution. One is an autocorrelation approach (AC), described by Rubin (2004) and used in previous DIC studies (Bornert et al., 2009; Robert et al., 2007; Sutton et al., 2009). The average speckle size, h_{sp}, is the width of the autocorrelation function, calculated from the points satisfying the equation $A(u) = 0.5$, where A is the autocorrelation function (Sutton et al., 2009). The other approach relies on particle analysis (PA) techniques (Lecompte et al., 2006). These have been implemented in various software packages; the present analysis is performed using ImageJ (Rasband). Prior to analysis, the camera image is thresholded and converted to a binary image. Contiguous features of any size and circularity are found within the new image. The effective diameter of each feature (speckle) is defined as $d_{eq} = 4 \cdot A/P$, where A is its area and P is its perimeter. Using this approach, circular speckles yield an effective diameter equal to the actual diameter; for elliptical speckles, the effective diameter is the geometric mean of the major and minor axes of the ellipse.

Computation of error

In DIC displacement analyses, three types of errors are typically reported: the bias, $\overline{\Delta v}$, the standard deviation, v_{SD}, and the root-mean square error, v_{RMS}

(Bornert et al., 2009; Robert et al., 2007). The bias is a measure of the *systematic* deviation of the measured displacements, v_m, from their true (imposed) values, v_i, given by

$$\overline{\Delta v} = \frac{1}{n}\sum_{j=1}^{n}(v_m - v_i) \tag{2.2}$$

Because the displacement bias is typically negligible compared to the *random* error, characterized by the standard deviation (Bornert et al., 2009), $v_{SD} \approx v_{RMS}$, where

$$v_{RMS} = \sqrt{\frac{1}{n}\sum_{j=1}^{n}(v_m - v_i)^2} \tag{2.3}$$

Only the RMS error is considered in this work. Strain errors are computed in an analogous manner, with displacements, v, replaced by ϵ_{yy} (y denoting the nominal loading direction). Here, again, bias is typically much smaller than the corresponding standard deviation and thus only the RMS strain error is considered.

The imposed displacement field in the uniaxial tensile test is unknown *a priori*. It is taken to be of the form

$$v = \epsilon_i y + C_1 x + C_2 \tag{2.4}$$

where x is the transverse in-plane direction; ϵ_i is the imposed axial strain (taken to be that measured by a 'virtual extensometer' over a gage length of 40 mm on the sample surface); C_1 represents the displacement gradient $\partial v/\partial x$ associated with rigid body rotations (small but not negligible); and C_2 is the rigid body translation (a natural consequence of applying extension to only one end of the test specimen). C_1 and C_2 are determined by fitting Equation 2.4 to the measured (DIC) displacement data. In this scheme, the displacement bias is assumed to be zero, and therefore the RMS displacement error computed using Equation 2.3 is solely a measure of the random error. The sum in Equation 2.3 is evaluated over a sufficiently large array of nodal points to ensure statistically significant results. The RMS strain error is computed in a similar manner.

In the open-hole and center-notched tension tests, only strain error is determined. Axial normal strain values (ϵ_{yy}) from the DIC software are taken along a line emanating from the edge of the hole or the notch at the sample midplane along the x-direction. Strains are interpolated between nodal points using cubic splines. The true spatial variation of axial strain along this line was obtained from finite element analysis, which utilized a material constitutive law calibrated with the uniaxial tensile data. (Although the law was calibrated for both elastic and plastic deformation, the subsequent measurements were restricted to the elastic domain only). The strains obtained from DIC and FEA along with Equation 2.3 are used to calculate the RMS error.

2.2.3 Results and discussion

Speckle size

Speckle size distributions for both the airbrush and spray paint patterns and the relevant statistical values are summarized in Figure 2.1. The figure indicates that the speckles from the airbrush pattern are finer than that from the spray paint pattern. Furthermore, both speckle size distributions are highly skew, implying the presence of speckles several times larger than the median value. The skewness can be problematic for correlation; indeed, correlation is difficult to attain in regions of the pattern where the speckle size is large. These observations suggest that the *median* speckle size is not the premier characteristic of a speckle size distribution, since it is relatively insensitive to the presence of very large speckles. Statistics which account for skewness, such as the autocorrelation speckle size (which is implicitly weighted by the number of pixels within a speckle) or the 90^{th} percentile speckle size (from PA) should be utilized instead. Hereafter, h_{sp} is taken to be that obtained from the autocorrelation method. (Numerically, the values obtained from AC are almost the same as the 90^{th} percentile values.)

Correlation

Full image correlation requires that each subset in the deformed image contain sufficient *unique* information so that it can be located in the undeformed image (Bornert et al., 2009). This requirement sets a *lower* bound on the allowable subset size. Figure 2.2(a) illustrates the effects of subset size (below and above this bound) on the degree of correlation (based on error criteria prescribed by the correlation algorithm). The results are broadly consistent with the rules of thumb for achieving optimal correlation: $h_{sp} > 3\,\text{pixels}$ and $h_{sub} > 3 \cdot h_{sp}$ (Sutton et al., 2009). The latter describes the qualitative trend of Figure 2.2(a) — that larger speckle sizes require larger subset sizes for full correlation. The minimum subset size predicted by the rule of thumb and the subset size required for full correlation also agree quantitatively. For the spray painted speckles, $h_{sp} = 9.3\,\text{pixels}$ and hence the minimum recommended subset size is $h_{sub} = 28\,\text{pixels}$. By comparison, the experimental results show that 99 % correlation is obtained at 17 pixels and full (100 %) correlation at 29 pixels. For the airbrushed speckles, $h_{sp} = 4.5\,\text{pixels}$ and the predicted lower bound on subset size is 13 pixels. 99 % correlation is attained at a subset size of 13 pixels and full correlation at 25 pixels.

Displacement error

Figure 2.2(b) shows the effect of subset size on displacement error for the uniaxial tension test at an applied strain of 0.002 (about half of the yield strain and thus well within the elastic domain). For small subset sizes, below that needed for full correlation, the error scales approximately inversely with subset size. In contrast, for larger subsets, the error asymptotes to a constant value. Similar trends have been reported in previous studies (Haddadi and Belhabib, 2008; Robert et al., 2007). The displacement errors obtained in the present study (0.01–0.02 pixels) also agree with the results of other studies (Robert et al., 2007; Sutton et al., 2007). The subset size that provides the best compromise between spatial resolution and displacement accuracy lies just below that at the asymptote; larger subset sizes yield no further reduction in displacement error. The near-optimal value employed in the subsequent strain error analysis is taken to be 40 pixels for the spray paint pattern. Note that, in general, the optimal subset size depends on a number of factors, including the speckle size distribution and presence of strain gradients within the subset.

For subset shape functions that are first-order, displacement error is expected to be insensitive to the *magnitudes* of rigid body displacements and/or uniform strains within the subset (Bornert et al., 2009). This hypothesis can be assessed for the case of uniform strain; the results are shown in Figure 2.3.

For strains below yielding (i.e. < 0.004) displacement error is indeed constant. Furthermore, the error for low strains is identical to that for nominally *zero* applied strain. This quantity was computed by taking the standard deviation of displacements between two sequential images (before loading). Interestingly, for strains in excess of the yield strain, the error increases dramatically. It is surmised that the latter trend is a consequence of the inherent heterogeneity of crystal plasticity at the length scales being probed by the present measurements ($h_p/10 \approx 3\,\mu\text{m}$).

Strain error

The sources of strain error in digital image correlation are twofold. First, as mentioned previously, numerical differentiation of 'noisy' displacement data results in 'noisy' strain data (Nicoletto et al., 2009). Filtering (averaging) is therefore employed. However, filtering can also introduce strain error if derivatives of strain within the filtering gage length are not negligible. In the uniaxial tension test, the strains are uniform and thus only the former error source is relevant; for the open-hole and center-notched tension tests, both sources must be considered.

The relationship between strain error, displacement error, and subset size for the uniaxial tension test at an applied strain of 0.002 is depicted in Figure

2.3. Here, $h_{st} = 2$ pixels and $h_f = 10$ pixels: both small in comparison to the selected subset sizes. Because displacement values within a subset are correlated to one another, displacement data exhibit sinusoidal variations with a wavelength roughly equal to the subset size. Hence, differentiation of the displacement field to obtain strains yields errors obeying the scaling relationship $\epsilon_{RMS} \propto v_{RMS}/h_{sub}$. From the data in Figure 2.3, the scaling constant is found to equal 1; the agreement between the prediction and the actual strain error is good, demonstrating that, for affine deformations, strain error can be ascribed *solely* to displacement error.

Because displacement values are correlated over a length scale roughly equal to the subset size, strain error can be minimized by choosing a gage length for strain calculation comparable to the subset size. In practice, this is equivalent to choosing a large step size: $h_{st} > h_{sub}/2$ (Ke et al., 2011). An alternate approach is to select an arbitrarily small step size and subsequently filter the resulting strain data. The effect of filtering on the strain error for the uniaxial tension test at an applied strain of 0.002 is illustrated in Figure 2.4. For the smallest step size, two regimes are evident. When $h_f < h_{sub}$, averaging has almost no effect due to the aforementioned correlation of displacements and strains over a subset. In contrast, when $h_f > h_{sub}$, the errors follow the expected scaling relationship: $\epsilon_{RMS} \propto v_{RMS}/h_f$ (Orteu et al., 2007).

Line scans of axial strain for the uniaxial tension test in Figure 2.5(a) demonstrate the efficacy of filtering in reducing strain noise. Note that, when $h_f < h_{sub}$, strain fields oscillate with a wavelength comparable to the subset size. For large step sizes, the magnitude of strain error is diminished (Ke et al., 2011).

Differences between the DIC virtual extensometer strain and the strain measured by the laser extensometer on the specimen back-face are $\leq$ 50 μstrain, indicating that systematic errors (strain bias) are small compared to random errors (strain standard deviation). The random errors are hundreds of μstrain before filtering. Other metrics of strain bias, e.g. the average *shear* strain across the specimen, are similarly small. The assumption made at the outset of the analysis — that strain bias is negligible compared to strain standard deviation — is therefore validated.

Strain gradients constitute an additional source of error, both because a secant line approximation is employed to compute displacement derivatives and because filtering is utilized to reduce noise. A Taylor series analysis proves to be insightful. Suppose that ϵ_{yy} is to be determined at a point y_0. The displacements in the neighborhood of $y = y_0$ can be expressed as

$$v(y) = v(y_0) + v'(y_0)(y - y_0) + \frac{1}{2}v''(y_0)(y - y_0)^2 \tag{2.5}$$

and the corresponding strain, computed using (first-order) forward differences, is

$$\epsilon_{yy}(y) = v'(y_0) + \frac{1}{2}v''(y_0)(y - y_0) \tag{2.6}$$

Since the distance between adjacent nodal points is h_{st}, the difference between the computed strain (from Equation 2.6) and the actual strain, $v'(y_0)$, (i.e. the strain *error*) becomes

$$\Delta\epsilon_{yy}(y_0) = \frac{1}{2}v''(y_0)h_{st} \tag{2.7}$$

That is, strain error is proportional to both the strain *gradient* and the step size. An equivalent statement is that large step sizes lead to a loss in spatial resolution of strain measurements (Ke et al., 2011). Filtering has a similar effect. A Taylor series analysis of a uniformly weighted filter yields

$$\Delta\epsilon_{yy}(y_0) = \frac{1}{4}v''(y_0)h_f \tag{2.8}$$

for filters that are centered on the *edge* of a specimen (e.g. the edge of a hole or notch) and

$$\Delta\epsilon_{yy}(y_0) = \frac{1}{24}v'''(y_0)h_f^2 \tag{2.9}$$

for filters lying away from a specimen edge. The deleterious effects of strain gradients and higher-order derivatives within a filter length are manifest in these relations.

The preceding relationships are confirmed by the results of the open-hole tension test. Figure 2.5(b) illustrates the salient trends. Line scans of strain, ϵ_{yy}, along the sample mid-plane are compared to the FEA prediction at an applied stress of 100 MPa. For small filter lengths and step sizes, numerical differentiation noise is not attenuated and the strains exhibit large-amplitude oscillations (identical to those seen in the uniaxial tension test). Conversely, for large filter lengths and step sizes, strain estimates deviate from those predicted, both with increasing step size (at a constant filter length) and with increasing filter length (at a constant step size). The magnitude of the strain errors (several hundred μstrain) is large compared to the expected strain bias. At the hole edge, for step sizes large enough to reduce strain variability from numerical differentiation, the errors are well described by

$$\epsilon_{RMS} = 0.5\frac{d\epsilon_{yy}}{dx}h_{st} + 0.07\frac{d\epsilon_{yy}}{dx}h_f \tag{2.10}$$

The strain derivative terms were calculated using the FEA results. The first term on the right side of Equation 2.10 is the same as that in Equation 2.7. The coefficient (0.07) of the second term differs from that (0.25) obtained from the Taylor series analysis. The discrepancy is due to the fact that the Taylor series analysis employs uniformly-weighted filtering while the DIC strain calculation uses Gaussian-weighted filtering. The latter provides superior results in the presence of strain gradients.

The previous results can be utilized to generate a 'map' of acceptable parameters (magnification, subset size, filter size) for a DIC experiment on a specimen with a strain concentrator. The assumptions used to construct the map are as follows. First, the step size is chosen to be a small fraction of the subset size: $h_{st} = h_{sub}/10$. Second, speckle size is assumed to be 'optimal': that is, the speckle pattern is reasonably over-sampled so that $4 < h_{sp} < 9$ pixels (Robert et al., 2007; Sutton et al., 2009). With these assumptions, the displacement error (in pixels) should be insensitive to magnification and speckle size and controlled mainly by subset size (Robert et al., 2007). The functional form of the relationship is obtaining by fitting the data in Figure 2.2(b). (Note that the magnitude of the displacement error should be confirmed by performing rigid body experiments before mechanical testing.) Third, the conservative assumption is made that strain errors arising from strain gradients and displacement noise are additive. Then, the minimum magnification needed to resolve a known strain gradient to a prescribed error tolerance can be calculated using Equation 2.10 and relations expressed by Figure 2.4. An example is shown in Figure 2.6, using an error tolerance of 300 μstrain. For an applied stress of 100 MPa, the resulting strain gradient is $10^{-6}/\mu m$, which is indicated by the dashed line (the magnification in the open-hole tension experiment being 41 pixels/µm). Evidently, only a narrow range of subset size and filter length combinations yields acceptable strain data. One such combination is illustrated in Figure 2.5(b).

In the *center*-notched geometry, the strain gradient is about an order of magnitude larger. The map indicates that, to within a reasonable strain error, DIC parameters cannot be chosen to comply with the concurrent requirements of capturing the strain gradient near the notch and mitigating the numerical differentiation noise. Line scans in Figure 2.5(c) confirm this result. The gradient can be captured only by employing a higher magnification. This would also require use of smaller speckles.

These results are a direct consequence of the relationships between the length scales associated with the structural features and the DIC analysis (h_{sub}, h_f). Specifically, in the present case, the gage length for strain computation must be significantly smaller than the notch root radius, which governs the length scale for strain decay. However, to attenuate numerical differentiation noise, the strain computation must be performed over an area large compared to the subset size, which must encompass several speckles and many more pixels. While parameters can be chosen for the open-hole and uniaxial tension tests to satisfy these opposing requirements, no such selection is possible for the center-notched test.

To summarize, errors are minimized by choosing a speckle pattern and DIC parameters in accordance with the following guidelines.

1) Deformations within a subset should be affine; that is, the strain gradients must be small.

2) The subset size, speckle size, and camera magnification should be chosen to obtain full correlation as well as the requisite displacement accuracy. The rules of thumb $h_{sp} > 3$ pixels and $h_{sub} > 3 \cdot h_{sp}$ provide a useful start.

3) The subset size should be sufficiently small that the desired spatial resolution is achieved.

4) Step and filter sizes should be selected to preserve real strain gradients arising from material or structural features while simultaneously minimizing noise due to numerical differentiation.

In some cases, the parameter selection process is over-constrained. This can occur if the error tolerances are low, the area of interest is large, or the length scales for strain variation are small. Error analysis provides useful insights in selecting parameters that yield the best compromise between these competing objectives.

2.3 Case study: SiC/SiC composite

2.3.1 Experimental details

Strain variations associated with the fiber weave in a ceramic composite under uniaxial tension were probed using DIC measurements. Samples were laser-machined from a SiC/SiC composite comprising six layers of 2-D woven fiber (eight-harness satin weave). The specimen were machined so that the tensile direction was aligned with one set of fiber tows. The specimens had dog-bone geometry with a gauge length of 25 mm and gauge width of 8.5 mm. The airbrush technique was used for speckling. Fiberglass tabs were bonded to the sample ends to facilitate uniform load transfer from the grips to the sample. The testing machine and the DIC equipment were identical to those used for the test on the Al specimens. A laser extensometer was used to measure strain on the back-face of the specimen over a gauge length of 25 mm.

In the test orientations employed, surface fibers reside within either long, relatively-flat segments of longitudinal tows or short segments of transverse tows, each passing over a single longitudinal tow (Figure 2.7(a)). Because the matrix conforms to the undulations of the underlying tows, crossovers and flat segments can be discerned from the topographical map generated by DIC (Figure 2.7(b)).

DIC parameters were chosen to satisfy the following requirements: *(i)* a spatial resolution at a sub-tow length scale; *(ii)* full correlation across the entire sample; and *(iii)* a field of view that encompasses the entire specimen width. The last requirement yields an upper bound on magnification. The magnification selected for both experiments, 138 pixels/mm (attained using a lens focal length of 180 mm), was sufficiently high to achieve adequate spatial resolution while remaining below the upper bound. At this magnification, the area within the field of view was 12 mm × 8.5 mm, and $h_{sp} \approx 9.5$ pixels. A compromise between the first two requirements was achieved by selecting the *smallest* subset size that yielded full correlation ($h_{sub} = 51$ pixels). This choice implies a spatial resolution of 0.36 mm, or roughly 30 % of the tow width.

Due to the insensitivity of displacement error to strain, a good estimate of this error for low levels of applied strain (< 0.01) is that obtained at nominally *zero* strain. As stated previously, this quantity is computed by analyzing two sequential images taken before loading. The resulting estimate of displacement error is 0.013 pixels and the (unfiltered) strain error is 255 μstrain (comparable to values obtained from tests on the aluminum alloy). Since the strain noise was unacceptably large in comparison to the strain variations being measured, strains were filtered over a gage length larger than the subset size but significantly smaller than the tow width ($h_f = 75$ pixels $< h_{tow} = 160$ pixels, $h_{st} = 5$ pixels). Based on the trends in Figure 2.4, the resulting strain error induced by numerical differentiation is estimated to be approximately 100 μstrain. (Note that, since $\epsilon_{RMS} \approx \epsilon_{SD}$, $\pm\, 2\epsilon_{RMS}$ gives a 95 % confidence interval). Because strain gradients are unknown *a priori*, other error quantities cannot be estimated. The results presented below show that strain gradients can indeed become unacceptably high for accurate strain determination, especially in the vicinity of matrix cracks.

2.3.2 Results and discussion

Representative results from tension tests are shown in Figures 2.8, 2.9, and 2.10. At small strains (roughly half of the tensile failure strain), the strain fields are reasonably uniform (a result expected on the basis of the satin nature of the fiber weave), with one notable exception. Whereas the axial strains within the long segments of the longitudinal tows are uniform over most of their length, strain concentrations arise in locations where the transverse tows cross over the longitudinal tows. These features are illustrated by the line scans plotted in Figure 2.9. Strain elevations can be rationalized on the basis of *straightening* of axial tows at crossover points (González and Llorca, 2005); in contrast, within nominally flat tow segments, undulations in the thickness direction are small and hence the strain variations are similarly small.

At larger strains (> 0.002), the strain concentrations subsequently 'bleed' into the adjacent longitudinal tows. Approaching the composite failure strain (0.004), strains in excess of 0.02 are seemingly attained in these tows. Upon closer examination of the displacement data, it becomes apparent that these regions are actually cracks, each producing an axial displacement discontinuity. The computed strains are therefore not true material strains. Furthermore, since these strains are essentially equal to the ratio of the local crack opening displacement (COD) to the subset size, the computed values are highly sensitive to the selection of the DIC analysis parameters.

Therefore, displacements (not strains) should be used to assess the evolution of damage within the composite. Displacement maps corresponding to the strain maps are shown in Figure 2.8. In addition to identifying the crack locations, the displacement data are used to compute the COD profiles of the cracks. This is accomplished in two steps (Figure 2.10(a)). First, the crack center is identified by locating the point at which the (apparent) displacement gradient along a line that straddles the crack reaches its maximum. Then, displacement data along this line are fit to a piecewise linear relationship of the form:

$$v = \begin{cases} C_1(y - y_{cen}) + C_2 & y_{min} \leq y \leq y_{cen} - 0.67h_{sub} \\ \\ C_3(y - y_{cen}) + C_4 & y_{cen} + 0.67h_{sub} \leq y \leq y_{max} \end{cases} \tag{2.11}$$

where y and v are the displacement and position, respectively, in the direction of crack opening, and C_i are fitting constants. This equation assumes first-order displacements on either side of the crack. Since displacement data may be unreliable very close to the crack plane, data residing within two-thirds of a subset size from the crack center are excluded from the fitting procedure. This requirement is represented by the inequalities on the right side of Equation 2.11. From these fits, the displacement step and hence the COD becomes $v_{COD} = |C_4 - C_2|$. A threshold of 0.5 µm is used as a minimum value to constitute the presence of a crack. The procedure is repeated along each line passing perpendicular to the subject crack to produce the entire COD profile. Iterating at varying stress levels provides information on crack evolution. Note that crack *locations* can be determined much less accurately than crack *opening displacements*; the accuracy of the former measurement is comparable to the displacement spatial resolution (i.e. subset size), while that of the latter is comparable to the displacement error. If strain fields are instead used to detect cracks, the resolution of the measurement is related to the strain spatial resolution (i.e. filter length). This resolution is significantly lower than the displacement spatial resolution if a large filter length is employed. Efforts to determine crack locations with high fidelity are also complicated by bridging of cracks by the paint used in the speckle pattern.

COD profiles of one such crack (indicated on Figure 2.8) are plotted in Figure 2.10(b). At stresses slightly above that for crack nucleation, the central region of the crack exhibits an approximately elliptical profile, consistent with the prediction for a weak-bridging scenario of a through crack. The profiles near the tips diverge from the elliptical shape, presumably because of influences of neighboring cracks as well as the underlying tow architecture. It may also be a consequence of a more complex crack front in the through-thickness direction. Approaching the ultimate tensile strength, cracks begin to link. This is manifested as non-zero crack opening displacements at the outer boundaries of the data in Figure 2.10(b). Current efforts are focused on extracting pertinent bridging traction laws (Bao and Suo, 1992) from the displacement profiles.

Post-mortem sectioning and micrography confirms the locations of cracks detected by DIC analysis (Figure 2.11). That is, each displacement discontinuity captured by the DIC (Figure 2.11(a)) corresponds to a transverse crack (Figure 2.11(b), (c), and (d)). Each crack comprises breaks through several fibers within the surface 0° tow. The DIC analysis also agrees with micrography on the relative opening displacements of different cracks.

2.4 Concluding remarks

Digital image correlation is capable of measuring full-field displacements and strains with accuracy and spatial resolution unparalleled by strain gages and extensometers. It is especially well-suited for measuring pre-cracking strain distributions and post-cracking damage evolution in fiber composites. However, design of DIC experiments that yield high-fidelity results can be complex, primarily because numerous camera, correlation, and post-processing parameters must be selected simultaneously. These parameters can be categorized into two groups: those that *must* be chosen before an experiment commences (speckle pattern, camera magnification) and those that *can* be selected after the experiment concludes (subset size, step size, filter length).

The present study shows that the optimal results are obtained when even the latter parameters are judiciously chosen *prior* to the test, to ensure that the requisite fidelity is indeed achievable.

By analyzing the results of mechanical tests on an aluminum alloy in various test configurations, analytic relations for displacement and strain error have been developed and validated. Each implies a trade-off. Higher camera magnifications entail not only higher spatial resolution of displacements but also a more limited field of view. The speckle size must be small enough so that each subset has sufficient unique information and large enough so that at least three pixels exist within each speckle. Larger subset sizes reduce displacement error at the expense of spatial resolution. Larger step sizes and filter lengths sacrifice the ability to resolve strain gradients for attenuation of strain noise. Analytic relations that capture these qualitative statements have also been provided.

With appropriate analysis parameters, digital image correlation can capture the evolution of strain within ceramic composites. The present study has illustrated that strain concentrations exist at tow crossovers even in composites with seemingly ‘flat’ woven fabrics. At higher stresses, the strain concentrations lead to the formation of cracks in adjacent longitudinal tows that ultimately cause rupture. In these cases, the DIC results are clearly more meaningful when presented in terms of displacements: strains calculated near a crack being non-physical in nature. A procedure to discern the locations of cracks as well as their opening displacement profiles has been presented.

The procedures of displacement measurement and analysis developed here are employed in subsequent studies on inelastic deformation of CMCs, presented in Chapter 3. The resulting strain fields are used for calibration and assessment of a meso-scale finite element model of a woven SiC/SiCN composite.

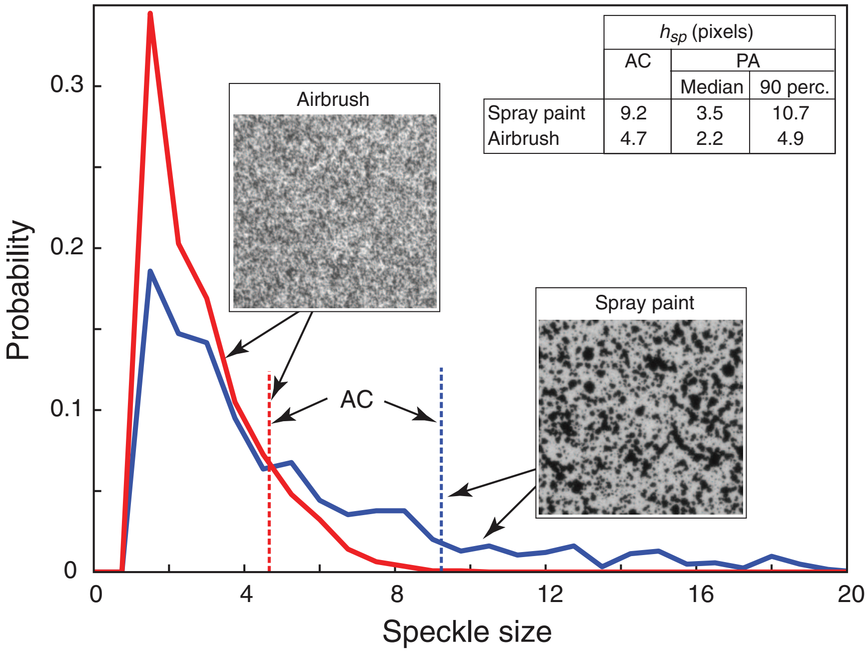

	h_{sp} (pixels)		
	AC	PA	
		Median	90 perc.
Spray paint	9.2	3.5	10.7
Airbrush	4.7	2.2	4.9

Figure 2.1: Speckle size distribution from particle analysis (PA, solid lines) and autocorrelation (AC, dashed lines).

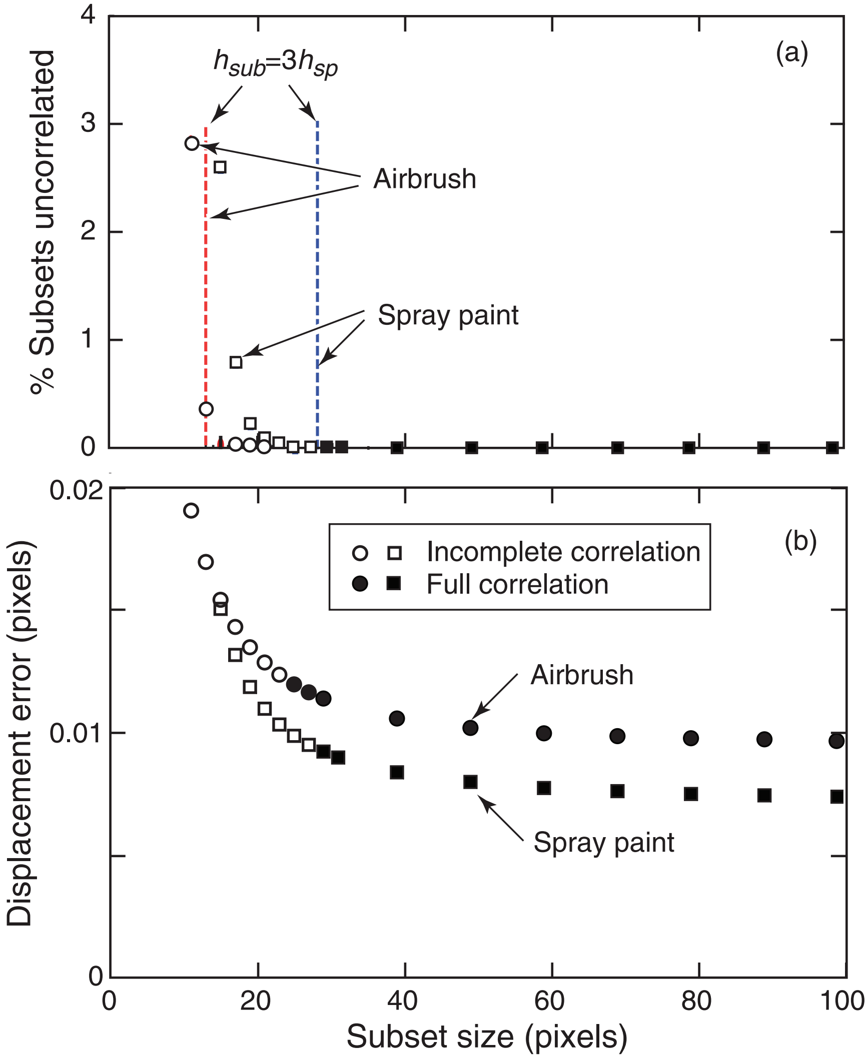

Figure 2.2: Variation in (a) extent of correlation and (b) RMS displacement error with subset size for uniaxial tension tests on Al. The predicted subset for full correlation from the rule $h_{sub} > 3 \cdot h_{sp}$ is shown by dashed lines in (a).

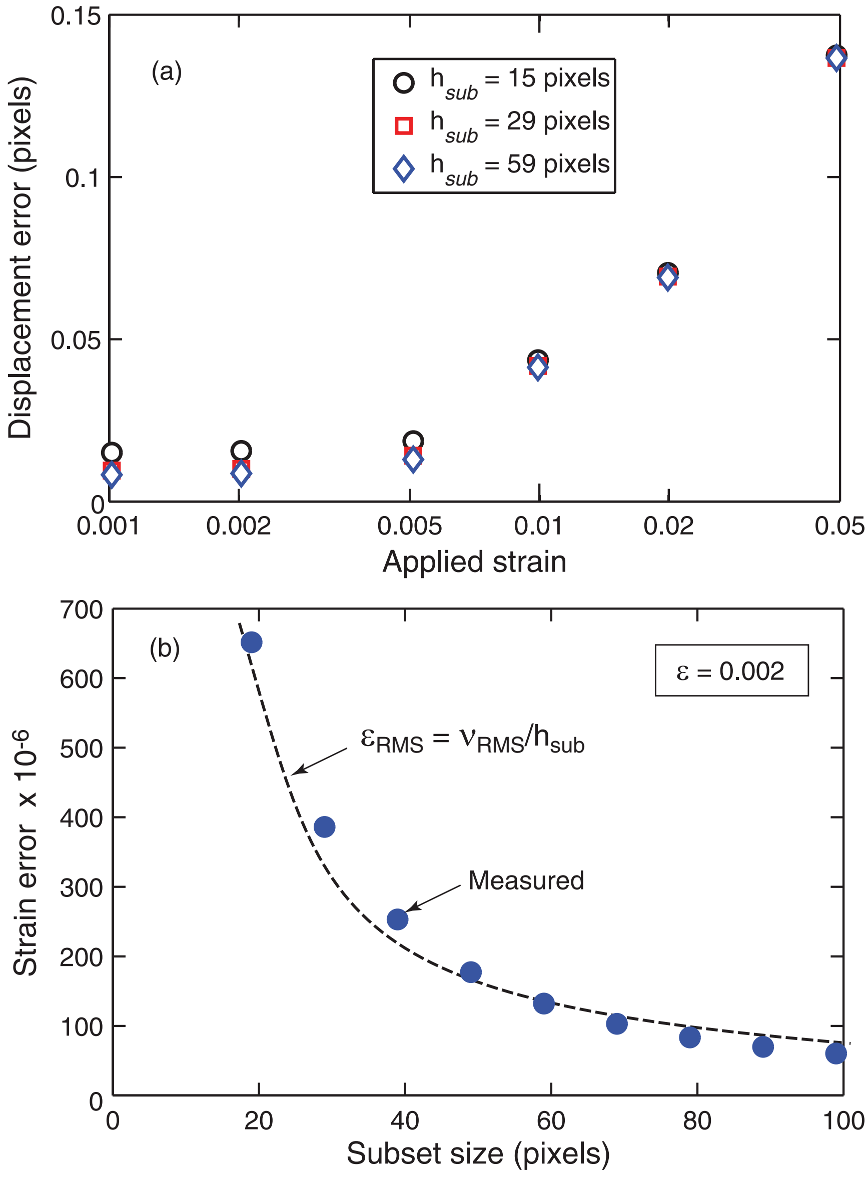

Figure 2.3: Effects of strain and subset size on displacement and strain errors ($h_{st} = 2$ pixels, $h_f = 10$ pixels).

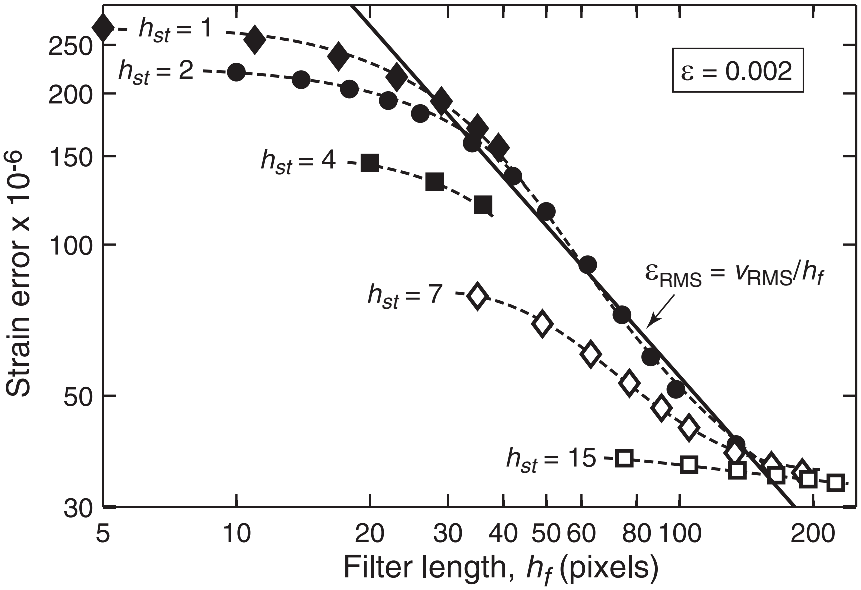

Figure 2.4: Strain error vs. filter length for various step sizes ($h_{sub} = 40$ pixels). Strain error decreases inversely (solid line) with increasing filter length for $h_f > h_{sub}$. Strain error also decreases with increasing step size.

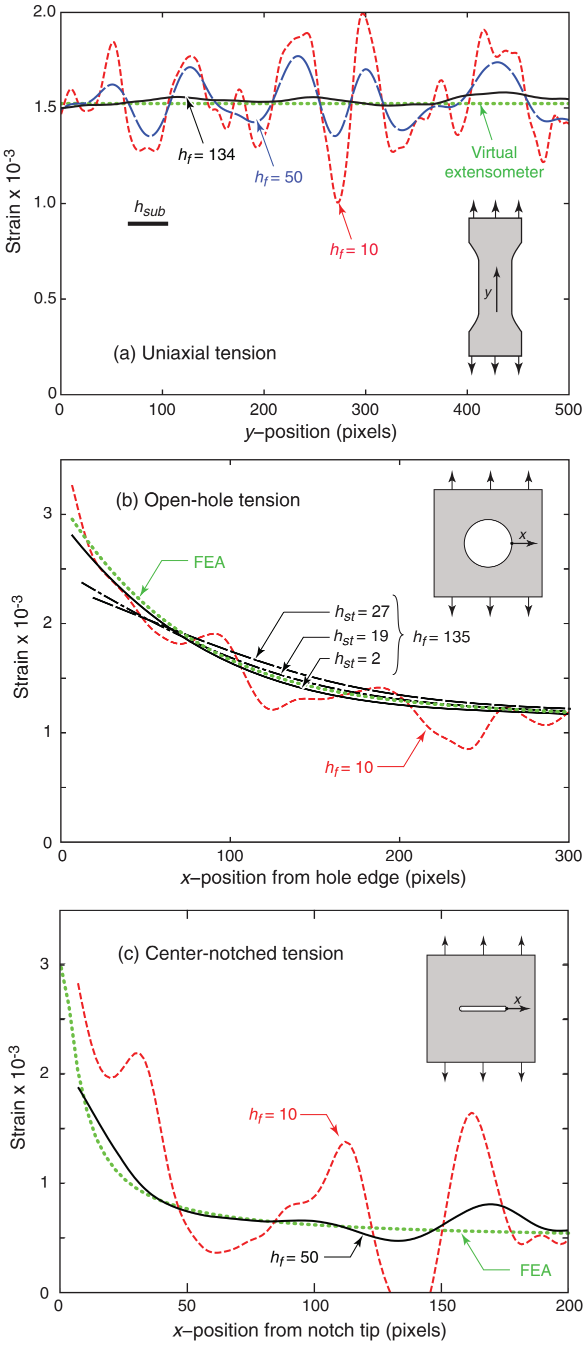

Figure 2.5: (a) Line scans of strain (ϵ_{yy}) for uniaxial tension test ($h_{st} = 2$ pixels, $h_{sub} = 40$ pixels) for various filter lengths. Strain oscillations occur over a wavelength comparable to the subset size. (b) Line scans of strain (ϵ_{yy}) for open hole tension test ($h_{st} = 2$ pixels, $h_{sub} = 40$ pixels) for minimal filtering ($h_f = 10$ pixels) and for constant filter length ($h_f = 135$ pixels). Also shown for comparison is the distribution calculated by FEA. (c) Corresponding line scans for the center-notched specimen ($h_{st} = 2$ pixels, $h_{sub} = 20$ pixels).

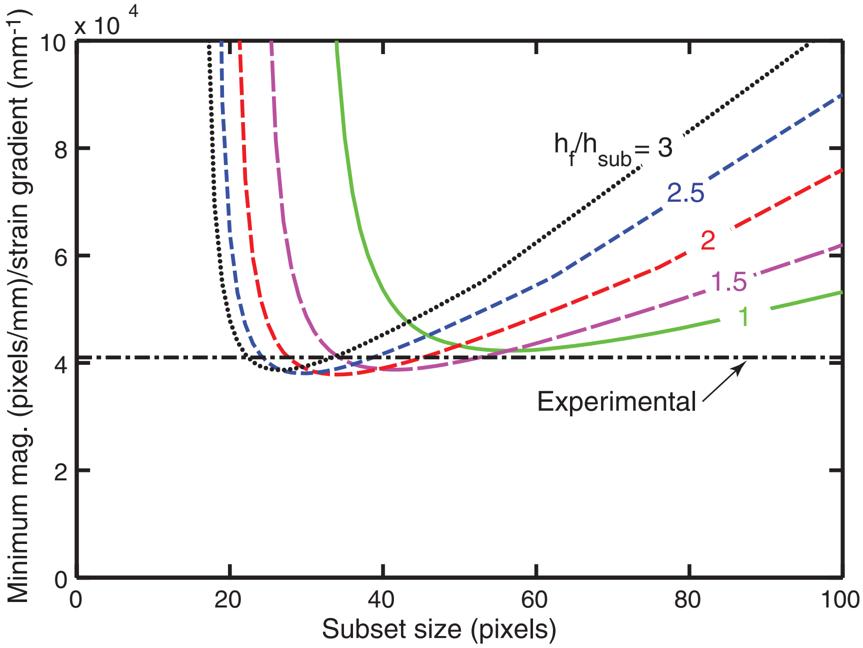

Figure 2.6: Effects of subset size and filter length on the minimum magnification/strain gradient required to achieve a specified strain error (300 μstrain) in a DIC experiment.

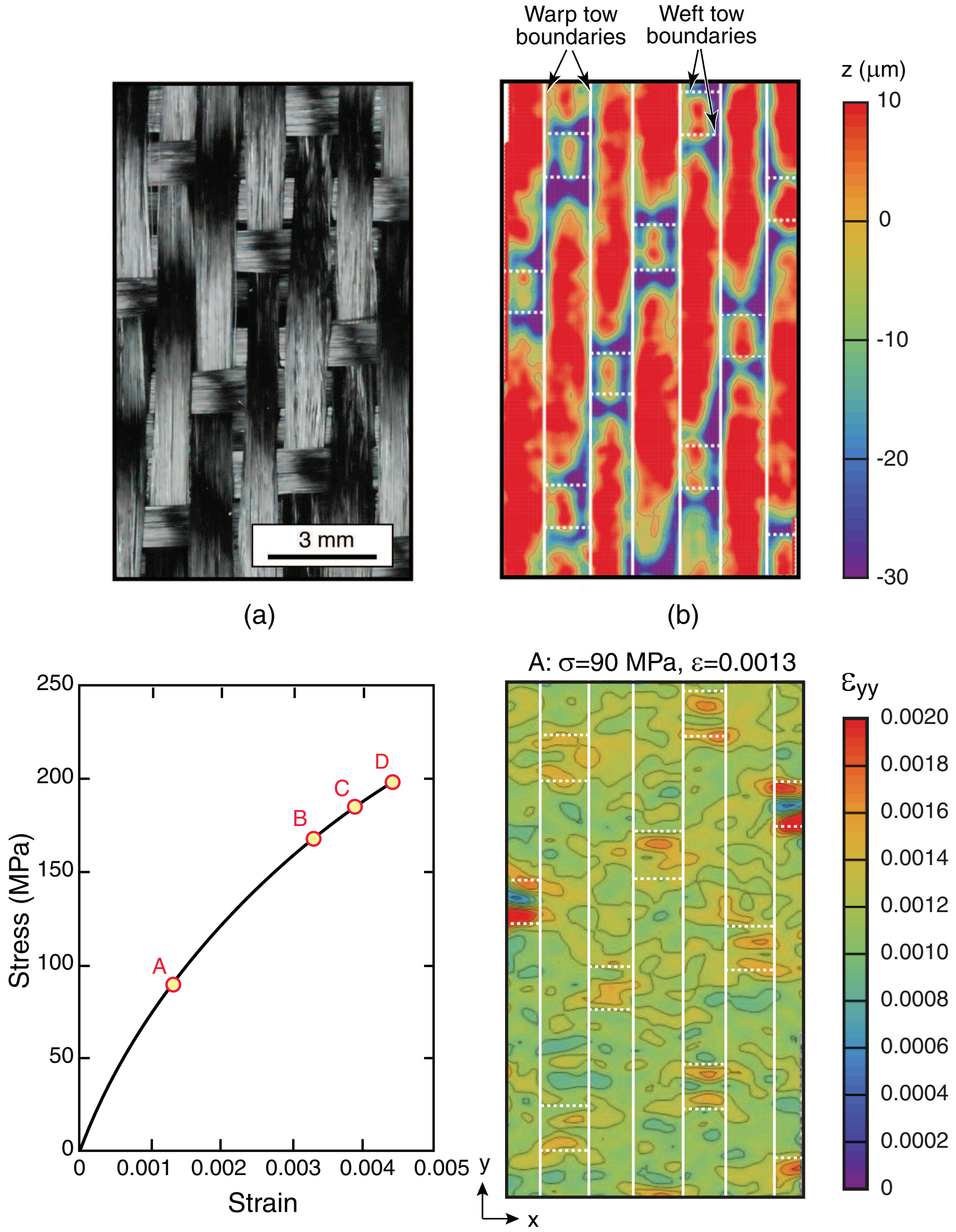

(a) (b)

(c) (d)

Figure 2.7: (a) A representative sample of the woven fabric and (b) topographical map of SiC/SiC composite (at the same magnification). Crossover points and flat segments can be discerned from the changes in height. (c) Tensile stress-strain response and the points (A,B,C,D) corresponding to the strain field in (d) as well as the strain and displacement fields in Figure 2.8.

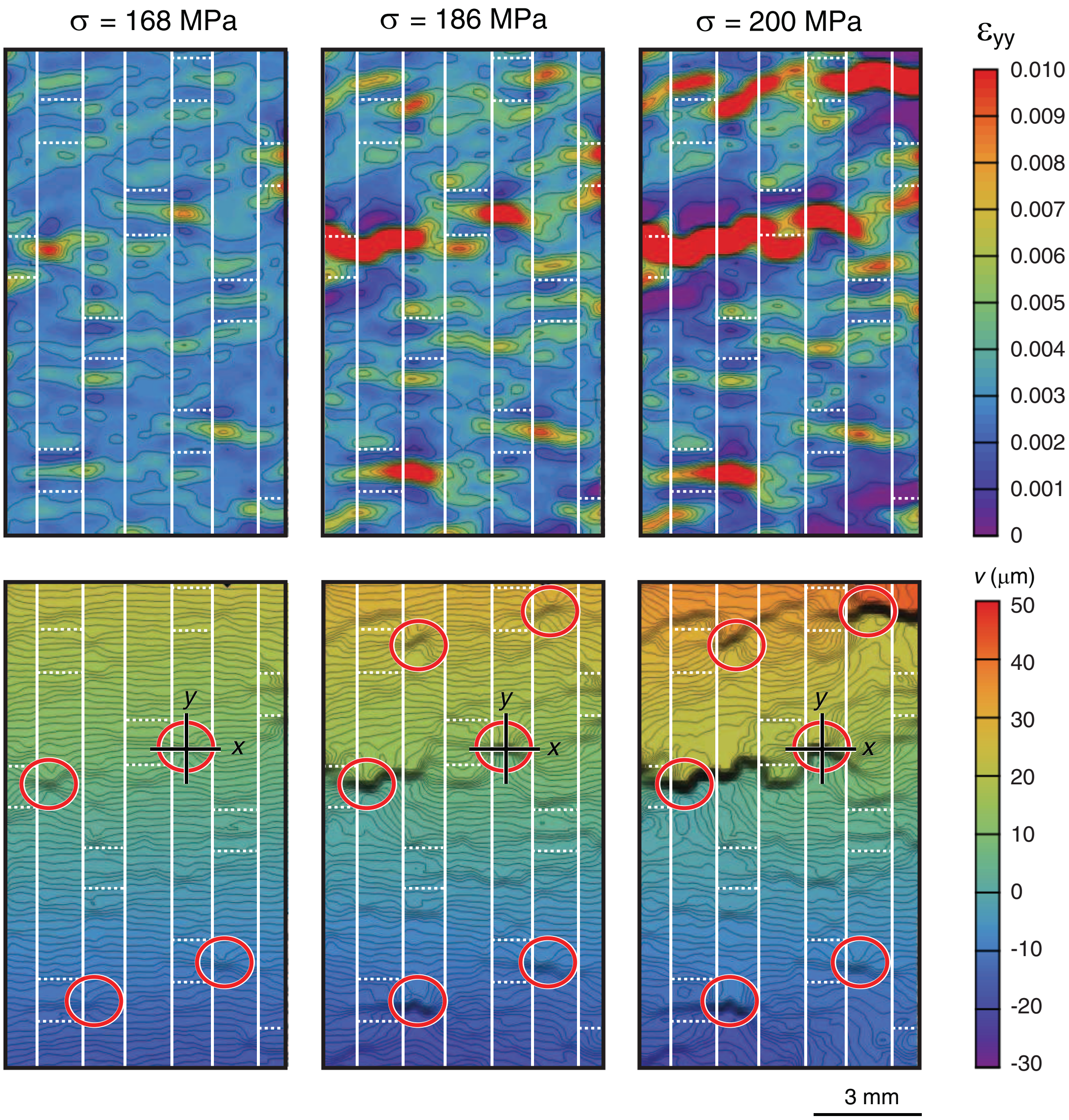

Figure 2.8: Strain (top) and displacement fields (bottom) at three stress levels. The white lines demarcate the tow boundaries, established in Figure 2.7. Circled features are examples of cracks emanating from tow crossovers. The crack with the x-y coordinate system is the one analyzed in Figure 2.10. The black lines in the displacement fields are displacement contours, which are separated by 0.5 μm.

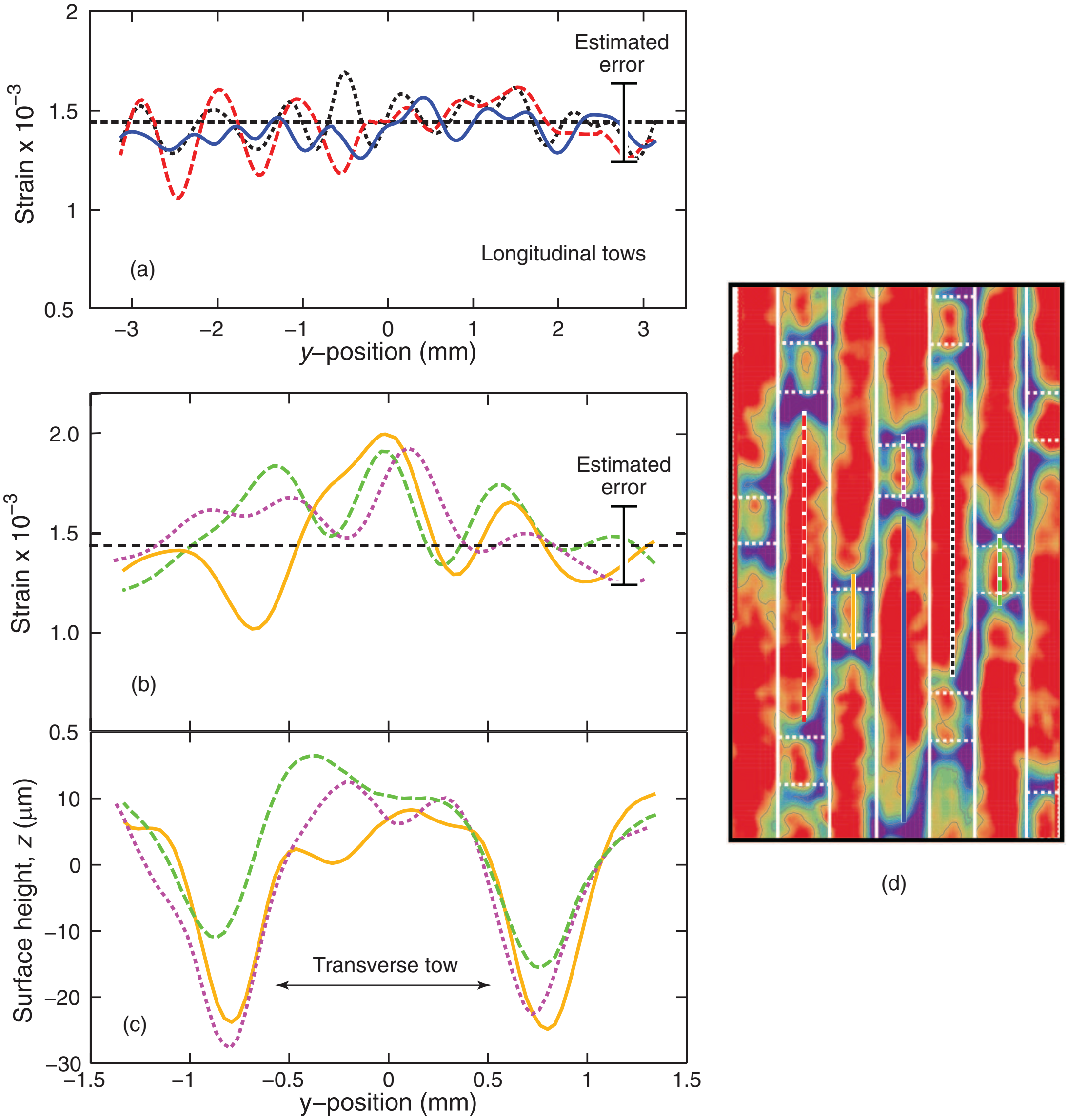

Figure 2.9: (a) Line scans of strain (ϵ_{yy}) along nominally flat segments of longitudinal tows, at an applied strain of 1.4×10^{-3} (about 30 % of the tensile failure strain). The strain is not statistically different from the extensometer strain (dashed line). (b) Line scans of strain and (c) z-profiles along crossover points, at the same applied strain. Strain elevations of about 30 % of the applied strain are found in the center of the transverse tow. (d) Locations of line scans (flat segments and crossover points) within the fiber architecture.

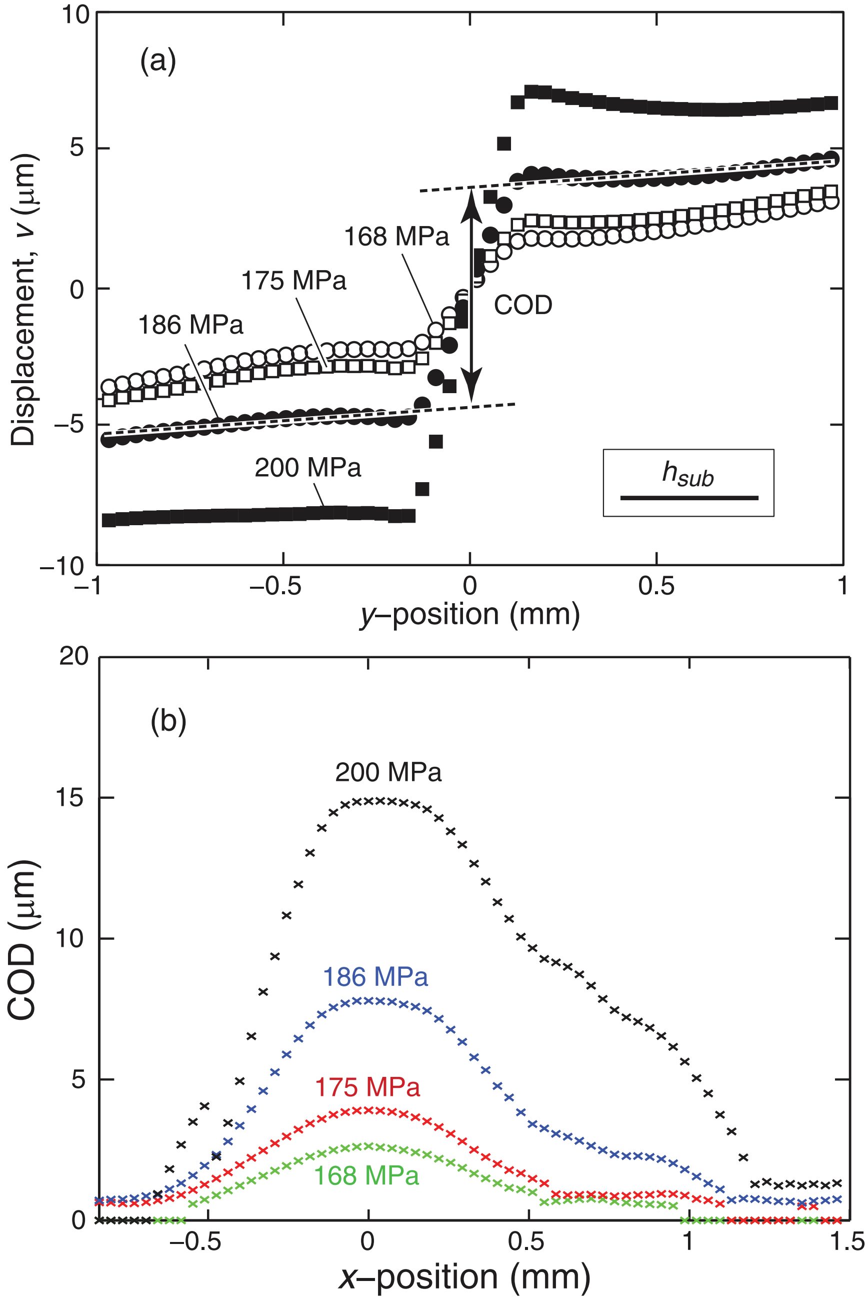

Figure 2.10: (a) Demonstration of procedure used to ascertain crack opening displacement (COD). (b) COD profiles for the crack highlighted in Figure 2.8 at several stress levels.

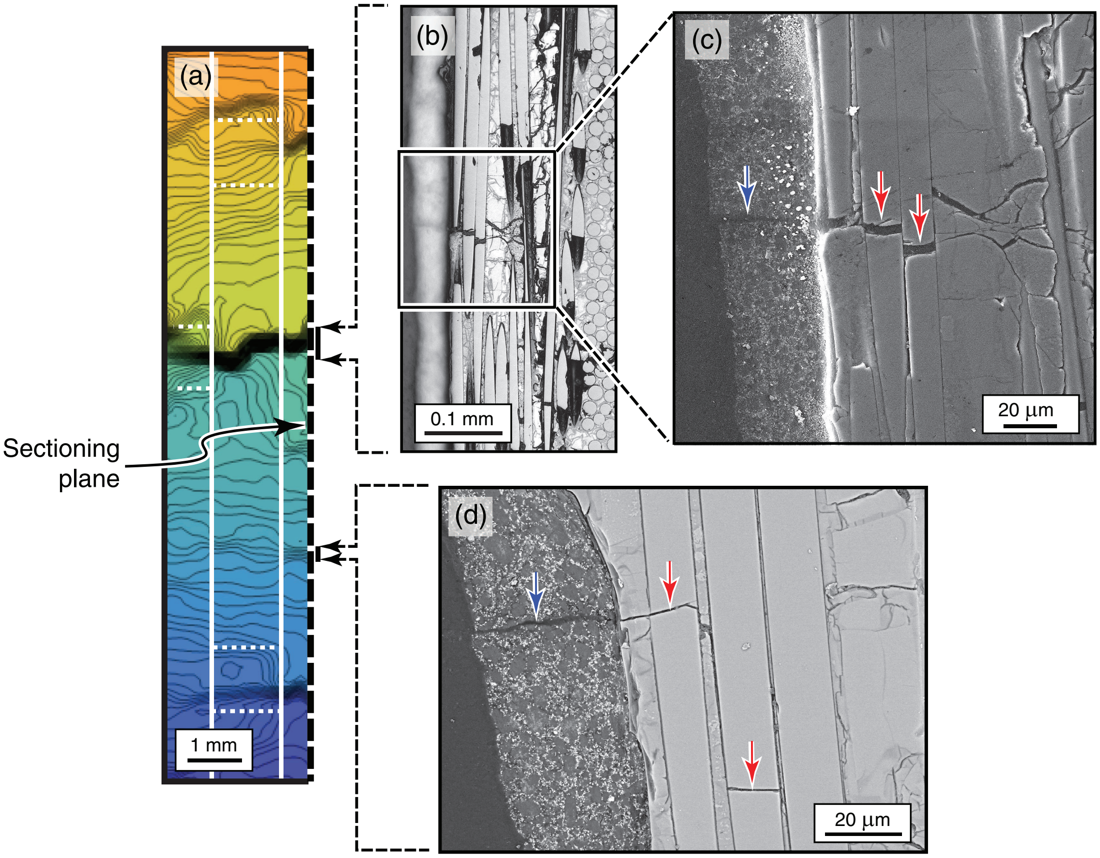

Figure 2.11: Post-mortem micrography of the CMC tensile sample. (a) Section plane with overlaid displacement field showing crack locations, (b) Optical and (c) Electron micrographs of large central crack, and (d) Electron micrograph of small crack. Red arrows denote fiber breaks. Blue arrows denote cracks in the paint.

Chapter 3

Effects of weave architecture on mechanical response of 2D ceramic composites

3.1 Introduction

A primary challenge to furthering the understanding of damage initiation and evolution in woven CMCs is determining the sources of non-uniformity in stresses and strains that arise due to tow waviness. Digital image correlation has enabled the characterization of strain non-uniformity in woven CMCs (see Chapter 2); measurements on a variety of woven CMCs indicate a correlation between surface strains and the underlying weave architecture (Berbon et al., 2002; Qin et al., 2012; Rajan et al., 2014; Shaw et al., 2014a). Progress in understanding the correlation between strain non-uniformity and the weave architecture can only be made with computational models. Existing models of woven composites are either: unable to resolve strains at size scales at or below the tow dimensions (Flores et al., 2010); or have yet to incorporate matrix plasticity (Daggumati et al., 2011; Ivanov et al., 2009; Lomov et al., 2008; Nicoletto et al., 2009).

This chapter focuses on the effects of weave architecture on strain and stress distributions in 2D woven CMCs. The principal objective is to develop a computationally-tractable meso-scale finite element model that: *(i)* provides insights into the origins of strain non-uniformities in 2D woven CMCs found in Chapter 2; and, *(ii)* once suitably calibrated, can be used to probe the effects of weave architecture on fiber stress distributions and, in turn, on the conditions for fracture initiation. Although the scope of the study is restricted to a single weave type, the modeling approach is expected to find utility in examining other weaves. The study exploits recent developments in virtual geometry generation and meshing of woven composites (Cox et al., 2014).

The chapter is organized in the following way. The material of interest and its surface strain distributions during tensile loading are described in Section

3.2. A meso-scale finite element model is presented in Section 3.3. The model is based on a binary representation of the constituent phases: elastic rebar layers for the fibers and elastic/plastic 3D effective medium elements for the matrix. Plasticity within the effective medium is modeled by a pressure-dependent yield criterion. A procedure for preliminary (approximate) calibration of the matrix properties based on classical laminate theory is then described. Comparisons of the strain fields computed by finite elements (FE) and measured experimentally are used to assess the proposed FE formulation and material models. The FE results are used to glean insights into the the origins of the strain distributions, the role of matrix properties in these distributions, and the potential debits in failure stress and strain that might ensue relative to comparable tape laminates.

3.2 Material and experiments

3.2.1 Material

The composite material of interest in this study is S-200H (COI Ceramics, Inc., San Diego, CA). It comprises eight layers of Hi-Nicalon (SiC) fibers with an eight-harness satin weave (8HSW) in a SiCN matrix. The fibers are coated BN followed by Si_3N_4. The matrix was produced by precursor impregnation and pyrolysis. As a result, it contains residual porosity and matrix microcracks after processing (Figure 3.1). The panel was 120 mm × 177 mm and 2.25 mm thick.

3.2.2 Experimental procedures

Uniaxial tension tests were performed on 12 mm-wide dog-bone specimens machined parallel (±0.5°) to one of the fiber directions. The gauge length was 25 mm. Fiber glass tabs were adhered to the end of the specimens with commercial epoxy to promote even load transfer. Specimens were loaded using hydraulic wedge grips and a hydraulic test machine (MTS 810, Minneapolis, MN) at a nominal strain rate of $10^{-5}\,\mathrm{s}^{-1}$. To enable measurement of full field strains and displacements via digital image correlation (DIC), an artificial speckle pattern was applied to the specimen surfaces. The speckle size was approximately 50 µm (measured using an autocorrelation technique). Images for DIC were taken at a magnification of 11 µm/pixel. The spatial resolution of the displacement measurement was maximized by choosing the smallest possible subset size, h_{sub}, that ensured full correlation ($h_{sub} = 31$ pixels or 340 µm). This choice yields a spatial resolution of displacements well below the in-plane tow dimension (roughly 1 mm). The step size was selected to be $h_{step} = 3$ pixels (approximately $h_{sub}/10$). DIC was also used to map the initial surface topography and the results used to identify the locations of the tow boundaries on the surface ply. The global stress-strain response was calculated using the nominal tensile stress and the area-averaged axial strains computed locally at each node via DIC.

3.2.3 Experimental results

The average stress-strain response, computed from two tension tests, is shown in Figure 3.2. The sample-to-sample variations were less than 3 %. The Young's modulus $E_0 = 120\,\text{GPa}$ and corresponding Poisson's ratio $\nu = 0.11$ were calculated from the slopes of the average stress-strain curves in the elastic regime. The axial tensile response of the material is approximately bi-linear with the onset of non-linearity occurring at about 100 MPa. The ultimate tensile strength is $> 500\,\text{MPa}$ and the failure strain is 0.65 %.

Full-field axial strain distributions, $\varepsilon_{app}(x, y)$ at several values of applied strain, ε_{app}, are also depicted in Figure 3.2. Locations of the tow boundaries on the surface ply are overlaid on these strain maps. The roughly square boxes signify locations where tows are oriented transverse to the loading direction and hence are visible on the external surface; these features are referred to as 'tow cross-overs.' Up to $\varepsilon_{app} = 0.3\,\%$, the strains are uniform over most of the surface, with the exception of slight strain concentrations within the tow cross-overs lying closest to the cut edges of the test specimen. These strain concentrations intensify with increasing applied strain while additional strain concentrations appear at cross-overs elsewhere on the specimen surface. At $\varepsilon_{app} = 0.6\,\%$ (shortly before fracture), the majority of transverse cross-overs in the field of view exhibit high strain concentrations, with peak strains exceeding 1 %. In some cases, two bands of strain concentration are present across the width of the cross-over (further illustrated by line scans presented in Section 3.4.2). More importantly, the strains in the axial tows in regions adjacent to the cross-overs become elevated and eventually become the sites of fracture initiation. A progressive series of correlated tow fractures is evident in the last three strain maps in Figure 3.2; each of the tow fractures occurs between adjacent pairs of tow cross-overs. These tow fractures are further evidenced by the fact that the axial strains within those tows are negligible over distances of several mm on either side of the breaks (indicated by the purple bands in the figure).

Distributions in transverse strain, $\varepsilon_{xx}(x, y)$, and out-of-plane displacement, $w(x,y)$, develop in a similar manner (Figure 3.3). That is, strain/displacement concentrations first appear at the cross-overs nearest the cut edge and subsequently intensify and develop elsewhere on the specimen surface as the strain is increased. The elevations in ε_{xx} and w, correlate strongly with those of ε_{yy}, shown in Figure 3.3 and Figure 3.2(C) respectively. The positive out-of-plane displacements at the tow cross-overs indicate straightening of the underlying axial tows, as described below.

The fracture path is shown in Figure 3.4, both in plan view (from DIC images) and from optical images of polished cross-sections in the through-thickness orientation. The fracture path of the surface ply exhibits a macro-scale zig-zag pattern, defined by tow breaks between adjacent tow cross-overs. In contrast, fracture follows a comparatively straight path through the interior plies. We postulate that this is due to differences in the degree of constraint on tow bending and straightening in surface and interior plies. This postulate proves to be consistent with the results of the forthcoming FE model.

3.3 Finite element model

3.3.1 Mesh and geometry

A finite element model of an idealized unit cell of the weave was created using the *Virtual Specimen Generator*, detailed by Blacklock et al. (2012) and Rinaldi et al. (2012). Here the tows are taken to be elliptical in cross-section. In general, each tow cross-section along the tow axis is characterized by four parameters: the center of mass, the cross-sectional area, the tow aspect ratio (major to minor axes dimensions), and the rotation of the major axis relative to the macroscopic fabric plane. In the present implementation, the tows are assumed to have the same cross-sectional areas and aspect ratios along their length and that the rotation of the major axis is zero everywhere. Furthermore, each tow is assumed to be identical to every other: the tows being related to one another through translation and rotation operations. The tow dimensions are selected to match those measured experimentally. Using these inputs, the *Virtual Specimen Generator* yields a three-dimensional representation of the surface of each tow within the unit cell. Tow interpenetration, when it occurs, is rectified using a set of topological rules defining the position of tows with respect to each other to guide minor adjustments to the tow geometry (Rinaldi et al., 2012). The resulting tow loci and tow profiles are shown in Figure 3.5.

Conventional meshing techniques (using, for instance, tetrahedral elements) tend to produce meshes with highly distorted elements in regions where the matrix is very thin, i.e. between adjacent tows (Nemeth et al., 2010). An alternative approach is to utilize a voxel mesh (as done, for example, by Kim and Swan (2003)), so that the composite is meshed with brick elements. The latter approach is employed here. Each voxel is assigned either to a tow or to the surrounding matrix, depending on whether the centroid of the voxel lies inside or outside of the tow surface. The voxelization algorithm of Patil and Ravi (2005) was used to generate the voxel mesh. Matrix present on the composite surface and between fabric plies was incorporated by adding a layer of matrix elements above and below the tows.

The disparate properties of the constituent phases—stiff, non-breaking fibers and a compliant, weak matrix—were treated using a binary model formulation (Cox et al., 1994; Flores et al., 2010; Xu et al., 1995; Yang et al., 2005). The model employs a dual mesh comprising: *(i)* solid (3D) effective medium elements that define the specimen geometry and embody the matrix-dominated constitutive properties; and *(ii)* surface elements containing rebar layers, embedded in each effective medium element that resides inside a tow and embody only the axial fiber stiffness. With respect to the coordinate axes defined in Figure 3.5, the rebar layers are placed on the $y - z$ and $x - z$ mid-plane of the host continuum element for axial and transverse tows, respectively. The load-bearing direction of the rebar layers is aligned parallel to the (local) tow axis. For voxels lying outside of the tows, effective medium elements without rebar are used. The effective medium properties include the shear stiffness of local assemblies of fibers and matrix, the stiffness of such assemblies transverse to the fibers, and the stiffness of the matrix in the fiber direction. Thus the effective medium properties are related (but not identical) to those of the matrix alone. A similar dual-mesh scheme had been employed previously in a simpler form (Flores et al., 2010). In that case, the axial fiber properties of each tow were embodied in a *single line element* located at the tow center line. The rebar layers used in the present model yield higher fidelity in the computed tow stresses. Additionally, they allow the stress gradients transverse to the tow axis to be captured.

For computational purposes, the rebar layers are assigned a thickness, t_r, selected such that the volume of rebar in the model is consistent with the fiber volume fraction in the entire composite ($V_f = 0.52$, calculated from the areal density of the woven fabric and the mass density of the fibers reported by the manufacturer). That is, $t_r = t_e V_f / V_{tow}$ where t_e is the thickness of the effective medium element perpendicular to the plane of the rebar and V_{tow} is the volume fraction of tows (66 %).

To explore the effects of constraints on tow straightening, we model several test geometries, ranging from completely unconstrained (i.e. a single ply) to completely constrained (i.e. an infinite number of plies). Here, the term ”ply” refers to a single layer of fabric that comprises both axial and transverse tows. We note that a single ply is asymmetric with respect to its thickness direction; such a ply is therefore expected from basic composite theory to exhibit some tension/bending coupling.

Four geometries, depicted in Figure 3.5(b)–(e), were investigated:

1) A single ply, representative of either an exceedingly thin composite or of an unconstrained surface ply produced, for example, by partial delamination of a surface ply from the bulk;

2) A two-ply symmetric lay-up, without the tension/bending coupling present in the single ply model;

3) A four-ply symmetric lay-up, used to explore effects of internal plies on the response of surface plies; and

4) An infinitely-thick composite, represented by a symmetric two-ply lay-up with periodic boundary conditions in the thickness direction.

For the two- and four-ply symmetric lay-ups, the plies were arranged so that the locations of tow crossovers within one ply did not coincide with those in any other ply (see Figure 3.5).

The finite element simulations were conducted in ABAQUS Standard (Version 6.12-EF4, Dassault Systèmes). Reduced integration brick elements (C3D8R) were used for the effective medium whereas reduced integration embedded surface elements (SFM3D4R) were used for the rebar layers. Successful mesh convergence was achieved using voxels of size 92.8 µm × 92.8 µm × 30 µm, yielding approximately 100,000 effective medium elements and 66,000 embedded surface elements within each ply.

3.3.2 Boundary conditions

Periodic boundary conditions were used to replicate the unit cell in the in-plane directions (x and y) and to model the geometry with an infinite number of plies (using periodicity in z). The periodic boundary conditions are implemented using three 'fictitious' nodes, denoted F_x, F_y, and F_z (Xia et al., 2003). Periodicity in the x-direction, for example, is enforced by imposing constraints on the displacements u_i via:

$$\begin{aligned} u_x(R) - u_x(L) &= -u_x(F_x) \\ u_y(R) - u_y(L) &= -u_y(F_x) \\ u_z(R) - u_z(L) &= -u_z(F_x) \end{aligned} \tag{3.1}$$

where R and L denote right and left faces, respectively (Figure 3.5(b)). That is, the difference in displacements between corresponding (periodic) nodes on the right and left faces equals the displacement of the corresponding fictitious node. The latter displacement is related to the overall strain, $\hat{\epsilon}_{ij}$, of the unit cell by $\hat{\epsilon}_{ij} = u_i(F_j)/L_j$ where L_j is the length of the unit cell in the j-direction. Axial strains are applied by imposing displacements on the fictitious node F_y in the y-direction. The remaining degrees of freedom of the fictitious nodes are allowed to relax to ensure that all average stresses except σ_{yy} in the unit cell are zero. Finally, the rotational degrees of freedom were constrained using the relationship $\hat{\epsilon}_{ij} = \hat{\epsilon}_{ji}$, which implies:

$$\begin{aligned} L_y u_y(F_x) &= L_x u_x(F_y) \\ L_z u_z(F_y) &= L_y u_y(F_z) \\ L_x u_x(F_z) &= L_z u_z(F_x) \end{aligned} \tag{3.2}$$

3.3.3 Constitutive properties

As in Flores et al. (2010), the response of the effective medium elements is taken to be elastic-plastic, in accordance with a linear Drucker-Prager (DP) yield criterion and an associated flow law. (In the present context, "yield" and "flow" refer to the onset and evolution of inelastic straining arising from distributed micro-cracking.) The DP model is a pressure-dependent law commonly used to describe cracking and comminution of brittle materials. The yield condition can be expressed in terms of the principal stresses $(\sigma_1, \sigma_2, \sigma_3)$ as:

$$\sqrt{\frac{(\sigma_1 - \sigma_2)^2 + (\sigma_2 - \sigma_3)^2 + (\sigma_1 - \sigma_3)^2}{6}} = A + B(\sigma_1 + \sigma_2 + \sigma_3) \tag{3.3}$$

The constants A and B are calibrated following the procedure outline in Flores et al. (2010). First, yield in uniaxial tension $(\sigma_2 = \sigma_3 = 0)$ is assumed to occur when $\sigma_1 = \sigma_{em}^{nl}$ where σ_{em}^{nl} is the effective medium stress at the onset of non-linearity. Second, the yield stress in hydrostatic tension is assumed to be the same as that in uniaxial tension: that is, $\sigma_1 = \sigma_2 = \sigma_3 = \sigma_{em}^{nl}$. Substituting these results into Equation 3.3 yields $A = \sqrt{3}\sigma_{em}^{nl}/2$ and $B = -1/2\sqrt{3}$. Finally, associated flow implies that the friction angle β equals the dilatation angle ϕ and is related to B by $\tan\beta = -3\sqrt{3}B$.

3.3.4 Preliminary calibration of constituent properties

Since the rebar elements represent the axial fiber properties, they are assigned a stiffness that, in combination with their thickness, yields the stiffness that would be obtained from the axial fiber bundle (with Young's modulus $E_f = 270\,\text{GPa}$). Fiber fracture is neglected.

Direct computation or prediction of the effective medium properties, on the other hand, is problematic, for two reasons. First, because of the inhomogeneous and porous nature of the matrix, even the average elastic properties are difficult to estimate *a priori*. Second, the effective medium elements, by definition, embody not just the matrix properties but also the contributions of the fibers to the off-axis properties. In light of these challenges, we adopt a pragmatic approach for calibrating the effective medium properties, using the measured stress-strain response of the composite, in the following way.

The calibration procedure is based on (2D) laminate theory. As such, it treats the fibers as being straight and aligned with the principal material directions. Although this assumption is seemingly at odds with the objective of probing the strain variations associated with tow waviness, we find that the procedure yields surprisingly good results, largely because the tows are indeed straight over most of their length. In principle, an iterative procedure could be employed to achieve higher fidelity. This would be done by using the preliminary estimates of the effective medium properties to perform a set of finite element simulations, comparing the computed results with the pertinent experimental measurements, judiciously adjusting the effective medium properties to bring the results into closer agreement with the measurements, and repeating the finite element simulations with the adjusted parameter values. A small number of such iterations would almost certainly be adequate to reproduce the measurements with high accuracy.

For the purpose of the approximate calibration, the composite is modeled as a symmetric cross-ply laminate (i.e. $[0°/90°]_s$). The elastic constants of a single unidirectional ply comprising effective medium elements with Young's modulus E_{em} and Poisson's ratio ν_{em} and with embedded rebar elements are given by (Flores et al., 2010; Nazarian and Zok, 2014):

$$\begin{aligned} E_1 &= V_f E_f + E_{em} \\ E_2 &= E_{em} \\ \nu_{12} &= \nu_{em} \\ G_{12} &= \frac{E_{em}}{2(1+\nu_{em})} \end{aligned} \tag{3.4}$$

where V_f is the volume fraction of fibers and the subscripts 1 and 2 denote the fiber and transverse directions, respectively. (Note that the terms containing the effective medium modulus in Equation 3.4 are *not* weighted by the matrix volume fraction, since the effective medium fills all space.) The reduced compliance matrix of the axial ply (assumed to be in plane stress) is given by:

$$\boldsymbol{S}_0 = \begin{bmatrix} 1/E_1 & -\nu_{12}/E_1 & 0 \\ -\nu_{12}/E_1 & 1/E_2 & 0 \\ 0 & 0 & 1/2G_{12} \end{bmatrix} \tag{3.5}$$

Similarly, the compliance matrix of the 90° ply is:

$$\boldsymbol{S}_{90} = \begin{bmatrix} 1/E_2 & -\nu_{12}/E_1 & 0 \\ -\nu_{12}/E_1 & 1/E_1 & 0 \\ 0 & 0 & 1/2G_{12} \end{bmatrix} \tag{3.6}$$

Then, from elasticity, the compliance matrix for the cross-ply laminate is:

$$\boldsymbol{S}^c = 2([\boldsymbol{S}_0]^{-1} + [\boldsymbol{S}_{90}]^{-1})^{-1} \tag{3.7}$$

The elastic properties E_{em} and ν_{em} of the effective medium are obtained through an iterative numerical procedure in which the errors between the computed laminate properties (using the preceding framework) and the experimentally-measured values are minimized. Taking the fiber properties to be $E_f = 270\,\text{GPa}$ and $V_f = 0.52$, the resulting effective medium elastic constants become $E_{em} = 50.0\,\text{GPa}$ and $\nu_{em} = 0.266$.

An analogous (pseudo-elastic) procedure is used to infer the *inelastic* properties of the effective medium. This is accomplished by first computing the composite secant modulus at each level of strain from the experimental data. The preceding numerical fitting procedure is then repeated, using the *secant modulus* in place of the *elastic modulus* at each level of strain. This yields a function of the effective medium secant modulus vs. applied tensile strain. The function is then converted straightforwardly into a stress-strain curve for the effective medium. The results of this operation are plotted in Figure 3.6. The stress-strain curve exhibits an elastic portion with a modulus of 50 GPa, an inelastic (nearly-linear) portion for stresses in the range of 45–85 MPa, followed by nearly perfectly-plastic behavior through to fracture. Also shown in Figure 3.6 are three linear or bi-linear idealizations used in the subsequent finite element simulations. They include: *(i)* elastic behavior with a modulus of 50 GPa (line labeled A), *(ii)* a bi-linear response with a post-cracking tangent modulus of 19 GPa, obtained by fitting the curve inferred from the calibration procedure over the pertinent stress range (line B), and *(iii)* elastic behavior with a reduced modulus of 19 GPa (line C), selected to match the post-cracking tangent modulus in the preceding case (line B).

3.4 Finite element simulations

3.4.1 Macroscopic response

Preliminary finite element simulations with the ”experimental” effective medium response proved to be satisfactory in matching the tensile stress-strain curve at small strains but underestimated the measurements at higher strains, by about 10 % to 20 %. One example, for the two-ply model, is shown in Figure 3.7(a). The discrepancies are attributable mainly to bending and straightening of the wavy portions of the tows: a form of geometric softening that naturally occurs in the real composite but is neglected in the laminate analysis used for calibration. (Further evidence and manifestations of tow bending and straightening are described below.) This results in underestimation of the effective medium flow stress at high strains and, in turn, underestimation of the composite response from the finite element simulations. In light of these results, further finite element simulations employed the (stiffer) bi-linear representation shown in Figure 3.6. Select simulations for purely linear-elastic behavior, with one of the two moduli shown in Figure 3.6, were also performed, largely to investigate the effects of matrix *elasticity* on bending and straightening of the wavy sections of the tows.

The effects of ply lay-up on the global stress-strain curves (using the bi-linear representation of the effective medium response) are shown in Figure 3.7(a). The results consist of four computed stress-strain curves and the experimentally-measured curve. Initially, for stresses less than 100 MPa, the computed curves are nearly coincident with one another and with the measured curve. In all cases, the computed stress at the onset of non-linearity is about 100 MPa. Thereafter, at higher stresses, the curves exhibit small but systematic differences. Notably, the single-ply model exhibits the softest response: a result of the low constraint on tow straightening. The two-ply model is somewhat stronger. The four-ply and two-ply infinite models yield yet higher stresses, although the latter two are nearly indistinguishable.

The variation in the rebar stress with applied strain is plotted in Figure 3.7(b). Even in the early stages of loading, the rebar stresses deviate from those expected from *straight* fibers, notably $\varepsilon_{app}E_f$. This is a consequence of the misalignment of the tows with the loading axis at the tow crossovers. The number of plies also plays a role: the differences are greatest for the single-ply model and least for the two-ply infinite model. Figure 3.7(b) also reveals evidence of tow *bending* and associated effects of ply constraint. Bending causes variations in the rebar stresses from their mean values at each level of applied strain, as indicated by the error bars. Once again the effects are greatest in the single-ply model, since, in it, the constraint against tow bending is the weakest.

Despite the slight differences in the computed stress-strain curves, the results, on the whole, agree adequately with the measured curve. As a result, no further efforts were made to refine the plastic properties of the effective medium. Furthermore, the slight discrepancies between measured and computed tangent moduli at the highest stresses may reflect the onset of fiber fracture: a feature not incorporated in the present model.

3.4.2 Effective medium strains and displacements

To facilitate a valid comparison between the strain distributions measured by DIC and calculated by FE, all strains were calculated from the nodal displacements in the same manner. First, the nodal displacements from DIC and from FE were interpolated in x, y and subsequently evaluated on a *common* (x, y) grid with 40 µm nodal spacing. Strains were then computed by differentiating the gridded displacement data with respect to the spatial coordinates. Finally, the resulting strains were averaged using a Gaussian filter of length, $h_f = 280\,\mu\text{m}$, and standard deviation $0.25h_f$. With these selections, the gauge length for strain computation is less than one-third of the tow width ($\sim 1\,\text{mm}$). The axial strain distributions obtained in this manner are presented as full-field maps in Figure 3.8; select line scans (along lines denoted C and D) are plotted in Figure 3.9.

The computed axial strains, ε_{yy}, exhibit patterns that are broadly in accord with those observed in the DIC measurements (the latter also shown for comparison in Figures 3.8 and 3.9). Notably, the peak strains are obtained at the tow crossovers. This is attributable to bending of the wavy sections of the axial tows. The greatest curvature in the tow is at the edges of the tow cross-overs, coincident with the locations of the peak strains.

The magnitudes and spatial distribution of these strains vary considerably with the number of plies. In the single-ply model the values are highest and the elevated strains persist over the entire crossover region, with two rather small peaks near the edges. For the models with multiple plies, two distinct strain peaks, of reduced magnitudes, exist along the edges of each crossover; between the peaks the local strain is roughly equal to the applied strain. In the two-ply infinite model the strains at the tow cross-over are the smallest and are comparable to elevations present in regions away from the cross-overs. This trend further exemplifies local tow bending and straightening as well as the effects of ply number on the degree of constraint. The number of strain maxima observed in the experiments is heterogeneous: some tows (line C) exhibit one maximum whereas others (line D) exhibit two. These variations likely reflect heterogeneity in the local geometry of the tows and the matrix microstructure. Away from the tow crossovers, the experimental strains exhibit fine-scale fluctuations around ε_{app}. The magnitude of these fluctuations appears to be of the same order as the strain error associated with DIC (Rajan et al., 2012) and are therefore likely spurious.

Maps of the computed transverse strain, $\varepsilon_{xx}(x,y)$, and out-of-plane displacement, *w(x,y)*, along with select line scans (along lines E and F), are shown in Figure 3.10. The transverse strains and out-of-plane displacements are similarly periodic, with elevations correlated with the location of the tow crossovers. The magnitude of the out-of-plane displacements is dependent on the number of plies: 12 µm in the single ply model, 3–4 µm in the two ply model, and negligible displacement in the four ply model. The transverse strains follow a similar trend(Figure 3.10(b)); values vary from 0.3 % in the single-ply model to 0 % in the four-ply model.

The effects of elasticity, plasticity, and ply number on the strain concentrations, characterized by $k_\varepsilon = \varepsilon_{max}/\varepsilon_{app}$ (with ε_{max} being the maximum axial strain), are summarized in Figure 3.11. For each of the four models, k_ε is initially constant (independent of ε_{app}, in the elastic domain), at values ranging from 1.1 for the two-ply infinite model to 1.9 for the single-ply model. Once yielding occurs, k_ε rises rapidly to a plateau level. Here again k_ε increases with decreasing ply number, varying from 1.2 to 2.6. Interestingly, the post-yield values are similar to those obtained for an elastic effective medium with a reduced modulus (19 GPa, matching the post-yield tangent modulus of the bi-linear case). The implication is that the extent of strain concentration is dominated by the instantaneous tangent modulus of the effective medium. The role of the effective medium properties on the axial strain distributions is further illustrated in Figure 3.12 for two representative models (those with one and four plies), along the line labeled C in Figure 3.8. The strains at the cross-overs decrease with increasing stiffness of the effective medium. Clearly, strain concentrations are not caused by inelasticity *per se*; instead, they are a manifestation of the *mismatch* in mechanical properties of the constituent phases coupled with the weave geometry.

Although rigorous quantitative comparisons between computed and measured strains were not performed, it appears that, from examination of Figures 3.8, 3.9, and 3.10, the experimental results fall between those computed for the one- and two-ply models. The variations obtained experimentally from one cross-over to the next are likely due to variations in microstructure and properties of the matrix material beneath the tows. That is, regions that contain larger-than-average pores and microcracks will experience lower constraint and higher strain concentrations.

3.4.3 Rebar stresses

Contour plots of the normalized rebar (or fiber) stress, $\sigma_f/(\varepsilon_{app}E_f)$, are presented in Figure 3.13. The stresses are those in the top set of axial tows (closest to the surface), averaged through the tow *thickness*. Regions contained within the black contour lines experience a stress $\sigma_f/(\varepsilon_{app}E_f) > 1$. Also shown on the figure are elemental stresses in the transverse cross-sections denoted by the dashed lines. Line scans of the fiber stress, averaged over the cross-sectional *area* of the tow, are plotted against axial position in Figure 3.14, for the tow identified in Figure 3.13. The dots are average values and the error bars represent the full range, from minimum to maximum.

The computed fiber stresses provide complementary information to the surface (effective medium) strains. In the cross-over regions, where the transverse tows experience high strain and the underlying axial tow undergoes straightening, the fiber stresses are generally at their lowest. This is because the fibers are misaligned with the loading axis. However, the *spread* in fiber stresses is the highest at these locations, indicating bending of the curved tow segments. The peak values are obtained elsewhere along the tows: specifically, in regions of neighboring axial tows adjacent to the cross-overs. The ply number (which governs the constraint against bending and straightening) again plays an important role; the peak normalized stress varies from about 1.35 in the single-ply to 1.1 in the two-ply infinite model.

3.5 Discussion

Predictions from the meso-scale models indicate the following effects of the weave on deformation in 8HSW composites under tensile loading. *(i)* Misalignment between the wavy portions of the surface axial tows and the loading axis results in coupled tension and bending within those tows. Bending, in turn, causes strain elevations in the effective medium at the edges of the tow cross-overs, where tow misalignment is greatest (Figure 3.15(a)). *(ii)* Tows misaligned with the loading axis not only experience bending stress, but also tend to straighten (Figure 3.15(b)). Because of the low transverse tow stiffness, this straightening causes elevations in the axial strains within the transverse tows at this location. *(iii)* Tow straightening also produces positive out-of-plane displacement of both the axial and transverse tows at the cross-over. The latter displacement induces tension in the transverse tow along its axis, manifested as positive (tensile) transverse strains above the cross-over. *(iv)* Out-of-plane displacement of the transverse tow at the cross-over is constrained by the two neighboring axial tows on the surface. This leads to transverse displacements and elevations in the local axial stresses in the neighboring tows (Figure 3.15(c)). All of the preceding effects are constrained by neighboring plies and thus vary with the total number of plies.

The maximum stress elevation in the neighboring tows depends on the elastic/plastic response of the effective medium and the number of plies. For the bi-linear stress-strain response employed here, the peak value varies from about 10 % to 35 %: decreasing with increasing number of plies. The effects appear to reach a constant (small) value once the number of plies exceeds about four. The effects are further mitigated upon increasing the matrix modulus.

The experimental measurements of surface displacements and strains are broadly consistent with the model predictions and support the postulated effects of the weave on local deformation. The measurements, however, exhibit variations at nominally equivalent surface sites, likely a consequence of the heterogeneity of the matrix microstructure. More importantly, the *extreme values* in strains and displacements obtained experimentally appear to correlate best with the predictions from the one-ply model. We speculate that this correlation is the result of local separations between surface and interior plies, either present in the pristine material or formed during tow straightening: features that are likely not captured well by the effective medium plasticity model employed here.

The results further suggest that, because of the stress elevations obtained in axial tows adjacent to cross-overs, the strengths of woven composites will be somewhat lower than those of comparable tape laminates (where all fibers are straight and aligned). Although the progression of fiber breakage and coalescence that leads to composite rupture depends on the length scales over which the stress elevations persist as well as the load transfer characteristics between broken fibers and surrounding (intact) material, a worst-case scenario might have rupture occurring at a stress that scales inversely with the relative stress elevation. For instance, if the peak stress elevation is 35 % and failure is assumed (conservatively) to initiate when the local fiber stresses reach their intrinsic bundle strength, the fracture stress would be reduced by a factor of $1 - 1/1.35 = 25\,\%$. A comparable reduction in failure strain might also be expected. Naturally, these estimates neglect the complexity of fiber bundle failure when the fibers are stressed non-uniformly: a problem that remains unresolved.

Notwithstanding the difficulties in directly converting the predicted stress distributions into a composite failure strain, the limited available data on composites probed here and elsewhere appear to support the preceding ideas. For instance, the failure strain of melt-infiltrated HiPerComp$^{\text{TM}}$ composites with Hi-Nicalon fibers in satin weave architectures is 0.74 %; by comparison, the failure strain of comparable HiPerComp$^{\text{TM}}$ composites in tape laminate form is about 0.89 % (Corman and Luthra, 2005). The ratio of these failure strains (1.2) is broadly in line with the fiber stress elevations computed in the present study. Additionally, the failure strain of the satin weave HiPerComp$^{\text{TM}}$ (0.74 %) is higher than that of the present composite (0.65 %). Qualitatively, the latter difference appears consistent with the predicted effects of matrix stiffness and strength on elevations in fiber stress. Specifically, the matrix of the melt-infiltrated HiPerComp$^{\text{TM}}$ composite is significantly stiffer and stronger than the present PIP-derived matrix and would therefore be expected to produce lower fiber stress elevations at the tow cross-overs.

Finally, the validity of the assumptions underlying the binary model formulation—wherein rebar elements represent the axial fiber properties and an effective medium incorporates off-axis properties of *both* phases—has yet to be critically examined for CMCs. This will require more comprehensive comparisons of experimental measurements and model predictions over a broad range of loading scenarios, including not only 0° tension but also 0° shear and 45° tension. Thus, although the model formulation and the constitutive laws employed in the present study produce results that match the various experimental measurements and observations for 0° tensile loading, they may require some refinement in order to capture the behaviors over a broader range of loadings. For instance, because the effective medium elements must incorporate all of the non-fiber axial stiffness and strength as well as the off-axis properties of both phases, an *anisotropic* constitutive law may be required to describe its inelastic behavior. Notwithstanding these limitations, the present model has provided useful insights into the origins and magnitudes of stress/strain concentrations associated with the weave, including the effects of matrix stiffness and strength.

3.6 Conclusions

A meso-scale finite element model has been developed to investigate the effects of the weave on strain and stress evolution in an 8HSW SiC/SiCN composite. The model predictions indicate that stress and strain concentrations develop in response to bending and straightening of the axial tows at the cross-overs. Tow straightening is accommodated by out-of-plane displacement of the tows at the cross-overs, which leads to an elevation in the fiber stress in the neighboring axial tows. The effects are reduced somewhat for multi-ply composites, provided the surface plies do not separate from the internal plies. In the present composite, ply separation is expected to increase the stress elevations from about 10 % to 35 %.

These insights re-affirm the importance of achieving a stiff and strong (fully-dense) matrix in SiC/SiC composites. Low matrix stiffness and strength—features inherent to PIP-based composites—will inevitably result in strain and stress elevations in woven composites.

The results further suggest that weaves with wavier tows, e.g., plain weaves, will not perform as well as the satin weaves. They also imply that some improvement in composite properties might be achieved by tailoring near-surface weaves, e.g., replacing woven plies with unidirectional tapes.

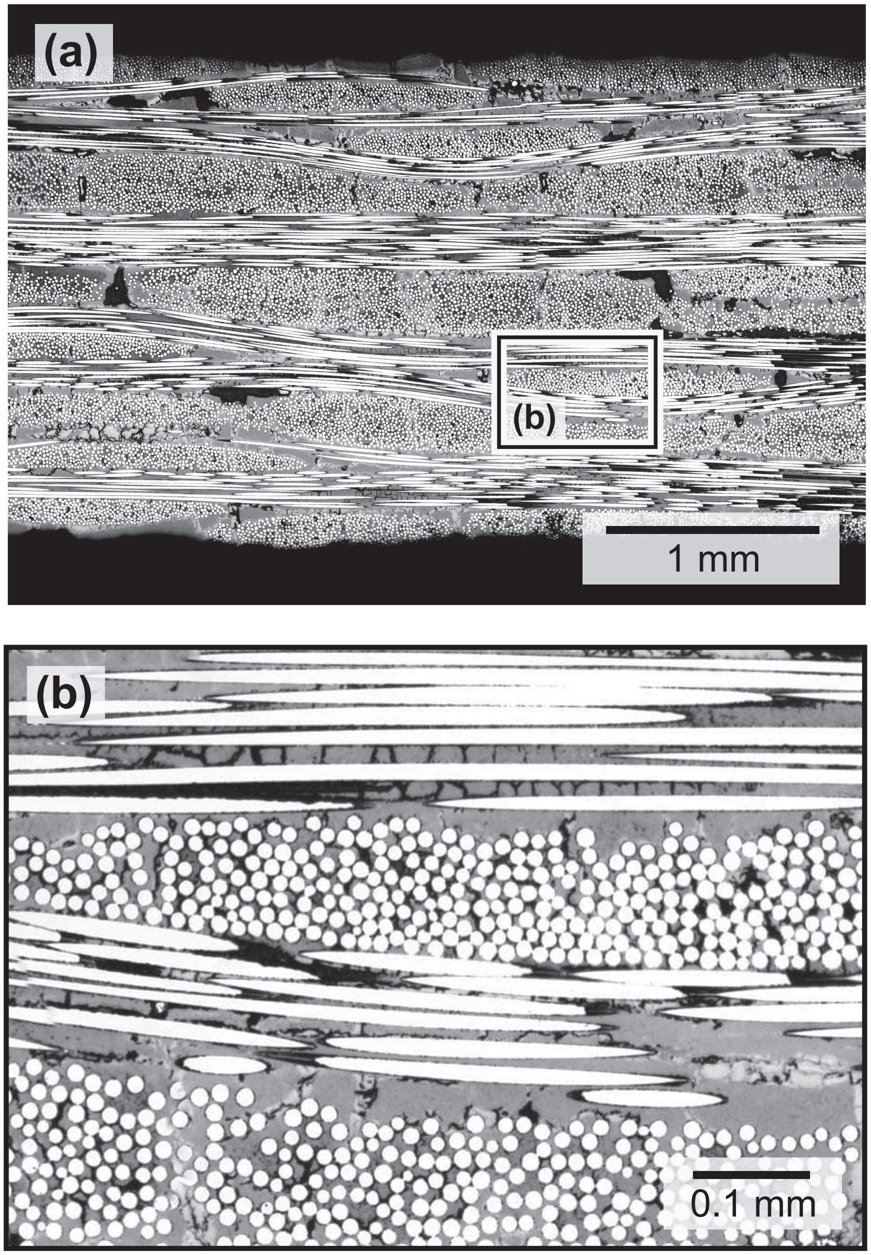

Figure 3.1: Optical micrographs of composite cross-section.

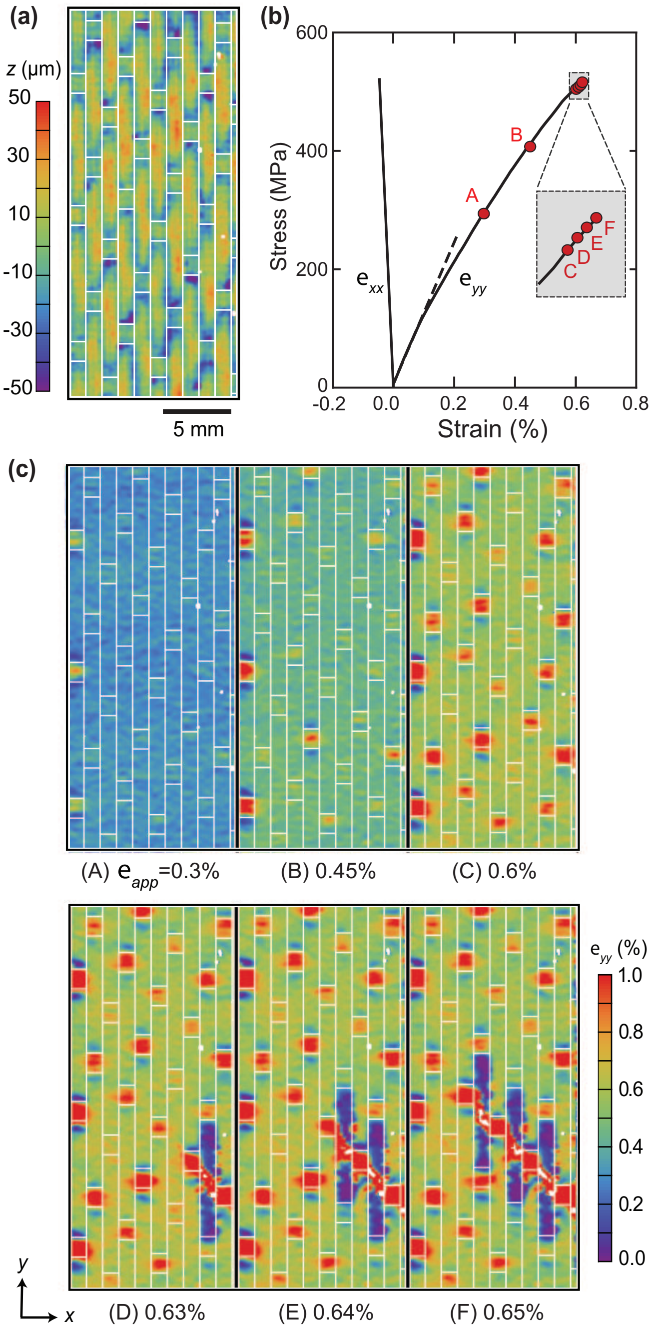

Figure 3.2: (a) Surface topography used to identify boundaries of tows in the surface ply. (b) Global stress-strain response. (c) Corresponding full-field strain maps. Locations of tow boundaries in the surface ply are indicated by the white lines.

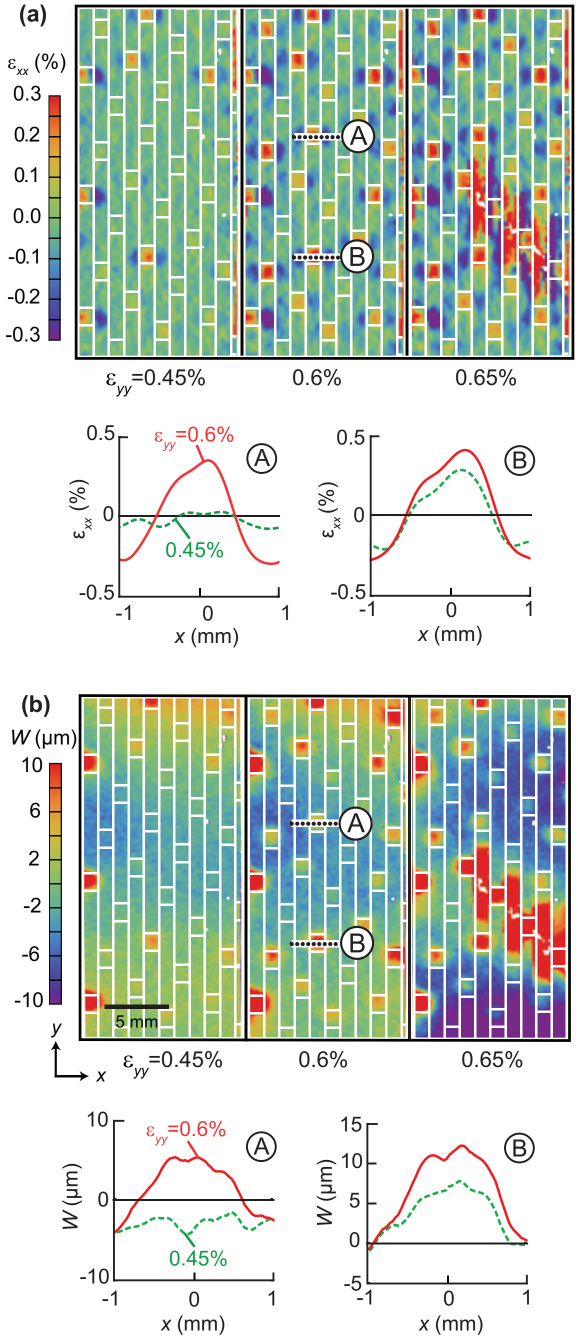

Figure 3.3: Full-field maps and select line scans of (a) transverse strains and (b) out-of-plane displacements.

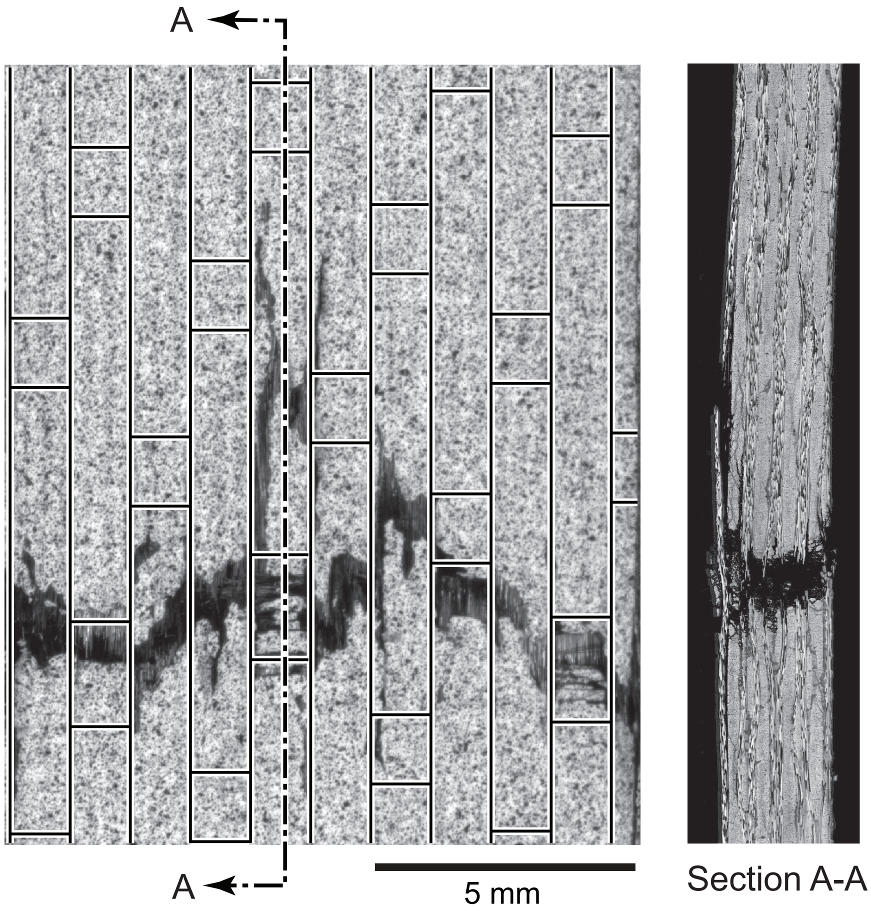

Figure 3.4: Plan view and through-thickness cross-section through fractured specimen.

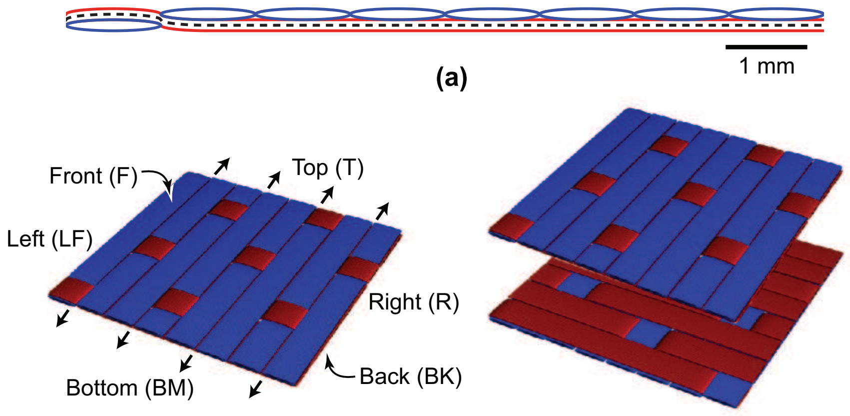

(b) Single-ply **(c)** Two-ply

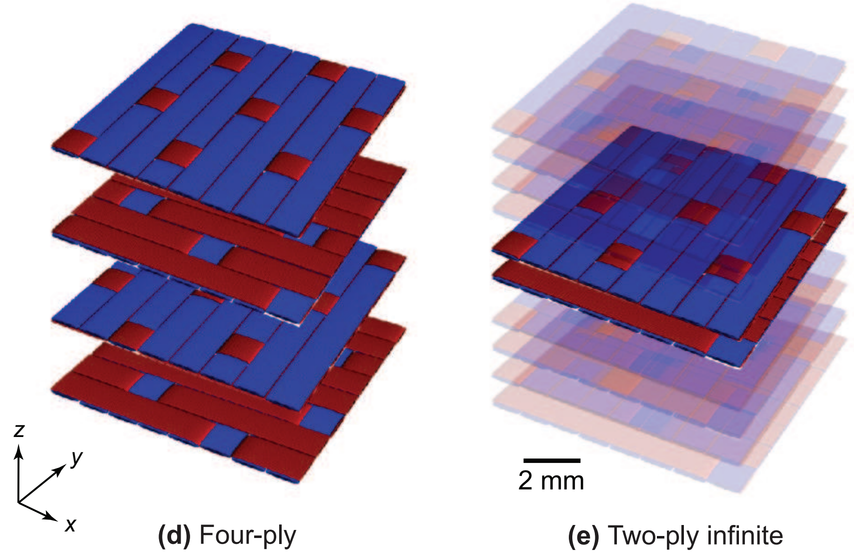

(d) Four-ply **(e)** Two-ply infinite

Figure 3.5: (a) Schematic of tow path and tow shape used as input in generating the tow geometry. Tow architecture and ply lay-ups in: (b) single-ply, (c) two-ply, (d) four-ply (e) two-ply infinite FE models. Designations of boundary faces are shown in (b).

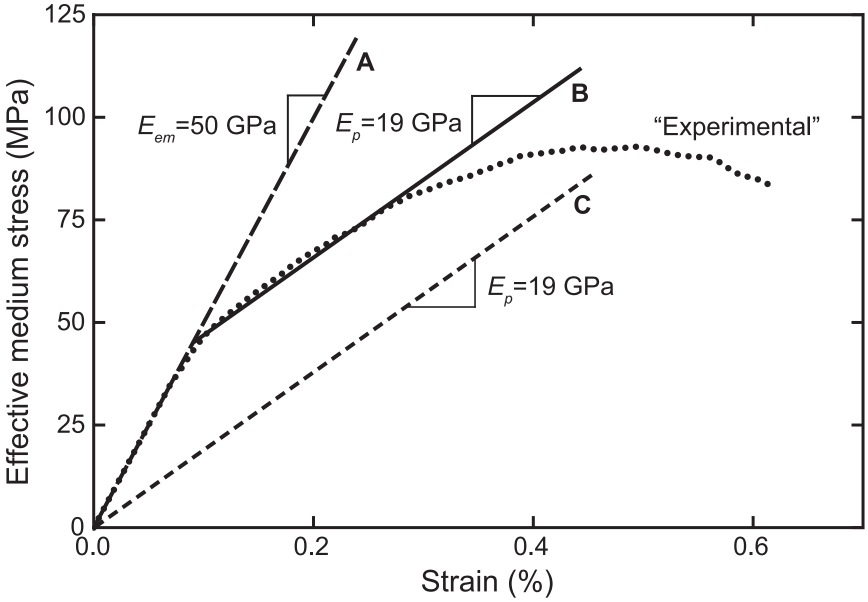

Figure 3.6: Effective medium stress-strain response inferred from the composite stress-strain curve using laminate theory (dotted curve) as well as the three linear/bi-linear idealizations.

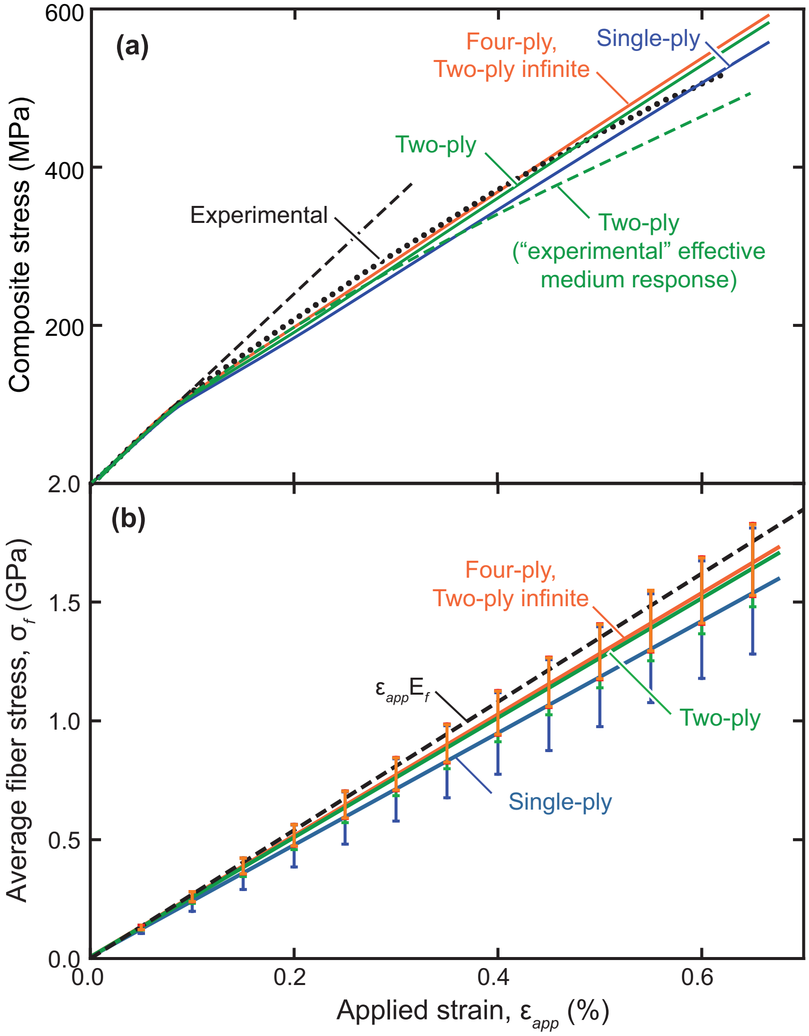

Figure 3.7: (a) Computed and measured tensile stress-strain curves. For four cases, the effective medium response was represented by the bi-linear curve in Figure 3.6 (solid lines). The curves for the four-ply and two-ply infinite models are indistinguishable from one another. In one case, the ″experimental″ effective medium response was used with the two-ply model (dashed curve). (b) Average rebar (or fiber) stress in the axial tows as a function of applied strain. Error bars indicate ± one standard deviation.

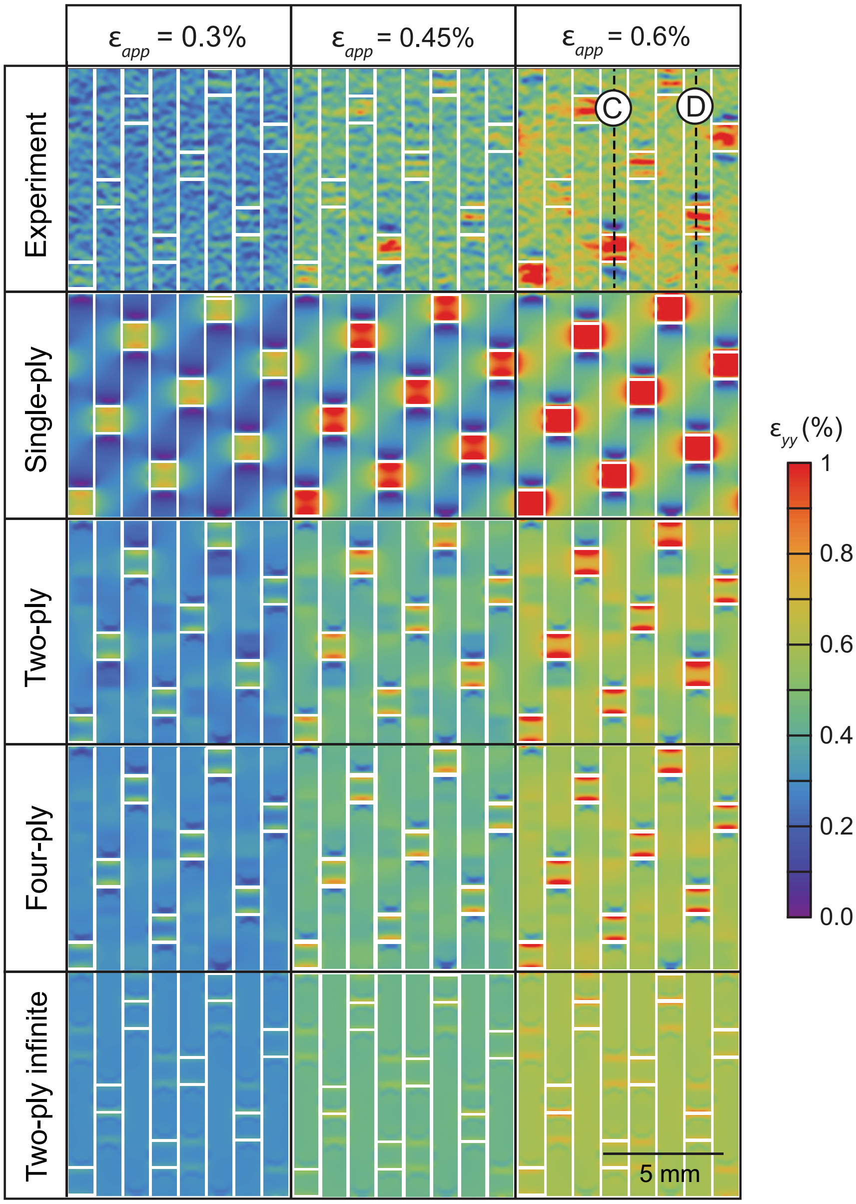

Figure 3.8: Axial surface strains measured by DIC and computed from single-ply, two-ply and four-ply models, as well as the internal strains computed from the two-ply infinite model. Overlaid white lines indicate tow boundaries.

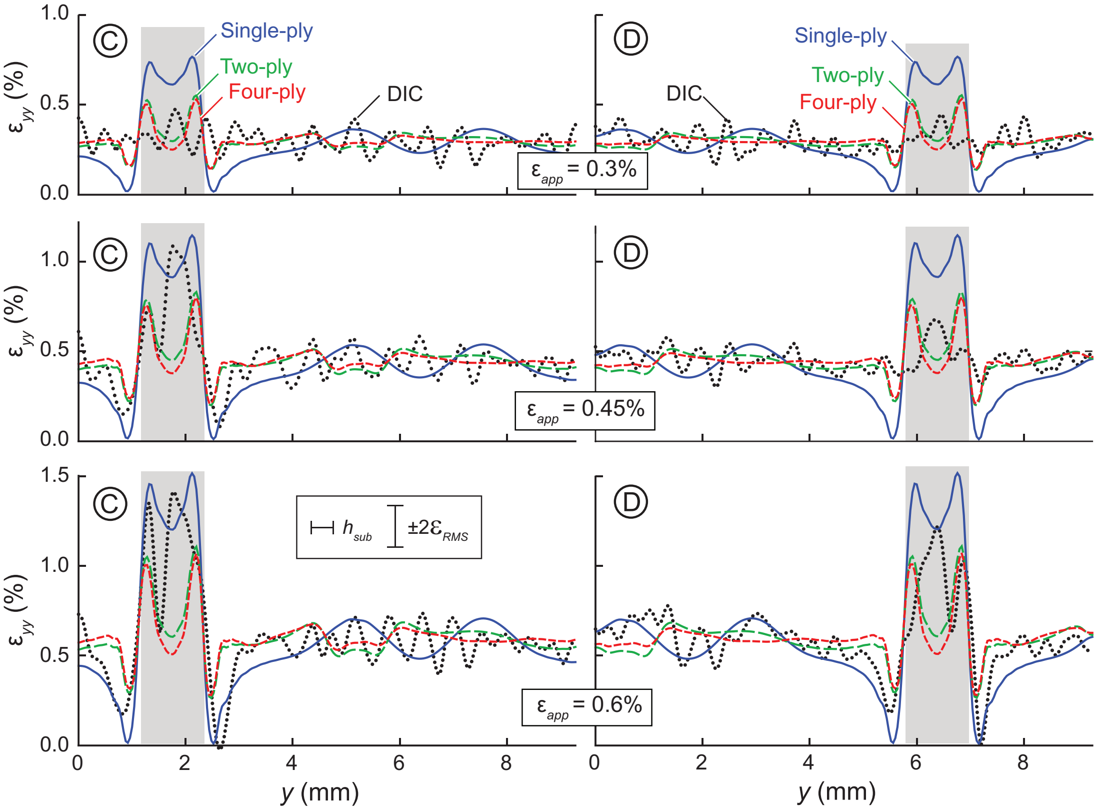

Figure 3.9: Line scans of surface strains from DIC and FE simulations along the trajectories shown in Figure 3.8. The magnitude and wavelength of the measured strains in the nominally straight tow sections is attributable to measurement error. Taking the intrinsic RMS displacement error to be 0.015 pixels, the RMS strain error ε_{RMS} for a 31 pixel (or 0.34 mm) subset size is 0.048 %.The approximate full range of strain error and the magnitude of the subset size are indicated in the inset in the bottom left figure. The shaded bands signify locations of tow cross-overs.

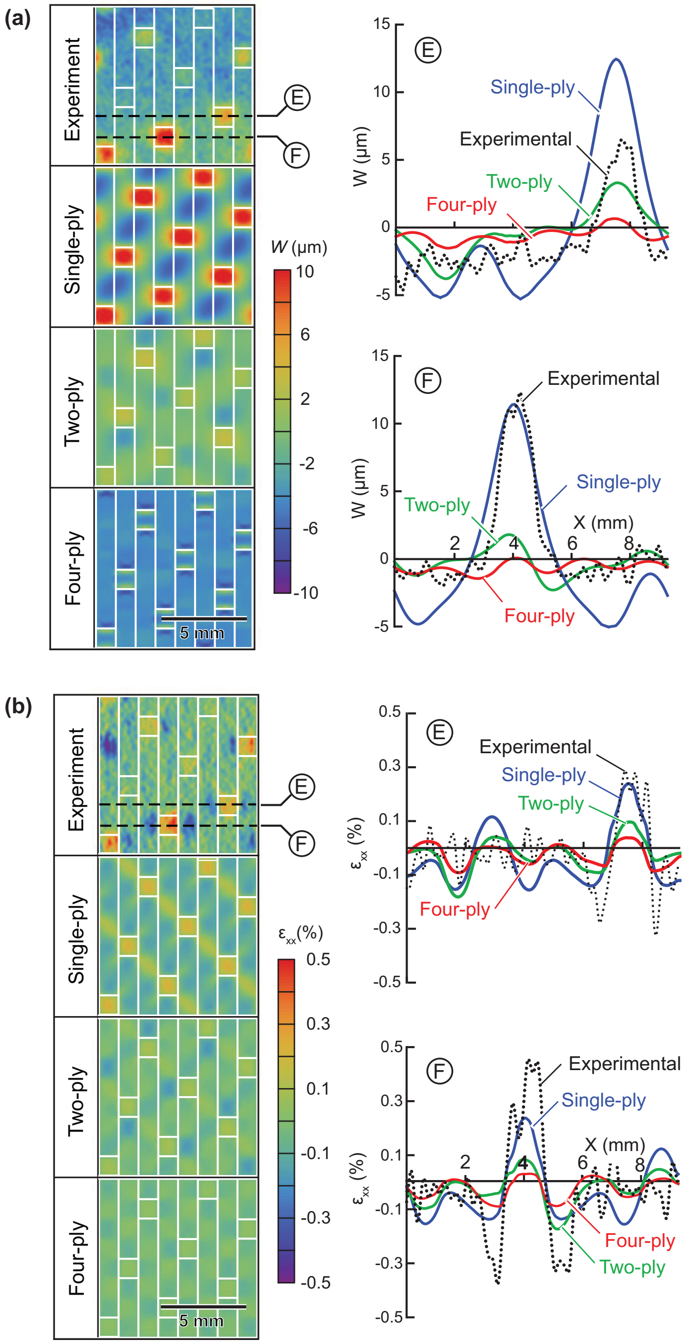

Figure 3.10: Full-field maps and line scans, at $\varepsilon_{app} = 0.6\,\%$, of (a) out-of-plane displacements and (b) transverse strains, measured by DIC and computed by FE.

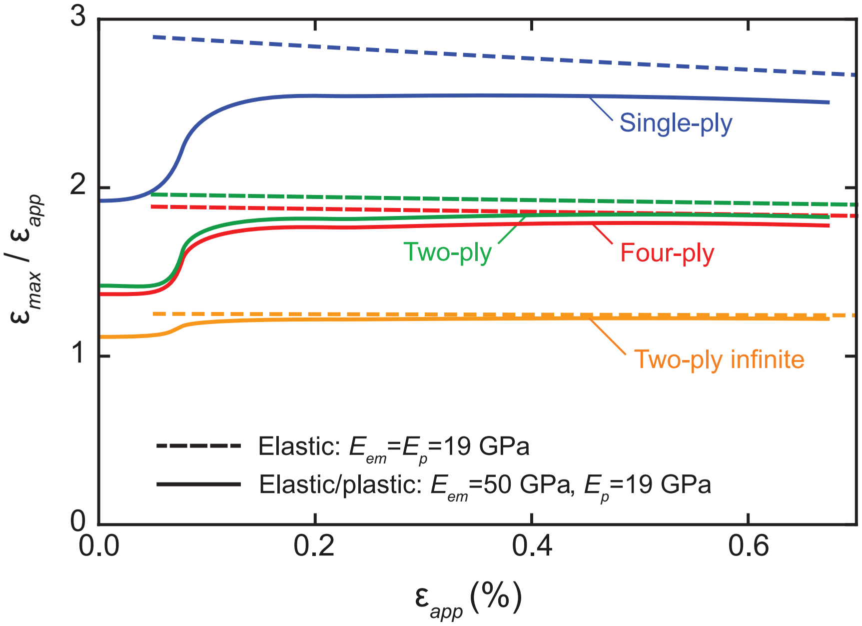

Figure 3.11: Effects of matrix properties and ply number on the variation in strain concentration ($k_\varepsilon = \varepsilon_{max}/\varepsilon_{app}$) on the surface of a tow cross-over with applied strain. The gradual reduction of k_ε with ε_{app} shown by the dashed curves reflects the progressive (albeit gradual) straightening of the underlying axial tow.

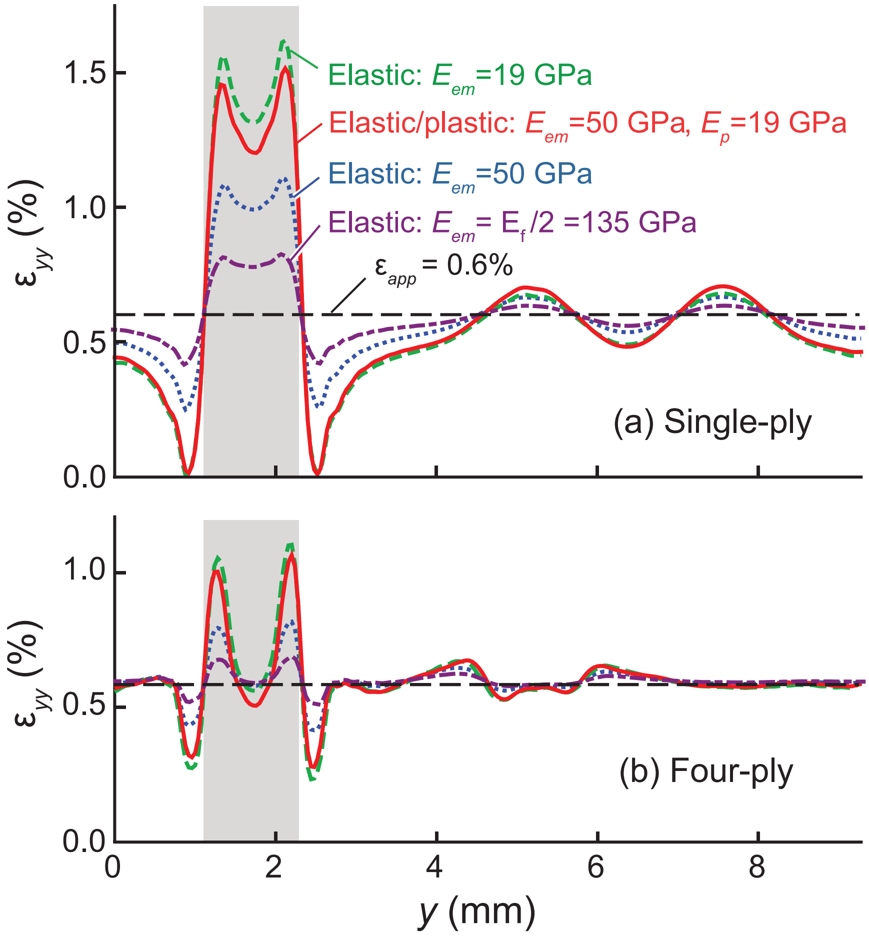

Figure 3.12: Effects of effective medium properties on strain distributions for (a) single-ply and (b) four-ply models, at $\varepsilon_{app} = 0.6\,\%$.

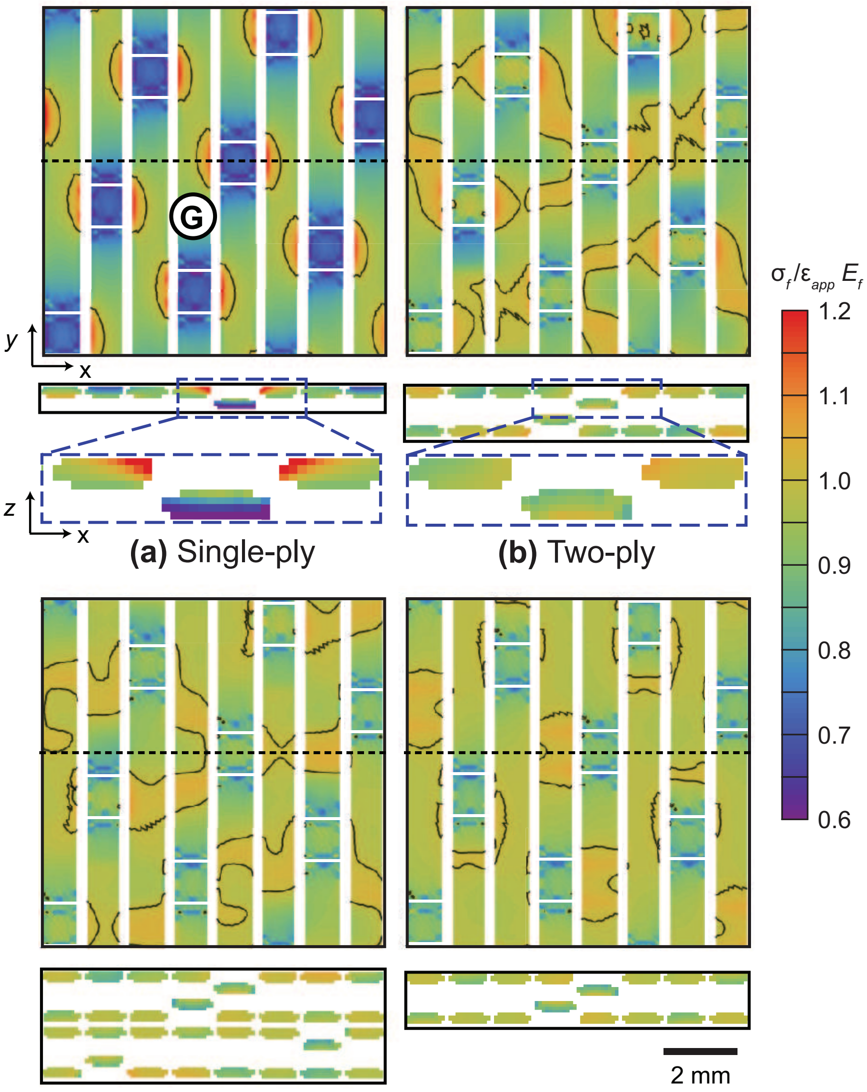

(a) Single-ply **(b)** Two-ply

(c) Four-ply **(d)** Two-ply infinite

Figure 3.13: Normalized fiber stresses, $\sigma_f/\varepsilon_{app}E_f$, in the near-surface axial tows, averaged through the tow thickness, at $\varepsilon_{app} = 0.6\,\%$. Solid lines denote a value of unity. White lines mark the tow boundaries. Normalized elemental fiber stresses are also shown in the transverse cross sections.

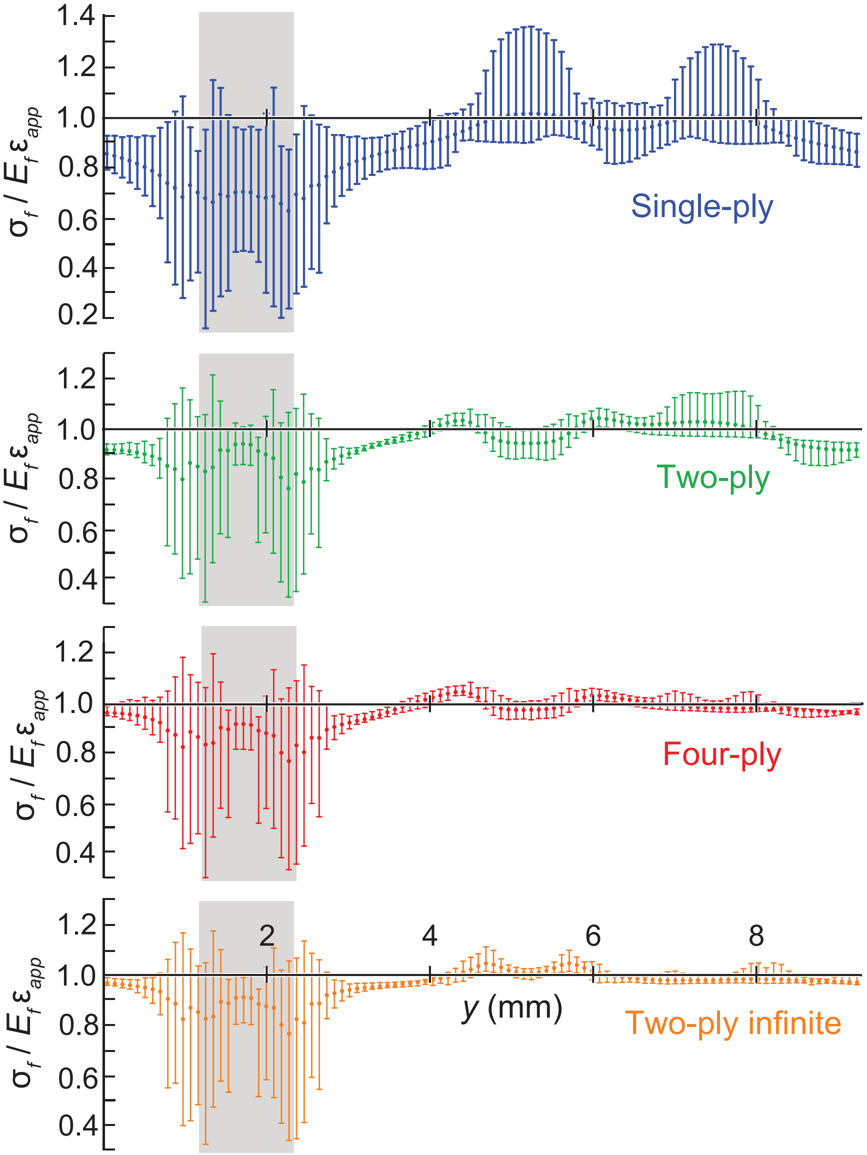

Figure 3.14: Normalized rebar stresses, $\sigma_f / \varepsilon_{app} E_f$, in tow G, indicated on Figure 3.13. Stresses have been averaged across the tow cross-section. Error bars indicate minimum and maximum values within each cross section.

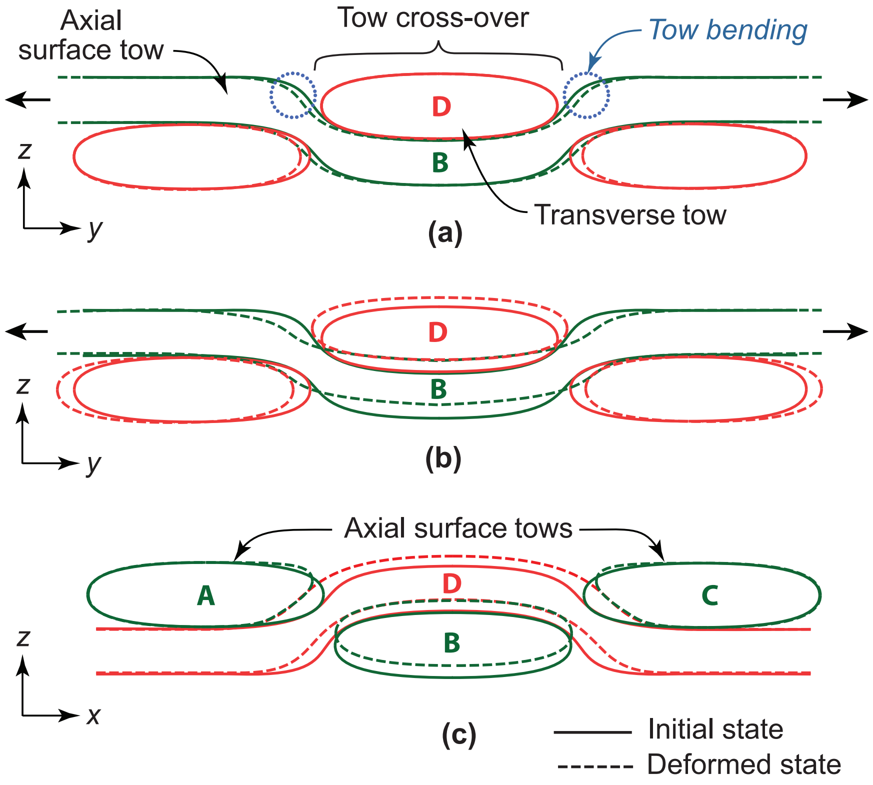

Figure 3.15: Schematics showing: (a) bending of the axial tows at a cross-over; (b) out-of-plane (z) displacement of the axial tow (B) during tow straightening and the resulting displacement of the transverse tow (D) at the cross-over; and (c) the resulting displacement of the two adjacent surface axial tows (A and C).

Chapter 4

Characterizing in-plane geometrical variability in textile ceramic composites

---

This chapter is adapted from the publications: M. N. Rossol, T. Fast, D. B. Marshall, B. N. Cox, and F. W. Zok. Characterizing In-Plane Geometrical Variability in Textile Ceramic Composites. *Journal of the American Ceramic Society*. Available at: `http://dx.doi.org/10.1111/jace.13275`; M. N. Rossol, J. H. Shaw, H. Bale, R. O. Ritchie, D. B. Marshall, and F. W. Zok. Characterizing Weave Geometry in Textile Ceramic Composites Using Digital Image Correlation. *Journal of the American Ceramic Society*, 96(8):2362–2365, 2013. Available at: `http://dx.doi.org/10.1111/jace.12468`; and J. H. Shaw, M. N. Rossol, D. B. Marshall, and F. W. Zok. Effect of Tow-Scale Holes on the Mechanical Performance of a 3D Woven C/SiC Composite. *Journal of the American Ceramic Society*. Available at: `http://dx.doi.org/10.1111/jace.13389`

4.1 Introduction

One of the desired attributes of 3D woven CMCs is the ability to tailor the weave architecture to best match the anticipated thermal and mechanical stress fields. But with the added complexity inherent in 3D weaves comes the possibility of increased variability in the weave architecture. As noted in Chapter 3, the weave architecture plays an important role in the onset of damage. Therefore, understanding the nature of weave variability is a key issue that must be addressed in order to properly assess the thermomechanical performance of 3D woven CMCs.

Synchrotron X-ray computed tomography (CT) has been shown to provide exquisite detail in the geometric characteristics and defects with ca. μm resolution in woven ceramic composites (Bale et al., 2012; Blacklock et al., 2012; Rinaldi et al., 2012). It has been used to establish statistical descriptors of the shapes and positions of tows (Bale et al., 2012). In turn, these descriptors have been used in conjunction with a probabilistic geometry generator to create virtual specimens with the same statistical characteristics as those obtained from the CT images (Rinaldi et al., 2012). In this way, the effects of defect distributions on thermal and mechanical performance can be probed computationally (Blacklock et al., 2012). Despite the richness of information extracted from CT images, the technique has one major drawback: that of severely-restricted volume and shape of specimens that can be characterized. While extensive work has been done in the textile community to enable automated detection of defects in large woven material, the techniques are fundamentally qualitative, with defects only needing to be identified and located, not quantified and characterized (Campbell and Murtagh, 1998; Chan and Pang, 2000; Jasper and Potlapalli, 1995; Mak et al., 2009).

The objective of this chapter is to present a methodology for characterizing long-range weave defects using a complementary characterization technique, based on surface topography mapping via 3D DIC . Although DIC mapping is inherently limited to characterization of external surfaces, the surfaces of woven composites of interest (described below) constitute a significant fraction of all tow surfaces. Consequently, the technique is expected to provide substantial information (though clearly not comprehensive) on geometric tow defects that cannot be gleaned from μCT imaging alone.

The outline of the chapter is as follows. The surface topography of a 3D woven CMCs measured using 3D DIC is compared with data obtained from μCT. The comparison is used to guide the proper choice of correlation parameters in order to minimize measurement error, while retaining the needed spatial resolution. Procedures are developed for acquiring and stitching multiple DIC data sets in order to characterize large panels. Analytical methods are presented for characterizing deviations of the weave from a hypothetical perfectly-periodic structure using the positions of one population of surface tows as fiducial markers. The methods include partitioning of the deviations into short- and long-range components, calculation of their spatial derivatives (to enhance the visibility of the short-range components) and spectral analysis of the derivatives using Discrete Fourier Transforms. Panel curvatures also emerge from these analyses. The methods are demonstrated on a composite panel that appears quite regular to the unaided eye. Finally, the methods are applied to characterize panels with other weave features, including holes and shear defects.

While demonstrated here for a representative 3D woven ceramic matrix composite, the methods are applicable to any woven or braided product with nominally periodic architecture. The shorter range variations in tow packing density reported below are concluded to be generated by the weaving machinery and therefore might be endemic to weaves. Indeed, qualitative characteristics are very similar to those reported elsewhere for 2D twill weaves of carbon fibers intended for use with polymer matrices (Vanaerschot et al., 2014).

4.2 Characterizing surface topography using DIC

4.2.1 Materials and experimental methods

The material of interest is a woven three-layer angle interlock C-SiC composite (Bale et al., 2012; Blacklock et al., 2012; Rinaldi et al., 2012). The fiber preform consists of T300-6K tows in the configuration depicted in Figure 4.1. The fibers (each of diameter 7 µm) had been coated with a thin layer of pyrolytic carbon (as a debond layer) via chemical vapor infiltration (CVI). The preform was then partially infiltrated with CVI SiC, resulting in a 40 µm-thick matrix layer around the fiber tows. The tows are approximately elliptical in cross section ($\sim 1\,\mathrm{mm} \times 0.2\,\mathrm{mm}$). The surface of the CVI SiC surrounding each tow is textured with fine striations ($\sim$ 100 µm wide) replicating positions of underlying fibers. In this (partially-processed) state, the fiber tow boundaries can be readily discerned in the synchrotron images and the external surfaces of the panel present an accurate depiction of the local tow positions.

The results of CT imaging have been presented elsewhere (Bale et al., 2012; Blacklock et al., 2012; Rinaldi et al., 2012). The test specimen had been imaged using monochromatic X-rays with 21 keV energy at the Advanced Light Source (Lawrence Berkely National Laboratory, Berkeley, CA). The specimen was 1.3 mm thick and 8 mm wide. Five tiled scans covering a height of 13 mm were conducted. The specimen comprised the equivalent of about two unit cells of the fiber weave. A commercial re-construction code (Octopus v8, IIC Ugent, Belgium) was used to create a set of two-dimensional slices normal to the rotation axis. The surfaces of the sample were identified by binarizing each two-dimensional slice to maximize contrast between the sample surface and the background and then locating the outermost pixels with a value not equal to that of the background. Visualization of re-constructed surfaces and associated computations were performed using Mathematica®(Wolfram Research, Campaign, IL).

Both surfaces of the same test coupon were characterized by DIC using procedures presented in Chapter 2. High-contrast speckle patterns were produced on the (black) specimen surface using an airbrush with white water-soluble paint. The average speckle size, determined by the autocorrelation technique, was approximately 50 ± 10µm. Images for DIC were acquired using two digital cameras (Point Grey Research Grasshopper, Richmond, BC, Canada), each with a CCD resolution of 2448×2048 pixels and a 70–180 mm lens (Nikon ED AF Micro Nikkor, Nikon Inc., Melville, NY). The experimental set-up and imaging conditions were selected to ensure that the entire coupon surface was in the focal plane of both cameras and that the highest possible magnification was attained. To achieve these goals, the lens focal length was 180 mm, the aperture setting was F-22, the magnification was 10 µm/pixel and the angle between cameras was 19°.

Image correlation was carried out using VIC-3D software (Correlated Solutions, Columbia, SC), employing the smallest possible step size (2 pixels, 20 µm) and subset sizes ranging from 21 to 91 pixels. The latter range was selected to assess the trade-offs between spatial resolution and degree of correlation. The intrinsic noise in the height measurements was characterized by the root-mean-squared (RMS) difference between height measurements, obtained from sequential image pairs that had been taken without altering imaging conditions. Variations in degree of correlation and RMS error with subset size (plotted in Figure 4.2) reveal a near-optimal subset size of 31 pixels, whereupon 99 % of subsets are successfully correlated and the RMS error is 1–1.5 µm (smaller than the CT voxel size: 4.4 µm). As demonstrated below, this noise level is about an order-of-magnitude lower than the RMS differences between surface heights obtained by DIC and CT. Increasing the subset size yields negligible benefit in terms of improved correlation or noise reduction. On the contrary, as shown below, it leads to increased errors in surface height measurements. Consequently, most results presented subsequently are based on correlations made with this subset size.

In order to perform quantitative comparisons, the coordinates defining the surface profiles obtained by each of the two techniques were aligned with one another using the locations of the peaks of the warp crowns as fiducial markers. The translations and rotations about the principal axes needed to align the data sets were determined by minimizing the sum of the squares of the Euclidean distances between the peaks of the warp crowns obtained from CT and DIC measurements. The standard deviation in warp crown heights from CT and DIC following alignment was 3.7 µm. Assessments of the DIC technique were made on the basis of 3D renderings of the surfaces, line-scans of surface heights and residuals between the two data sets.

4.2.2 Re-constructed surfaces

3D renderings of re-constructed surfaces from both CT and DIC are shown in Figure 4.3. Qualitatively the DIC results appear to provide an excellent representation of the sample surface, as determined by CT, with the exception of the fine surface striations. The inability to capture the striations is due largely to the combination of attainable speckle size (50 µm) and subset size (31 pixels, 310 µm) needed to attain full correlation.

Quantitative comparisons between the two surfaces are presented in the form of line scans of surface heights in Figure 4.4. Here we find that, in regions further than $\sim$ 100 µm from the boundaries between adjacent tows, the differences are typically $<$20 µm. Closer to the boundaries, where the surfaces exhibit rapid changes or discontinuities in height, the differences between CT and DIC are somewhat greater, but still typically <50 µm.

A more comprehensive assessment of the fidelity of the DIC-derived surfaces was made by computing the RMS errors over the entire surface (comprising >200,000 data points) over a subset size range of 21–91 pixels (Figure 4.5). The error was computed in two ways. The first was based on all surface data. In the second, a subset of those surface regions located more than 0.15 mm from a tow boundary was isolated and analyzed accordingly. The isolated regions for the latter case and the RMS errors are shown in Figure 4.5. Neglecting the boundaries, the error is essentially constant, at $\sim$ 10 µm, up to a subset size of 50 pixels (0.5 mm). This level of error is only about twice the CT voxel size - the latter setting the accuracy on the baseline true surface heights. Including the entire surface yields somewhat higher errors at small subset sizes (e.g. 20 µm at a subset size of 31 pixels) and a progressive increase in error with subset size (approximately linear): differences attributable to errors in resolving tow boundaries.

The main sources of error in the preceding comparisons include: *(i)* the spatial resolution of the CT (roughly half the voxel size: $\sim$ 2 µm); *(ii)* the intrinsic noise in the DIC images ($\sim$ 1 µm); *(iii)* the disregistry between the DIC and CT images ($\sim$ 4 µm); and *(iv)* the spatial resolution of the DIC measurements and the associated smoothing of fine surface features (i.e. curvature of tows and fine surface striations). Although the convolution of these effects in overall measurement error is complex, it would appear that, based on addition of variances, a measurement error of 10 µm is likely to be the best one could expect to achieve from such experiments with analysis areas of several cm^2.

4.3 Application to panel characterization

4.3.1 Measurement methods

The preceding test methods were used to characterize a large panel of the three layer angle interlock C/SiC composite. The panel had dimensions 157 mm × 116 mm in the weft and warp directions, respectively, and an average thickness of 1.36 mm. Some modification to the methods were made in order to accommodate the large panel size.

Speckle patterns were created using the same technique described above, but with a different airbrush. The resulting speckles were slightly larger, with an average size of approximately 100 µm (Rajan et al., 2012). Images were acquired using a focal length of 70 mm, aperture setting of F-16, and a magnification of 23 µm/pixel. The angle between the cameras was 27°. To retain high resolution, images were taken of sub-sections of the surface (47 mm × 56 mm in size) and subsequently stitched together using methods described below. To facilitate stitching, an overlapping region about 10 mm wide was included in adjacent images. With the present selection of imaging parameters and the panel dimensions, twelve image pairs were required to characterize each of the two panel faces. The images were correlated with a subset size of 21 pixels and a step size of 2 pixels. The raw topographic data, represented by the function $z(x, y)$ relating surface height z to in-plane coordinates x and y, were exported from VIC-3D, with subsequent data stitching and further analysis performed using Mathematica®(Wolfram Research).

Stitching of two adjacent data sets requires that both be in the same reference frame. This goal was accomplished by first identifying three distinct speckles (to serve as fiducial markers) in the overlapping field and then re-positioning one of the images in-plane such that speckles were brought into alignment. The requisite positional shifts and rotation were determined by minimizing the sum of the squares of the Euclidean distance between each pair of points in the two images. Following re-positioning in-plane, the images were shifted in the z-direction so that the mean surface heights in the two images were the same. The shift needed in the z-direction is determined from coincident line scans taken along the center line of the overlapping region between the two data sets (Figure 4.6). Excellent agreement is seen between line scans of the repositioned data sets (Figure 4.6(c)). This illustrates the efficacy of the stitching process and the absence of artifacts arising from image distortions. For the purpose of the segmentation operations described below, the data for each panel face were auto-plane fit, to move them from the plane of the camera CCD to the $x - y$ plane. The full topographic map for one panel face constructed in this manner is shown in Figure 4.7.

4.3.2 Segmentation of data

The present weave consists of four distinct genuses of fiber tows (Rinaldi et al., 2012), three of which appear on the specimen surface: surface wefts, center wefts, and warp tows (Figure 4.1(a)). The portions of tows that are visible on the surface exhibit characteristic variations of height and outline in the $x - y$ plane. Although the height ranges for different tow genuses overlap, automated attribution of each visible tow segment to a particular genus was possible by combining height and shape information. The data were segmented into sub-sets for each tow genus using the following procedures.

First, common features were brought to comparable heights over the entire panel area by subtracting from each $z(x, y)$ value the mean *local* surface height $\overline{z}_{local}(x, y)$, computed over an area of one unit cell centered on (x, y). The warp tows and the surface wefts, which generally stand higher than the central wefts on the surface, were separated from the latter by thresholding the distribution of the quantity (Figure 4.8(a)). The warp tows and surface wefts were then classified using information about the aspect ratios of the outlines formed by the thresholding procedure: the average aspect ratio of the warp crowns is slightly greater than unity whereas that of the surface wefts is less than 0.5. The distributions in aspect ratios are plotted in Figure 4.8(b) and the segmented warp and surface weft tows are shown in Figure 4.8(c).

The outlines formed by thresholding are more consistent for warp tows, which appear on the surface as relatively regular crown features than they are for weft tows. Therefore, the segmented domains formed by thresholding data for warp tows were used exclusively for analyzing weave characteristics.

An ancillary result of computing local heights averaged over a unit-cell gauge length is the spatial distribution in averaged surface heights $\overline{z}_{local}(x, y)$; fitting the data yields the two principal curvatures of the panel and their directions. The results for the two panel faces, plotted in Figure 4.9, show that the principal curvatures are aligned approximately with the fiber directions. Additionally, the slight differences in the surface heights on the two faces indicate slight non-uniformity in the panel thickness. Examinations of corresponding line scans on the two faces (not shown) indicate that these variations are no greater than about 40 μm.

4.3.3 Definition and interpretation of warp crown positions

Analysis begins by computing the position (x_i, y_i) of the centroid of the segment area for each of N visible warp crowns, with $i = 1, \ldots, N$. [2] This position represents the mid-point of the intersection of the projections on the $x - y$ plane of the warp tow visible on the surface and the underlying weft tow. With the y-axis assigned to the weft direction, variations in the component y_i describes lateral shifts in the position of the warp tow, while variations in the component x_i describes lateral shifts in the position of the underlying weft tow (Figure 4.10). Any shifts of either the warp or weft tows along their own axes remain undetermined.

Since the fabricated product was intended to be and is often modeled as being regular and periodic, it is useful to extract from the stochastic data an ideal perfectly-periodic structure and regard the measured textile as being a deviation from this perfect structure. The ideal structure is one that would be used in non-stochastic modeling of the composite to predict mean composite properties. The degree to which the real material departs from the ideal should correlate with the measured scatter in properties if that scatter is due to variations in the weave structure.

---

[2] An alternative choice of position to represent a warp crown segment is that at which the surface height is maximum within the segment. The maximal positions were calculated by fitting the data to a second-order polynomial. The resulting positions were almost indistinguishable from those obtained from the tow centroids. For computational expediency, the centroid method is preferred.

The determination of the unit cell size and orientation for the hypothetical ideal is described below. Each warp crown position (x_i, y_i) can be regarded as shifted by a deviation vector (u_i, v_i) from the location $(\overline{x}_i, \overline{y}_i)$ that the warp crown would have in the hypothetical ideal:

$$(x_i, y_i) = (\overline{x}_i, \overline{y}_i) + (u_i, v_i) \tag{4.1}$$

All analysis is conducted using the array of positions (x_i, y_i) or deviations (u_i, v_i), which are defined over a periodic grid, $(\overline{x}_i, \overline{y}_i)$, with four grid points (four warp crowns) per unit cell of the fabric (the unit cell is defined as the smallest orthorhombic repeat unit of the ideal weave structure, Figures 4.1 and 4.8).

4.3.4 General weave characteristics

Figures 4.7 and 4.8 confirm that the weave is an approximately periodic structure. Other broad characteristics of the fabric can be seen by collating the projections of the trajectories of all warp and weft tows onto the $x - y$ plane, shifted in space to bring all of the warp and all of the weft tows separately into coincidence at one end (Figure 4.11). The results show that: (i) the projected trajectory of each tow is not straight over length scales larger than the unit cell dimensions but instead follows a curved path; (ii) the projected trajectories of warp tows appear similar to one another when viewed at the macroscopic scale (Figure 4.11(a)); and (iii) the projected trajectories of weft tows also appear similar to one another (Figure 4.11(b)). The implication is that each tow population has undergone long-range cooperative deviation from its intended path. In addition to the long range trends, scatter among the projections indicates short-range positional fluctuations.

The average unit cell in the actual weave structure is defined by the two vectors r_1 and r_2 along the warp and weft directions. These vectors are obtained by determining the average vector connecting neighboring crowns on all warp and weft tows. The mean and standard deviations of their magnitudes over the entire panel area are $r_1 = \lambda_{warp} = 7.52 \pm 0.06\,\text{mm}$ and $r_2 = \lambda_{weft} = 5.05 \pm 0.05\,\text{mm}$. The average angle between warp and weft tows, obtained from the lattice vectors, is $\theta_{av} = 89.65^\circ \pm 0.06^\circ$.

The direction of r_2 (parallel to the weft tows) was taken to be the y-axis of the specimen; the x-axis was set to be orthogonal to the y-axis. These directions and the lattice dimensions λ_{warp} and λ_{weft} define the ideal weave structure to which the deviations of Eqn. (4.1) refer. The axes in Figure 4.12 and other data plots are these axes of the hypothetical ideal.

4.3.5 Long and short range deviations

Plots of the deviation data, rendered as quasi-continuous quantities by interpolating the arrays (u_i, v_i), show that the largest amplitude deviations are associated with variations that span the entire specimen (Figure 4.12). Lower amplitude variations (mild color changes between the discrete contour lines in Figure 4.12) occur over shorter spatial gauges.

The visibility of short wavelength variations relative to those with longer wavelengths can be enhanced by spatial differentiation, which serves as a filter. Spatial derivatives of the deviations were computed at each grid point $(\overline{x}_i, \overline{y}_i)$ from the slopes of planar functions $u_i(x, y)$ and $v_i(x, y)$ fitted using the least squares method to the deviations (u_j, v_j) at a set of grid points within an area bounded by a unit cell of the weave structure centered on $(\overline{x}_i, \overline{y}_i)$ (Figure 4.1(b)). The spatial derivatives of most interest are: (i) $\delta_{xx} = \partial u / \partial x$, which gives a direct measure of fluctuations in the packing density of weft fiber tows,[3] (ii) $\delta_{yy} = \partial v / \partial y$, which gives a direct measure of fluctuations in the packing density of warp fiber tows, and (iii) $\delta_{xy} = (\partial u / \partial y + \partial v / \partial x)/2$, which is equal to one half of the cotangent of the angle, θ, between the warp and weft tows. In the event that the deviations were caused by mechanical deformation of the preform after completion of weaving, the derivatives δ_{xx}, δ_{yy}, and

---

[3] $\delta_{xx} = \rho^o_{weft} / \rho_{weft} - 1$, where ρ_{weft} is the packing density of the weft tows and ρ^o_{weft} is the average packing density of the weft tows. Similarly, $\delta_{yy} = \rho^o_{warp} / \rho_{warp} - 1$.

δ_{xy} can be regarded as tensorial strains ε_{xx}, ε_{yy}, and ε_{xy} in a quasi-continuous material, which are meaningful over gauge lengths somewhat larger than the tow spacing. Otherwise, if produced by the weaving process, δ_{xx}, δ_{yy}, and δ_{xy} represent the variances intrinsic to the weaving operation. Maps of these derivatives, rendered as continuous functions by interpolating the arrays of values at the grid points $(\overline{x}_i, \overline{y}_i)$, are shown in Figure 4.13.

The map of δ_{xy} in Figure 4.13(c) shows long-range variation in the angle between the warp and weft tows along the x-direction, but minimal variation along the y-direction. As discussed above, this systematic variation is attributable to shear deformation during handling after weaving. The magnitude of the shear strain increases approximately linearly with the distance x with a gradient of $0.000\,22\,\mathrm{mm}^{-1}$. The average shear strain over the area analyzed is 0.003, corresponding to an angle $\theta = 89.65^\circ$ between the warp and weft tows.

Superimposed on the long-range variations inδ_{xy} in Figure 4.13(c) are short-range fluctuations over length scales on the order of several unit cell lengths, presumably introduced during the weaving operation. The magnitude of these fluctuations ($\sim$ 0.005) is about $1/4$ of the long-range variation across the field (approximately 0.02).

The map of δ_{xx} in Figure 4.13(a) shows a similar long-range gradient

($0.000\,26\,\mathrm{mm}^{-1}$) in the x-direction (along the warp tows). This variation could also be caused by inadvertent fabric deformation after weaving. Because of the waviness of the warp tows, deformation parallel to the fibers would be relatively easy. Here, again, short-range fluctuations in δ_{xx} are superimposed on the long-range variations. In contrast, the map of δ_{yy} in Figure 4.13(b) shows only short-range fluctuations. This is consistent with the expectation that, with the weft tows being essentially straight, deformation parallel to the wefts would be difficult.

For further analysis, the long-range deviations (those with wavelength larger than the specimen width) were subtracted from the deviation data in Figure 4.12, then the spatial derivatives of the remaining short-range deviations were calculated. The resultant maps are shown in Figure 4.14. (The long-range deviations were determined by fitting bi-quadratic functions to the deviations.) In this form, the derivatives δ^S_{xx} and δ^S_{yy} represent variations in the relative short-range packing densities of the warp and weft tows, which are likely inherent to the weaving process.

The maps in Figure 4.14 exhibit highly anisotropic spatial variations, *i.e.*, with very different dependencies on x and y. The anisotropy arises because the continuity of fibers tends to dampen positional deviations along the tow direction but not transverse to it. Variations in $\delta^S_{yy}(x,y)$ tend to be smaller in the x-direction than in the y-direction. Conversely, variations in $\delta_{xx}^{S}(x, y)$ tend to be larger in the x-direction than in the y-direction. Thus, variations in $\delta_{yy}^{S}(x, y)$ and $\delta_{xx}^{S}(x, y)$ normal to their respective tow direction can be meaningfully subjected to spectral analysis, whereas those along the tow direction cannot (at least in specimens of the current size). An analysis that recognizes the anisotropy in the richness of data follows.

4.3.6 Fourier analysis of variation of tow packing density

The short-range fluctuations in δ_{xx}^{S} and δ_{yy}^{S} were quantified by Fourier analysis. First, each set of data was interpolated to create a data set on a regular grid with spacing $\lambda_{warp}/4$ along all of the warp tows and $\lambda_{weft}/4$ along the weft tows. Discrete Fourier Transforms (DFTs) were then evaluated for $\delta_{xx}^{S}(x)$ (fluctuations of weft packing density) along successive lines above each warp tow (120 lines, each containing 44 data points) and for $\delta_{yy}^{S}(y)$ (fluctuations of warp packing density) along lines above the weft tows (44 lines, each containing 120 data points). This yielded a set of Fourier coefficients for each warp line of amplitude $A_m^{(x)}(s)$ and phase $\phi_m^{(x)}(s)$, and for each weft line of amplitude $A_m^{(y)}(s)$ and phase $\phi_m^{(y)}(s)$, where the index m refers to one scan line in the data array and s is the spatial frequency $(s = 1, \ldots (n+1))$, with n the number of data points along the line. The spatial frequencies are defined by a wavenumber k and a wavelength λ:

$$\kappa(s) = \frac{2\pi}{\lambda(s)} = \frac{2\pi}{L}(s-1) \tag{4.2}$$

where L is the length of the line.

Comparison of the phases and amplitudes of the Fourier components for all of the warp tows and all of the weft tows indicated substantial stochastic variability. The results are summarized in Figure 4.15, as mean values and standard deviations for each spectral component. Components with significant amplitude are present with wavelengths ranging from the unit cell size ($s = n/4 + 1$ and $n - n/4$) to the specimen width ($s = 2$ and $n - 1$). On cursory examination the variation of the amplitude of the Fourier components with s appears qualitatively similar for $\delta^S_{xx}(x)$ and $\delta^S_{yy}(y)$. The distributions of phase angles show very large variances. While only half of the spectral components plotted in Figure 4.15 are unique (due to symmetry of the Fourier coefficients about $s = 1 + n/2$), all are needed during the reconstruction of virtual specimens discussed below.

4.3.7 Generation of stochastic virtual specimens

The preceding spectral analysis for characterizing the tow density variations, $\delta^S_{xx}(x)$ and $\delta^S_{yy}(y)$, can be used as a basis for developing simple algorithms for generating ensembles of stochastic virtual specimens. Virtual specimens enable the development of high fidelity finite element models which can be used to probe the properties and response of 3D woven CMCs. The procedure involves: (i) characterizing the stochastic variations of the amplitudes and phases of the Fourier components in Figure 4.15; (ii) using a Monte Carlo method to generate other instantiations of the set of Fourier components from the same statistical distribution; and (iii) reconstructing the virtual specimen by inverse DFT. Details of the procedure are given in the Appendix.

Figure 4.16 illustrates an example of the tow density variations generated by the reconstruction algorithm for one virtual specimen, i.e., for one choice of pseudo-random numbers. The spatial variations are qualitatively very similar to those seen in the experimental data (Figure 4.14). Complete validation of the quality of the reconstruction algorithm requires comparison of data from a large ensemble of virtual specimens with data from a large ensemble of real specimens.

4.3.8 Discussion

Deviations in the tow positions may have arisen during handling of the woven fabric (after manufacturing). Alternatively they may have been built into the fabric during the textile manufacturing process. The analysis suggests that the deviations in fact include contributions of both type: namely, long-wavelength contributions caused by fabric deformation and short-wavelength contributions created during the weaving process.

Deviations in the lateral positions of weft tows can arise during ”beating up”, wherein weft tows that have been newly inserted between warp tows are pushed along the warp tows into the fabric that has already been formed. The position at which the weft stops sliding along the warp tows during beating up is expected to be variable (Figure 4.10(b)). Deviations in the lateral positions of warp tows might arise during weaving due to interplay between looseness in the heddles that guide the warp tows, variations in the frictional drag imposed by weft tows during their insertion, and non-uniformity in the tensions applied to the warp tows. Variations in the lateral positions of either tow type imply variations in the local packing density of tows, which imply variations in the local fiber volume fraction.

Displacements due to deformation of the fabric after its manufacture are associated with global shear deformation, which occur by sliding rotations of tows at crossovers. When the global shear is small, it causes minimal change to the local tow packing density. The tow spacing varies as shear strain γ^2; for $\gamma \sim 10^{-2}$, for example, the fractional change in tow spacing is $\sim 10^{-4}$. However, if the shear strain is large (say ~ 0.1), changes in tow spacing can be so severe that fabric ”lock-up” occurs. When shear causes changes in tow spacing, the changes will be uniform over spatial gauge lengths for which the shear strain is uniform.

By sampling specimens much larger than the unit cell size, the DIC method has revealed statistical information that could not be discerned in a previous study in which the same composite had been characterized by micro-computed tomography (μCT) of small test specimens (volumes comparable to a single unit cell) (Bale et al., 2012). In particular, the in-plane deviations in the μCT data were found not to be correlated between different tows (Bale et al., 2012), whereas the DIC data reveal that they are indeed correlated over wavelengths larger than the unit cell. These deductions are not contradictory in that longer wavelength correlations between different tows would not be expected to emerge from data samples of a single unit cell. In such small volumes, the deviations discerned in Figure 4.12 would be approximately the same for all tows and would therefore not be detected as deviations; instead, they would imply a shift in the spatial origin. Thus the μCT and DIC analyses are complementary: the μCT analysis yielding details of deviations of tow loci and shapes at scales equal to or less than the unit cell size and the DIC analysis yielding deviations with wavelength exceeding the unit cell size. A reasonable assumption is that the statistical trends at different gauge lengths found by the μCT and DIC analyses are statistically independent of each other. In generating virtual specimens, the deviations required to represent short- and long-wavelength variations in the textile would be generated separately and combined by superposition.

Along with the averaged surface height reported in Figure 4.9, the displacement, spatial derivatives, and short range deviations were also calculated for the back side of the panel and can be found in Figure 4.17. The pattern of short-range deviations on the front and the back of the panel were found to be very similar. This suggests a high degree of correlation in the motion of tows on both sides of the panel during the weaving process. Additionally, the high degree of correlation between the front and back faces of the panel, which were created from independent sets of DIC images, suggest that error in the DIC measurements and stitching procedures are small in comparison to the intrinsic deviations in the weave. While the error has not been directly quantified through replicate analysis of the panel, this conclusion is further supported by more recent work on different panels of the same weave, characterized using analogous procedures, which show the same intrinsic variations in tow packing densities.

The magnitudes and qualitative characteristics of the tow positional variations (or packing density variations) determined for the 3D woven carbon/SiC composite studied here are remarkably similar to those determined in a contemporary study of a carbon fiber 2D twill weave intended for consolidation with a polymer matrix (Vanaerschot et al., 2014). Long-range deviations found for the twill weave are similar, exhibiting a wavelength comparable to the specimen dimension, again suggesting shear deformation resulting from handling of the manufactured fabric. Short-range deviations are also similar, comprising multiple wavelengths between the unit cell size and the specimen size, and exhibiting similar anisotropy in the variation of deviations in directions parallel and normal to the tow direction. The similarity of short-range deviations suggests that the observed variance results from variance in loom actions that may be characteristic of weaving machinery, i.e., qualitatively consistent for different looms.

4.4 Application and extensions to other panels

4.4.1 Material system and weave characterization

Material structure and fabrication

The preceding characterization methods were extended to panels containing weave features and defects. These features and defects were created by modifying the original weave architecture in four ways.

First, the warp wavelength prescribed during weaving was increased by

$\sim$ 50 %. The result is a reduction in the weft packing density. This, in turn, leads to a reduced composite stiffness in the weft direction (Shaw, 2014).

Second, holes were created within the fabric preform *prior to* CVI processing. This was accomplished by gently inserting graphite rods, with smoothly pointed ends and diameter 2 mm, through the fabric preform at select locations. During this operation the tows surrounding the rod were displaced laterally by a small amount with minimal fiber damage. The rods were removed after the pyrolytic carbon coating step, leaving behind approximately circular holes within the partially processed preform (Figure 4.19(a)). The resulting holes were 1.6–2.0 mm in diameter.

Third, a globally sheared preform was created by taking a pristine fabric preform and clamping it along the two edges parallel to the weft tows. While fixing one edge, the opposite edge was displaced parallel to the weft tows until ″lock-up″: the point at which further motion was resisted by contact between neighboring tows. Graphite rods were inserted through the sheared fiber preform to secure its shape during CVI processing (Figure 4.20(a)).

Fourth, a local shear band two to three unit cells wide was created using the same method described above. Here, the preform was clamped at the edges of the shear band. The preform was again sheared until ″lock-up″. Graphite rods were inserted at the edges of the shear-band to secure the preform during

CVI processing (Figure 4.20(e)).

Characterization of weave structure

The modified panels were characterized using the approach outlined in Section 4.3. A modification was made to enable further matrix processing of the the modified panels. To prevent contamination by the paint used to create the speckles needed for DIC, an alternative approach was developed to identify the locations of the warp crowns. The locations of the warp crowns were instead identified using high resolution (1200 dpi) scanned optical images of the partially-processed panels and a computational feature-finding algorithm.

The warp crowns were identified in the following way. First, a set of n representative images of warp crowns were selected randomly from the entire image. Next, using a template matching algorithm, potential matches for each of the n images (or templates) with features on the image were identified. For each successful match, the template location (once aligned with the features) was used as an estimate of the warp crown location. Positive matches were grouped spatially and the average position of each group was computed. Additionally, the match probability (i.e. the fractional number of templates that had been matched to each warp crown) was also computed. Features with a match probability of $< 10\,\%$ were deemed to be false positives and were therefore excluded from further analysis. Following this procedure, about 99 % of warp crowns were correctly identified; the remaining crowns and their locations were identified manually. Segments of incomplete tows at the panel edges were excluded from the analysis, thereby yielding a rectangular data array.

Once identified, the warp crown were used as fiducial markers to characterize the weave using the the analytical methods presented in Section 4.3. The panel with holes and the two sheared panels were made in the same run as the as-processed (reference) panel characterized above. Therefore, the idealized unit cell parameters ($\lambda_{warp} = 7.52\,\text{mm}$ and $\lambda_{weft} = 5.05\,\text{mm}$) determined for the reference panel were used to calculated the local deviations in the panel with holes and sheared panels. For the panel with the elongated unit cell, the unit cell parameters ($\lambda_{warp} = 11.08\,\text{mm}$ and $\lambda_{weft} = 5.09\,\text{mm}$) were calculated using the methods that had been applied to the reference panel.

4.4.2 Weave features and defects

Maps of the spatial derivatives for the modified panels are shown in Figures 4.18(b-d), 4.19(b-d), and 4.20(b-d, f-h). For comparison, results for the reference panel have been reproduced in Figure 4.18 (f-h). The maps of spatial derivatives were re-scaled for comparison with the modified panels. Measurements of the average values and standard deviations of the spatial derivatives for the five panels — reference, with an elongated unit cell, with holes, globally sheared, and locally sheared — are summarized in Figure 4.21.

Elongated unit cell

In the panel with the elongated unit cell, the variation in δ_{xy} is predominantly long-range in nature, with a gradient in δ_{xy} from the top left to bottom right corners of the panel (Figure 4.18(b)). The non-zero values of δ_{xy} are attributable to shear of the panel during handling after weaving. The magnitude of its average value ($\delta_{xy} = 0.005$) is comparable to that in the reference panel ($\delta_{xy} = 0.003$), but its standard deviation is about three times that in the reference panel (± 0.025 versus ± 0.008) (Figure 4.21). The presence of uniform gradients in δ_{xy} across both panels (Figure 4.18(b,f)) indicates that the variation in δ_{xy} is a function of the panel size. The elongated unit cell panel is 182 mm × 287 mm in size, nearly three times larger than the reference panel (157 mm × 116 mm in size). This is consistent with the difference in the standard deviation in δ_{xy} between the two panels. Of final note is the change in sign of δ_{xy} between the two panels. This indicates that the three-layer angle-interlock weave is susceptible to shear in both directions. This is also observed in the sheared panels.

The spatial variations in δ_{xx} and δ_{yy} are characterized predominantly by periodic *short-range* fluctuations over length scales of a few multiples of the unit cell dimensions. These fluctuations are manifested in the form of bands of either dilation (positive δ) or compaction (negative δ). In the panel with the elongated unit cell the variations in δ_{xx} are greater than in δ_{yy} (Figures 4.18(c-d)). This is in contrast to the reference panel, where the variations in δ_{xx} and δ_{yy} are comparable (Figures 4.18(g-h)). The average values of δ_{xx} and δ_{yy} are nominally zero in both panels (Figure 4.21), indicating that the variations are intrinsic to the weaving process.

These results suggest that the increased variance in δ_{xx} is due to the elongation of the warp wavelength. Increasing the warp wavelength leads increases the average spacing between weft tows. Variation in the weft packing density is caused by variation in tow motion during "beating up" after the insertion of each weft tow. The extra space between the weft tows allows for greater variability during consolidation. The weave parameters defining the warp spacing were unchanged between the reference and elongated unit cell panels, resulting in similar variations in the warp packing density (δ_{yy}).

Panel with holes

A nearly-uniform gradient in δ_{xy} is evident from the top left to the bottom right in the panel with holes (Figure 4.19(b)). The magnitude of its average value and standard deviation ($\delta_{xy} = 0.014 \pm 0.016$) are only slightly larger than the average value for the reference panel ($\delta_{xy} = 0.003 \pm 0.008$) (Figure 4.21). It is evident from Figure 4.19(b) that local deformation of the preform due to the presence of the holes does not contribute significantly to the mean and standard deviation of δ_{xy}. The disturbance to the δ_{xy} field due to the holes is small in magnitude and localized to a very small area surrounding each hole. The increased average δ_{xy} is attributable to the additional handling required to create the holes.

The variations in δ_{xx} and δ_{yy} are characterized predominantly by bands of dilation and compaction of the tows. These variations are intrinsic to the weaving process. Additionally, very near the holes, δ_{yy} (~ 0.05) is about an order-of-magnitude greater than average; the effect persists over an apparent distance of about one unit cell away from the holes (see inset in Figure 4.19(d)). (Since the strains are computed over distances equal to the unit cell dimensions, the apparent strain within an individual cell can be the result of a large displacement of *a single warp crown* adjacent to the hole. Indeed, this appears to be the case for many of the holes in Figure 4.19(a).) In contrast, the local values of δ_{xy} and δ_{xx} are elevated only very slightly relative to their respective averages (insets in Figures 4.19(b) and (c)).

The local deviation of the warp packing density (δ_{yy}) adjacent to the holes is significantly greater than that of the weft packing density (δ_{xx}) suggesting greater positional correlation between neighboring warp tows than neighboring weft tows. This is due to the topology of the weave. The warp weavers lie on the relatively straight weft tows allowing for lateral sliding, resisted mainly by compression of the neighboring warp tows. The weft tows, on the other hand, are constrained laterally by the interlocking warp weavers at the crossovers, but are unconstrained between these points. Lateral motion of the weft tows must be transmitted to its neighboring wefts through the interlocking warp network over length-scales longer than a unit cell. Within a unit cell, each weft tow is not in direct contact with its neighboring weft tows. Instead, a sizable gap (ca. 1 mm) exists between adjacent weft tows, as evident, for example, in Figure 4.1(a). Consequently, large lateral displacements would be required in any one weft tow in order to cause displacement of neighboring weft tows.

Sheared panels

In the globally sheared panel, δ_{xy} is characterized by three regions of approximately uniform shear (Figure 4.20(b)). Each region is of comparable width. The left and right most region are more heavily sheared, with average values of $\delta_{xy} \approx 0.045$. In the central region the average value is $\delta_{xy} = 0.03$. The consistency in length over which approximately uniform shear is observed suggests that the cooperative motion of the weave in the warp direction is limited to the width of one of these regions (75–85 mm or 10–11 unit cells). This distance is commonly referred to as a correlation length (Bale et al., 2012). In the locally sheared panel, a central band approximately three unit cells wide was sheared uniformly. The magnitude of δ_{xy} in this region is ~ 0.09. For comparison, measurements on the reference panel yield an average value of $\delta_{xy} = 0.003$: more than an order-of-magnitude smaller than in either of the sheared panels.

In both the globally and locally sheared panels, δ_{xx} is characterized by two main features. First, intrinsic variations in the weft packing density are evident as bands of positive and negative δ_{xx} (Figures 4.20(c) and (g)). The magnitude of these variations are comparable to the variations in the reference panel (Figure 4.18 (g)). Second, a localized band of dilation ($\delta_{xx} \approx 0.1$) is evident adjacent to the heavily sheared portions of each panel (Figures 4.20(c) and (g)).

In the globally sheared panel the band appears at the boundary between the heavily sheared region on the right side of the panel and the lightly sheared region in the center. In the locally sheared panel the band occurs at the left edge of the shear band. The magnitude of δ_{xx} in the dilation bands is more than two orders-of-magnitude greater than the average values of δ_{xx} for each panel (0.004 in the globally sheared panel and 0.0008 in the locally sheared panel) (Figure 4.21). Also of note is the presence of a localized compaction band ($\delta_{xx} \approx -0.05$) within the shear band in the locally sheared panel (Figure 4.20(g)).

As described in Section 4.4.1, these panels were deformed by shearing the weave until ”lock-up”, at which point further rotation is resisted by contact between the tows. Lock-up appears to coincide with tow rotations of $\sim 5°$. It is surmised that after lock-up, further deformation of the panels is accommodated by extension and compaction of the weave. In both panels *extension* along the warp direction occurs in the dilation bands adjacent to the heavily sheared regions of the panels. This extension is accommodated by the waviness of the warp weavers and the gaps present between the weft tows. The location of the dilation bands adjacent to the heavily sheared regions of the weave suggests that extension of the weave is resisted within in these heavily sheared regions, i.e., in the locked-up regions weave extension and further tow rotation are resisted by tow contact. In the locally sheared panel *contrac-*

tion along the warp direction occurs within the shear band, where the tow rotations are $\sim 10^\circ$, twice that in the globally sheared panel. This suggests that weave contraction enables continued tow rotation beyond 5°.

In contrast to δ_{xx}, the variations in δ_{yy} are unaffected by the shear defects. In both the globally and locally sheared panels, the variations in δ_{yy} (Figures 4.20(d) and (h)) are comparable to the variation in the reference panel (Figure 4.18(h)). The average values of δ_{yy} within the globally and locally sheared panels (0.0044 and 0.0046, respectively) are slightly higher than the average value for the reference panel (0.0002), but comparable to the average value for the panel with holes (0.0037). Dowels were inserted through the sheared panels to retain their shape during CVI processing. This same was used to create the woven holes. As described above, δ_{yy} is elevated by up to an order-of-magnitude adjacent to the woven holes. These elevations are evident in Figures 4.20(d) and (h) and likely elevate the average values of δ_{yy}. The absence of localized dilation or compaction bands in δ_{yy} is consistent with the weave topology. The weft tows are nominally straight and not easily extended during handling and the warp tows are constrained from lateral motion by their neighboring warp tows.

4.4.3 Discussion

The panels characterized in this chapter were further processed (using PIP) to densify the matrices. Shaw et al. (2014b) and Shaw (2014) investigated the effect of these weave features and defects on the mechanical performance of the densified composites.

It was found that increasing the warp wavelength reduced the composite stiffness and ultimate tensile strength when tested in the weft direction. This is consistent with a reduction in the fiber volume fraction (weft packing density). When tested in the warp orientation the stiffness was unchanged, but the ultimate tensile strength was increased. The increase in strength is attributed to decreased waviness of the warp tows with increasing wavelength.

The introduction of holes through the weave caused negligible distortion of the surrounding weft tows and only localized changes in warp tow packing density. The ultimate tensile strength of the composite exhibited only weak sensitivity to the presence of the woven holes. The response of samples with woven holes was found to be comparable to composites with holes of the same size produced by drilling.

Test coupons from the globally sheared panel were prepared in three orientations: parallel to the warp tows; parallel to the weft tows; and perpendicular to the warp tows. For loadings parallel to one of the two principal tow directions, the composite response was found to be insensitive to shear defects. For loadings perpendicular to the warp tow population, the misalignment of the axial tows leads to accelerated strain softening and a reduced failure stress. These effects are attributable to a reduction in the number of intact tows within the gauge length and progressive decoupling and unloading of the non-continuous tows near the edge of the test coupons.

4.5 Conclusions

A methodology for determining in-plane weave characteristics and departures from an ideal periodic weave structure in textile ceramic composites has been developed. The methodology involves:

1) Determination of surface topography using high resolution image pairs and 3D image correlation;

2) Identification and segmentation of the positions of a prescribed population of surface tows for use as fiducial markers;

3) Determination of a hypothetical perfectly periodic pattern that best fits the stochastic positional data for tows;

4) Determination of in-plane deviations in the nodal positions from their positions in the hypothetical ideal and partitioning of these deviations into short- and long-range components;

5) Determination of spatial derivatives of deviations; and

6) Spectral analysis of the spatial derivatives in the direction transverse to either set of tows by DFT, combined with simple models of the rate at which the complex amplitude of each Fourier component varies in the direction parallel to that set of tows.

Short-range deviations in the tow positions are associated with intrinsic variability in the weaving process and leads to variations in the local packing density of the tows. Long-range deviations are attributed to fabric deformation during handling and are usually associated with global shear deformations of the fabric preform.

The magnitude of these variations are expected to have minimal effect on the ultimate tensile strength and failure strain of C-SiC composites fabricated from preforms of this type. However, small variations in tow packing density might be expected to affect infiltration and densification of the matrix material within the inter-tow spaces. The resulting variation in the matrix density and pore distribution may bias the locations and loads for crack initiation and hence compromise the resistance of the composite to environmental attack.

The measurement and analysis methods have been extended to characterize weave features and defects that have a larger impact on composite properties. Therefore, the test methodologies could be readily adopted as part of quality assurance protocols that could be carried out at various stages of composite fabrication.

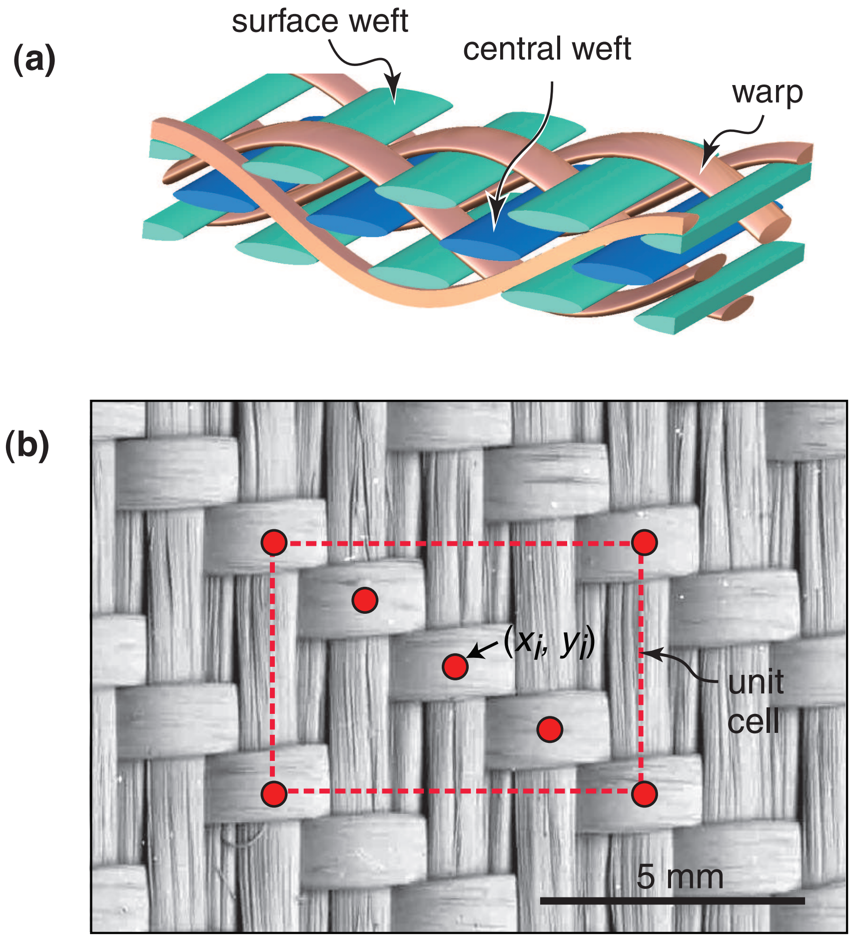

Figure 4.1: Unit cell of three-layer angle interlock weave of present interest: (a) schematic showing the three genuses of tows and (b) optical image of the composite in plan view. Also shown in (b) is a set of grid points used for least-squares fitting of the deviations (u_j, v_j) at point (x_i, y_i), as described in Section 4.3.5.

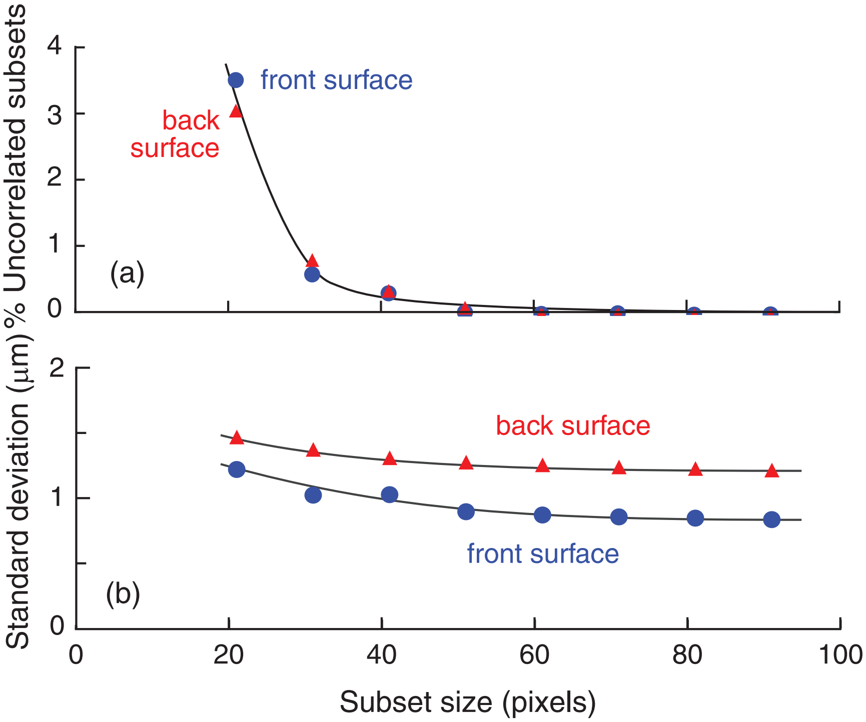

Figure 4.2: Effects of subset size on (a) percentage of uncorrelated subsets and (b) standard deviation in surface heights from sequential images.

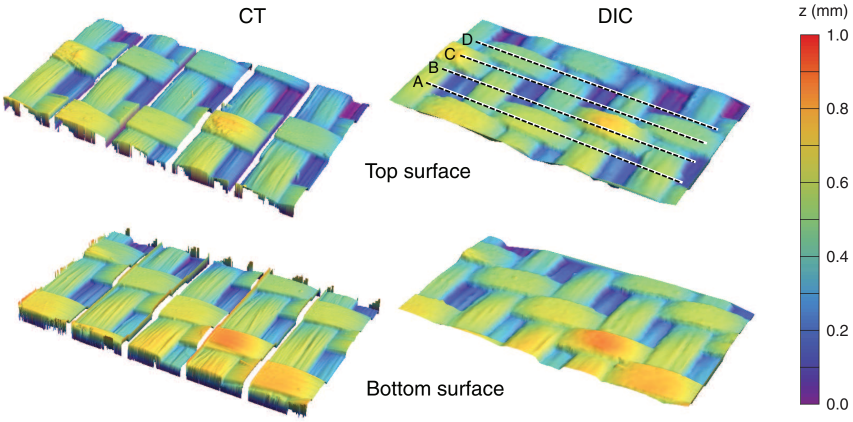

Figure 4.3: Comparisons of 3D renderings of surfaces obtained from both CT and DIC. Specimen length (from left to right) is 13 mm. Lines labelled **A-D** are trajectories of scans presented in Figure 4.4. (Narrow gaps between the five tiled scans in the CT images on the left represent regions in which CT data had not been collected.)

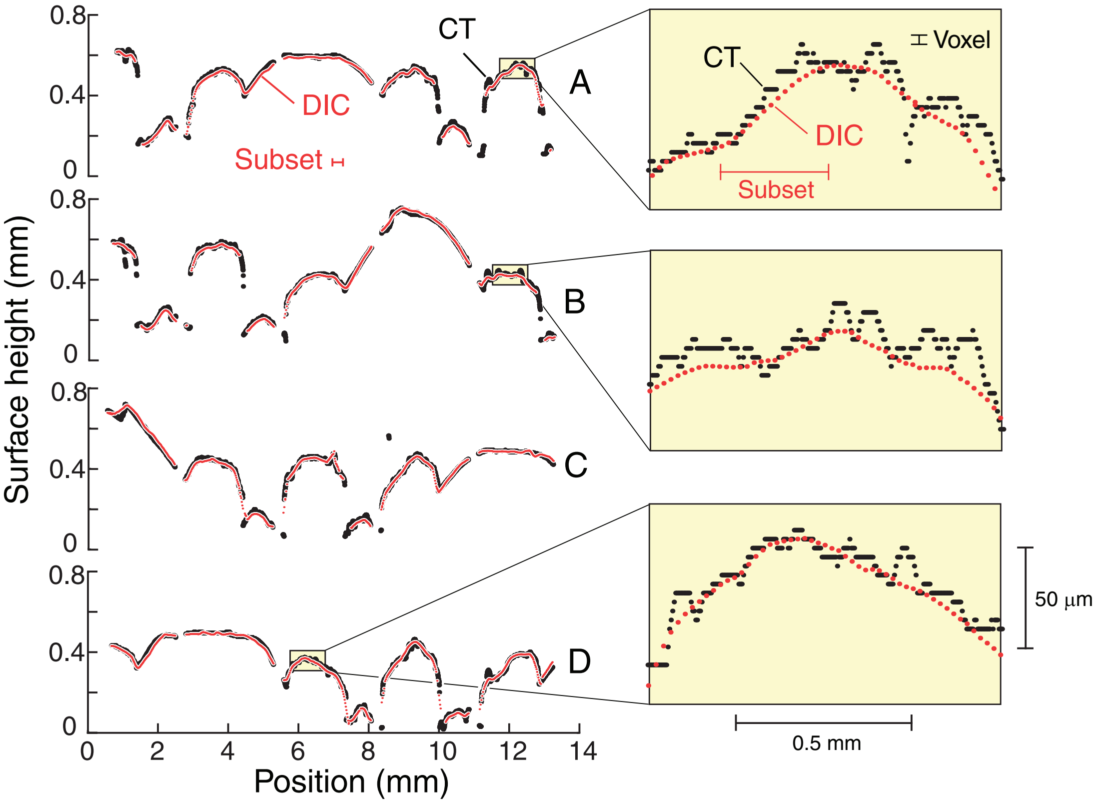

Figure 4.4: Representative line scans of surface heights obtained from DIC and CT. Locations of scans AD are indicated on Figure 4.3. Expanded regions on the right are examples where correspondence between DIC and CT is poorer than average, due to the presence of protruding filaments on the composite surface.

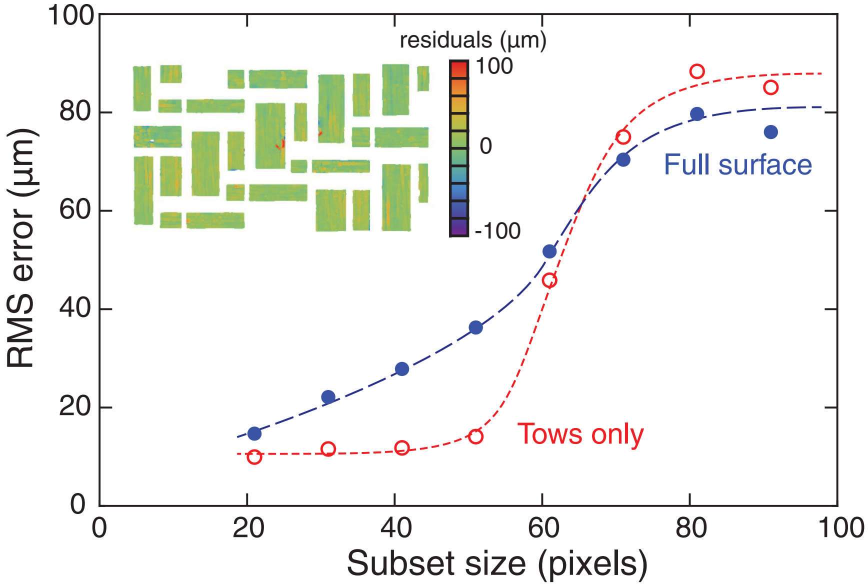

Figure 4.5: Variation in RMS error with subset size and, in inset, map of residuals between CT and DIC surfaces for regions away from the tow boundaries, all for a subset size of 31 pixels.

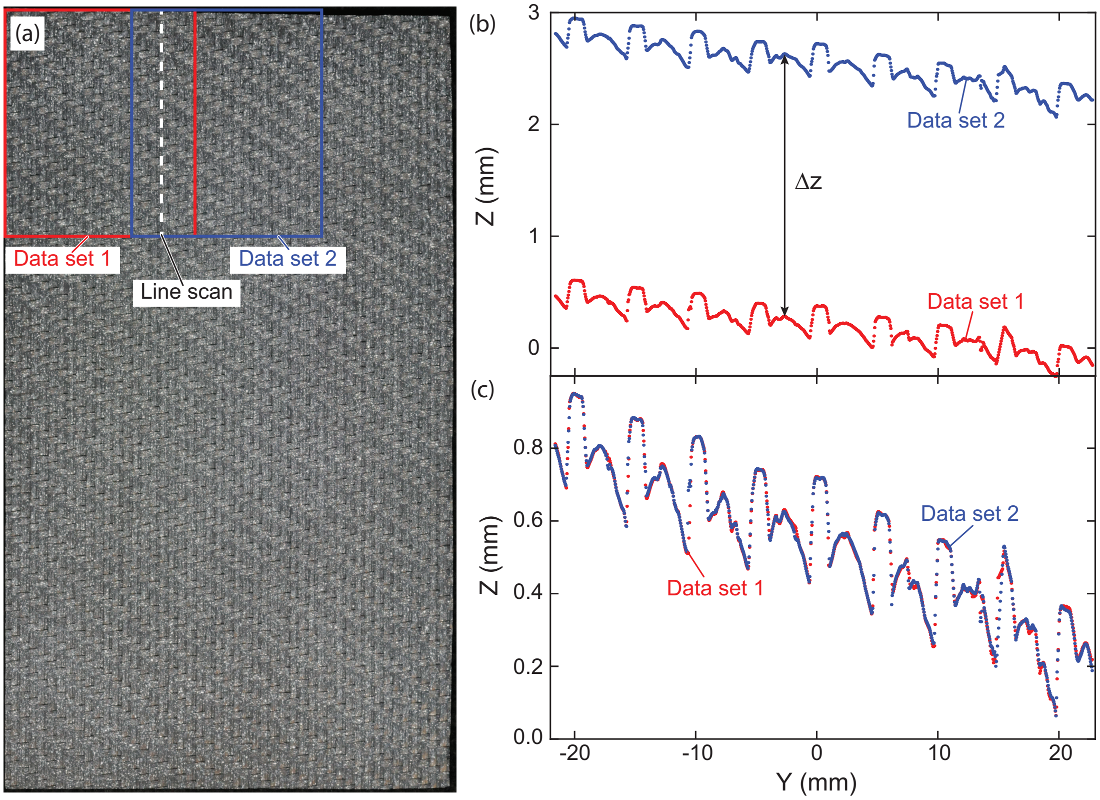

Figure 4.6: Procedure for determination of shift in z-direction: (a) line scans are taken from the center of the overlapping region between neighboring data sets; (b) the difference in mean z-position of the two line scans is computed; and (c) the data sets are shifted in z accordingly.

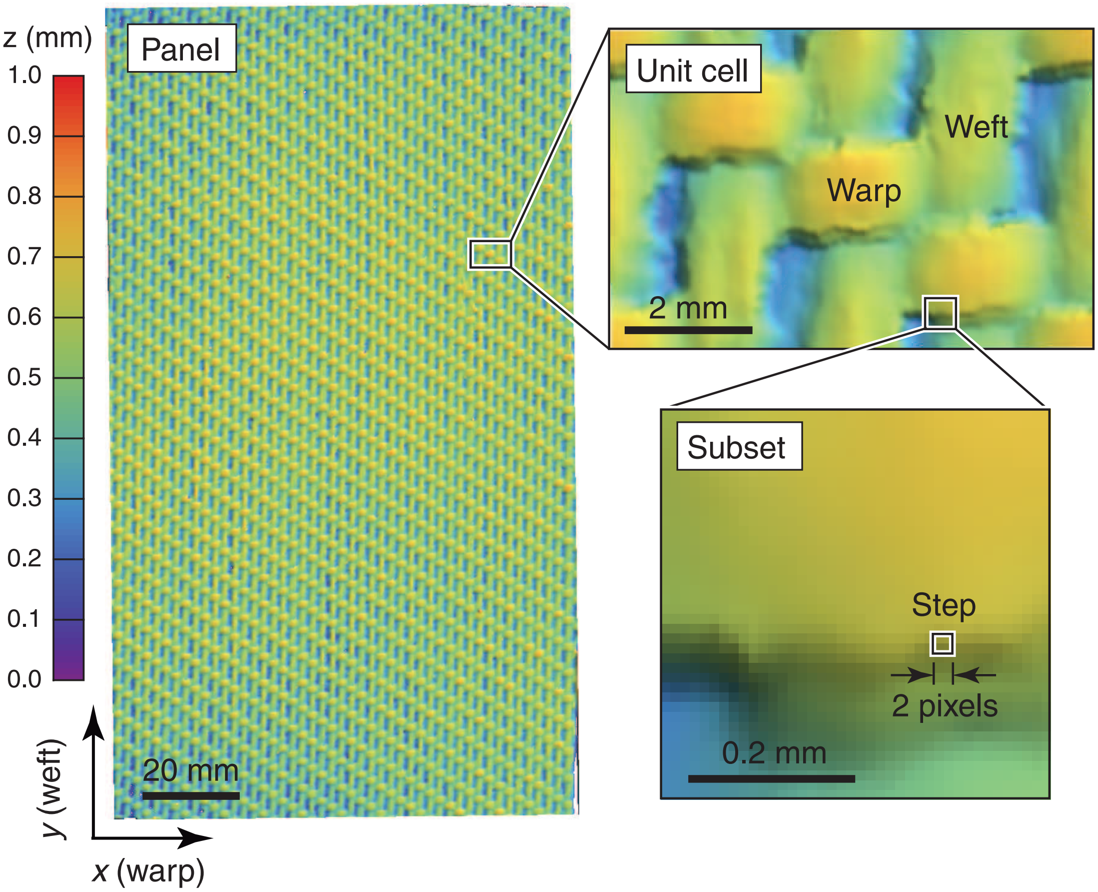

Figure 4.7: Surface topography at various length scales of one face of the composite panel. Slight gradient in height from panel edges inward in (a) is a manifestation of panel curvature.

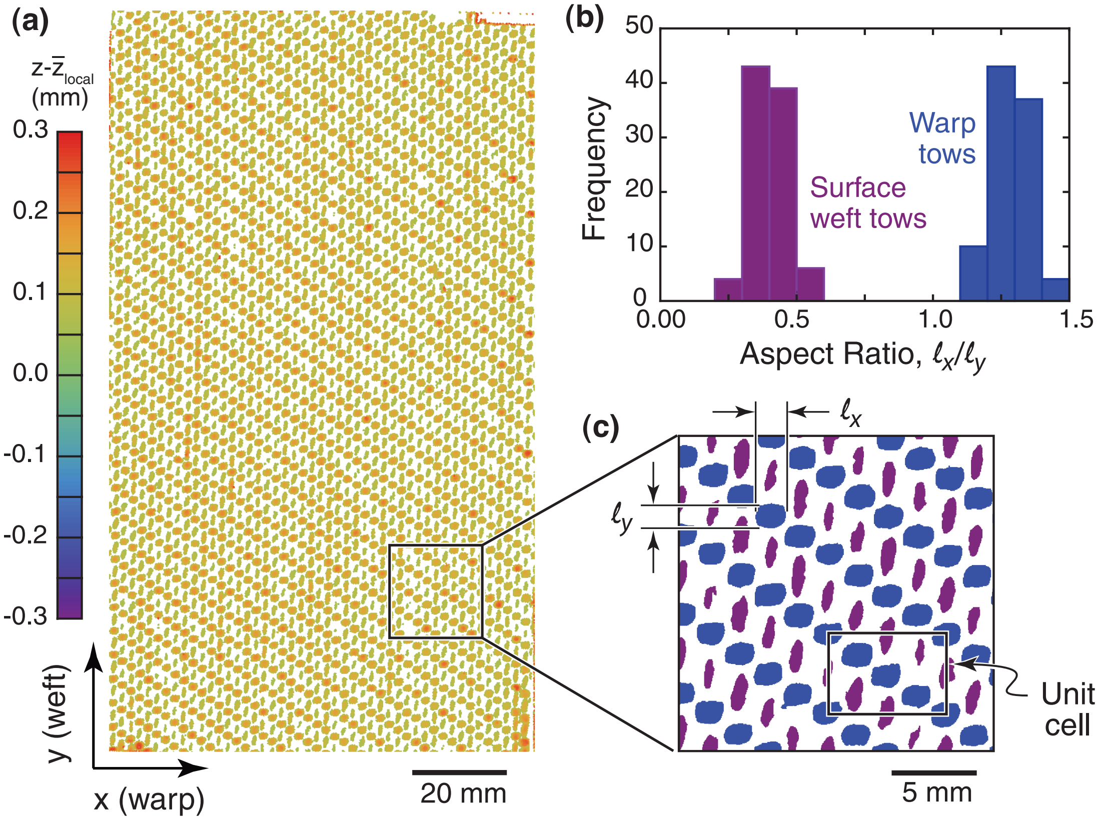

Figure 4.8: Results of segmentation process used to isolate tow segments. (a) Thresholding based on local surface heights, (b) subsequent differentiation between wefts and warps based on tow aspect ratios, and (c) resulting surface weft and warp tow segments (shown in purple and blue, respectively).

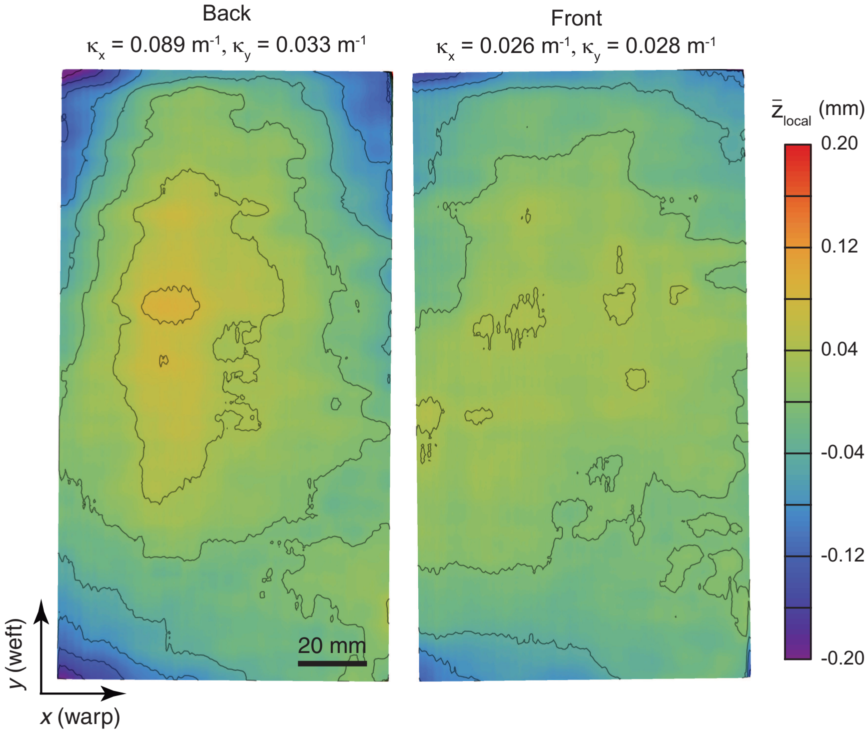

Figure 4.9: Distribution in surface heights averaged locally over one unit cell. The distributions were fit to second-order polynomials in both x and y and the fitted function then used to compute the curvatures k_x and k_y in the x and y directions, respectively.

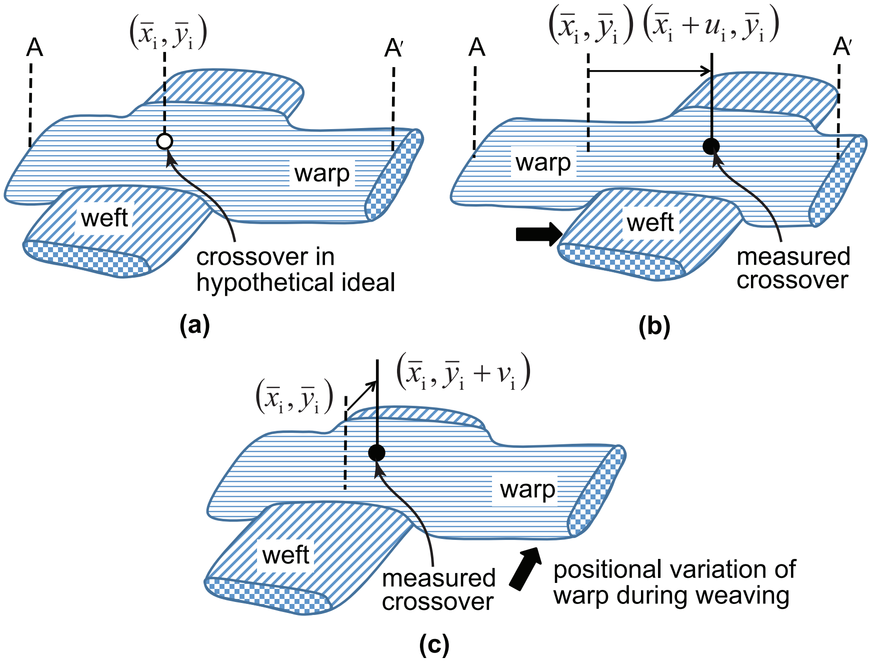

Figure 4.10: (a) and (b): A shift of the centroid of a warp crown in the warp direction indicates a lateral variation in the location of the underlying weft. (a) and (c): A shift of the centroid of a warp crown in the weft direction indicates a lateral variation in the location of the warp.

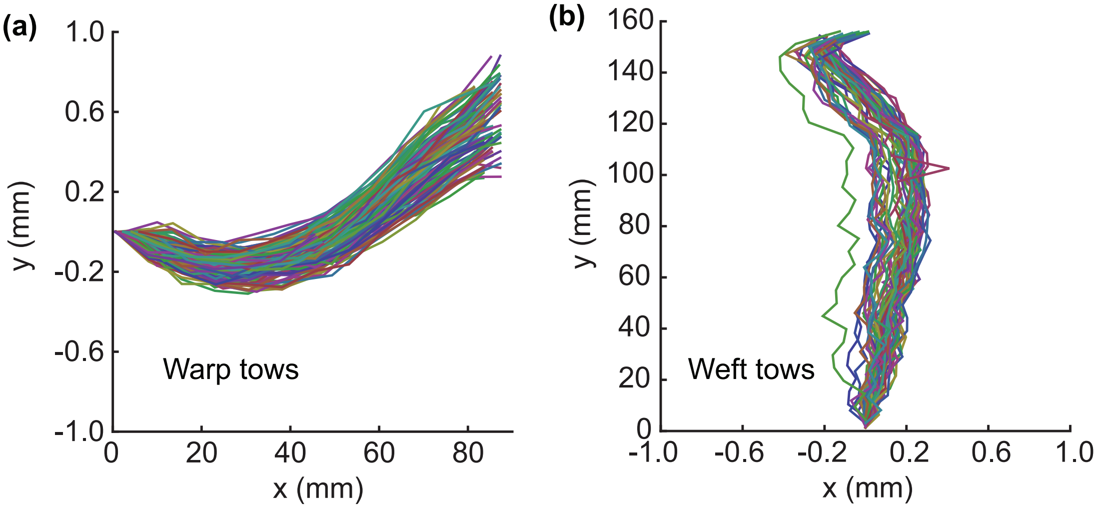

Figure 4.11: (a) Warp and (b) weft tow trajectories throughout entire panel. The warp trajectories had been shifted in the y-direction so as to align the left end of each tow with $y = 0$. Similarly, the weft tows had been shifted in the x-direction so as to align the bottom end of each weft with $x = 0$.

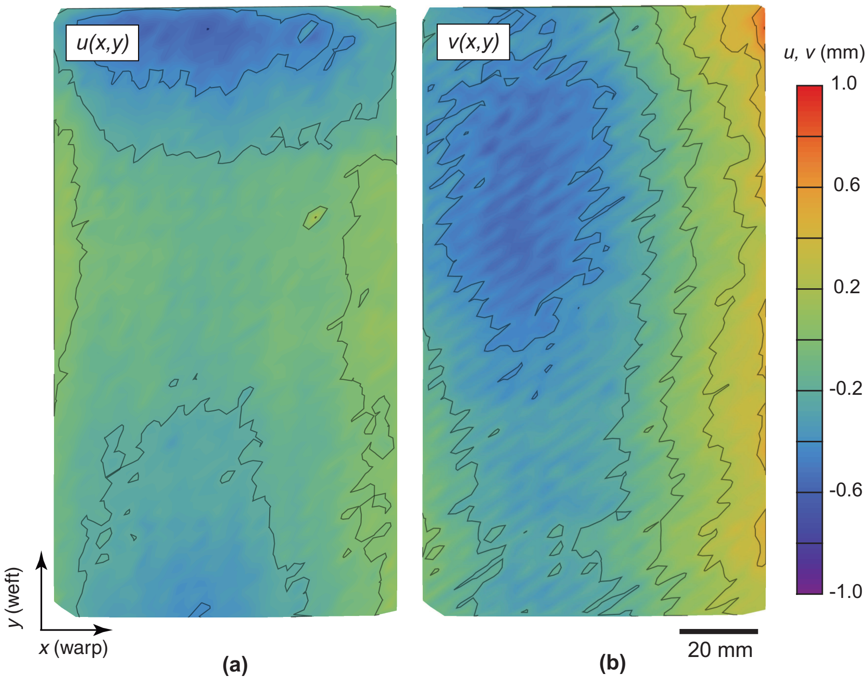

Figure 4.12: Quasi-continuous plots of the displacement components, formed by linear interpolation of the discrete data (u_i, v_i), where u and v are displacements in the warp (x) and weft (y) directions, respectively.

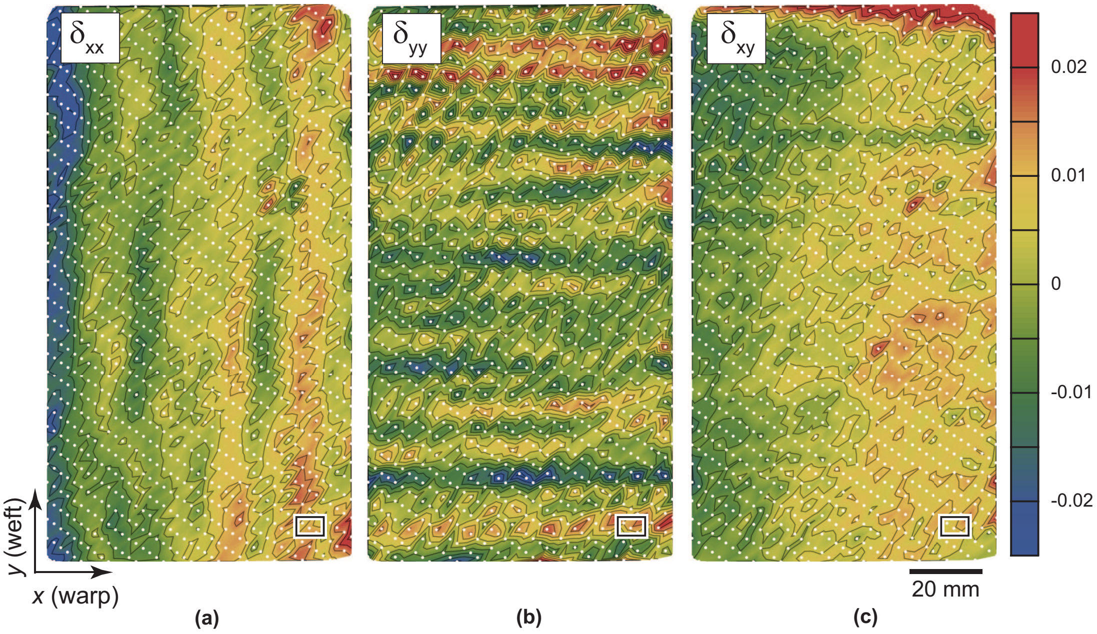

Figure 4.13: Quasi-continuous plots of spatial derivatives of the deviation data (u_i, v_i) in Figure 4.12 with overlay of warp crown positions. The rectangle in the bottom right corner of each figure represents one unit cell. (The short-range variations are not evident in Figure 4.12 because of the coarseness of the displacement scale needed to show the long-range variations.)

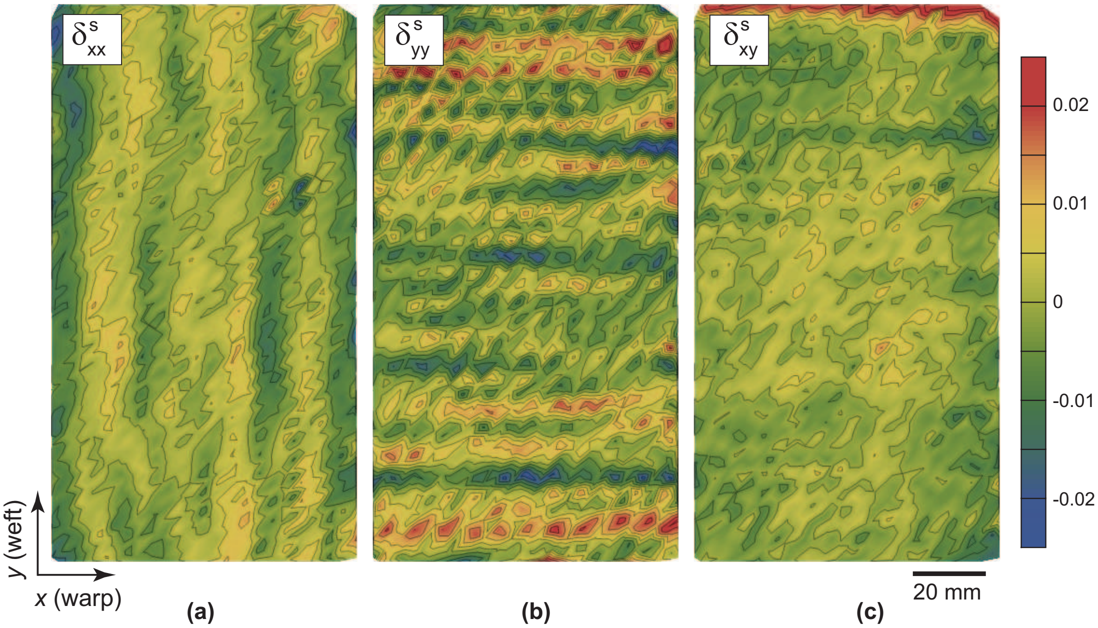

Figure 4.14: Quasi-continuous plots of short-range spatial derivatives of the deviation data $(u_i, v_i)_s$.

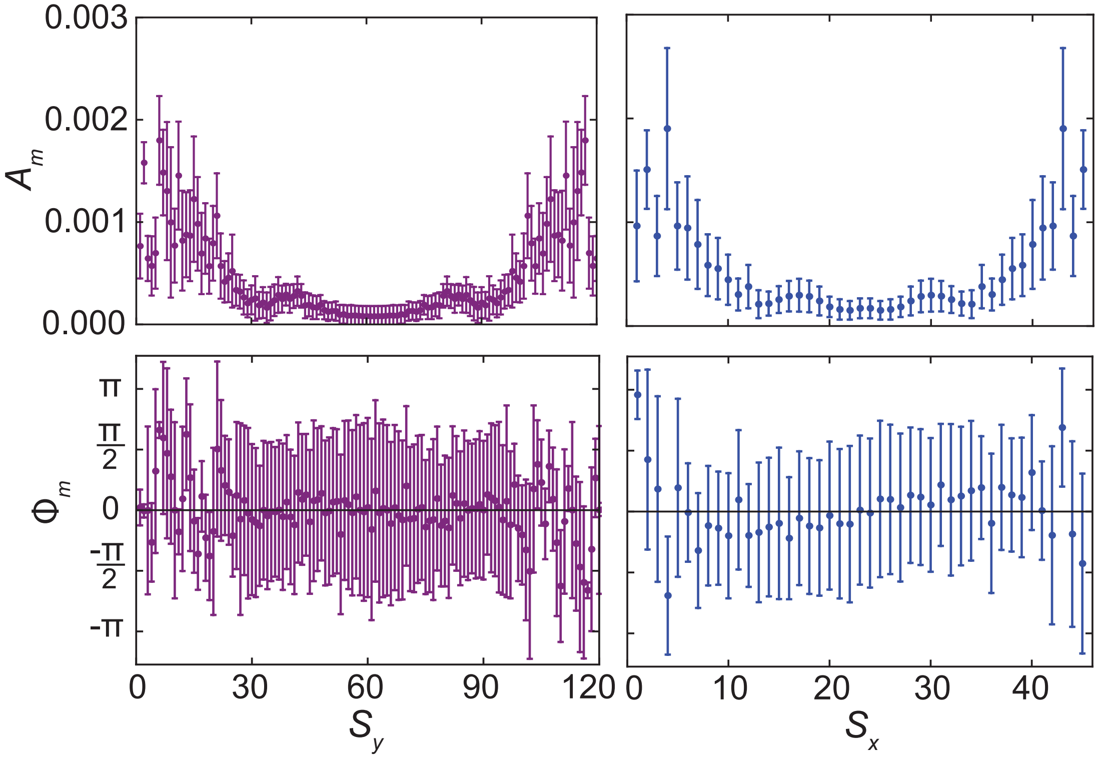

Figure 4.15: Distribution of amplitudes and phase from DFTs of all available scans.

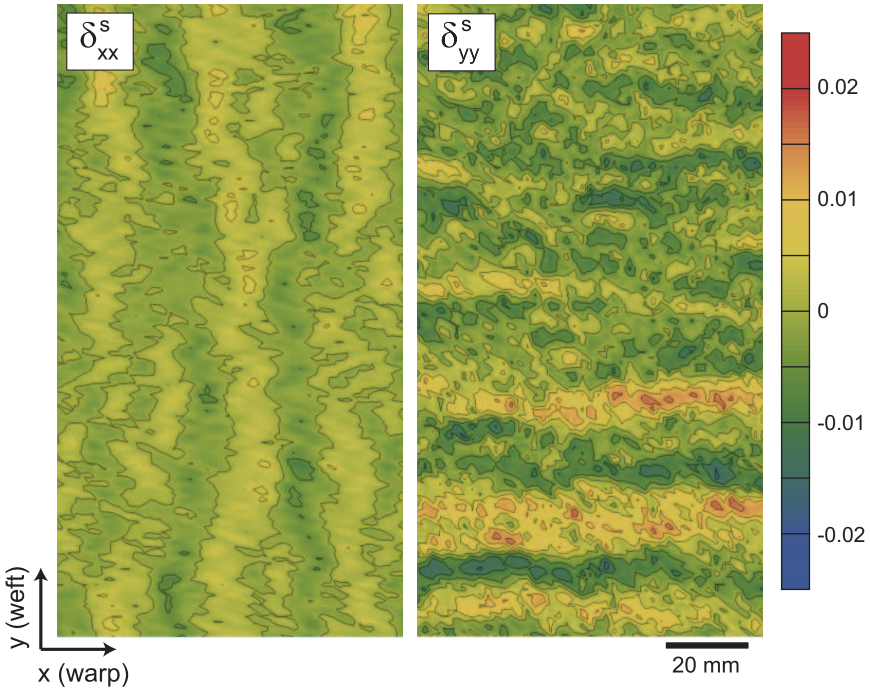

Figure 4.16: Packing density variations generated using the reconstruction algorithm.

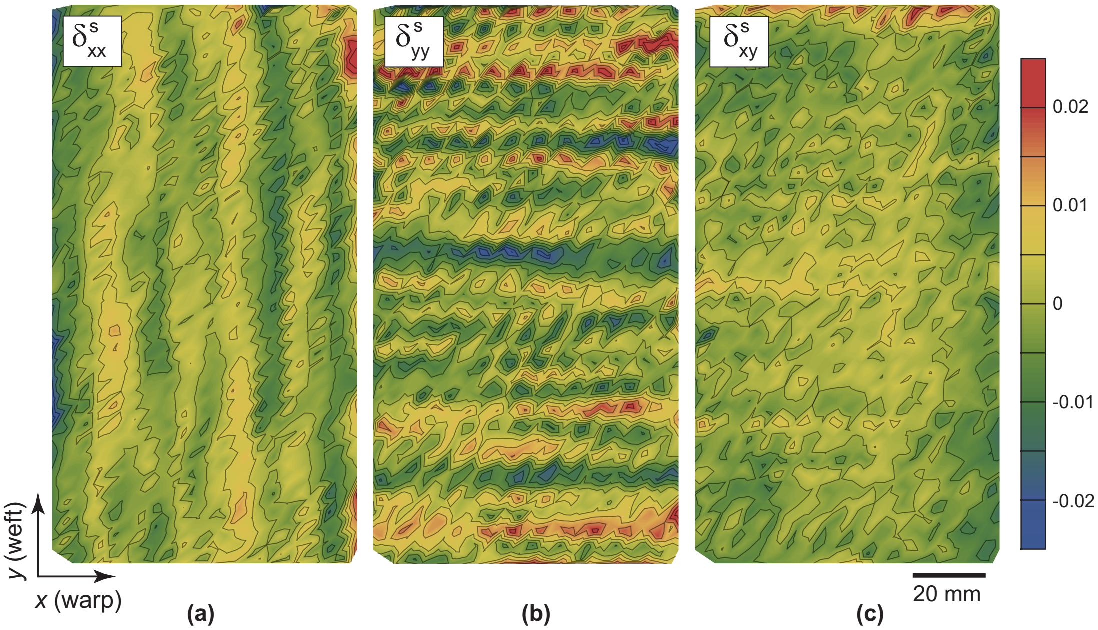

Figure 4.17: Quasi-continuous plots of short-range spatial derivatives of the deviation data $(u_i, v_i)_s$ from the back side of the panel.

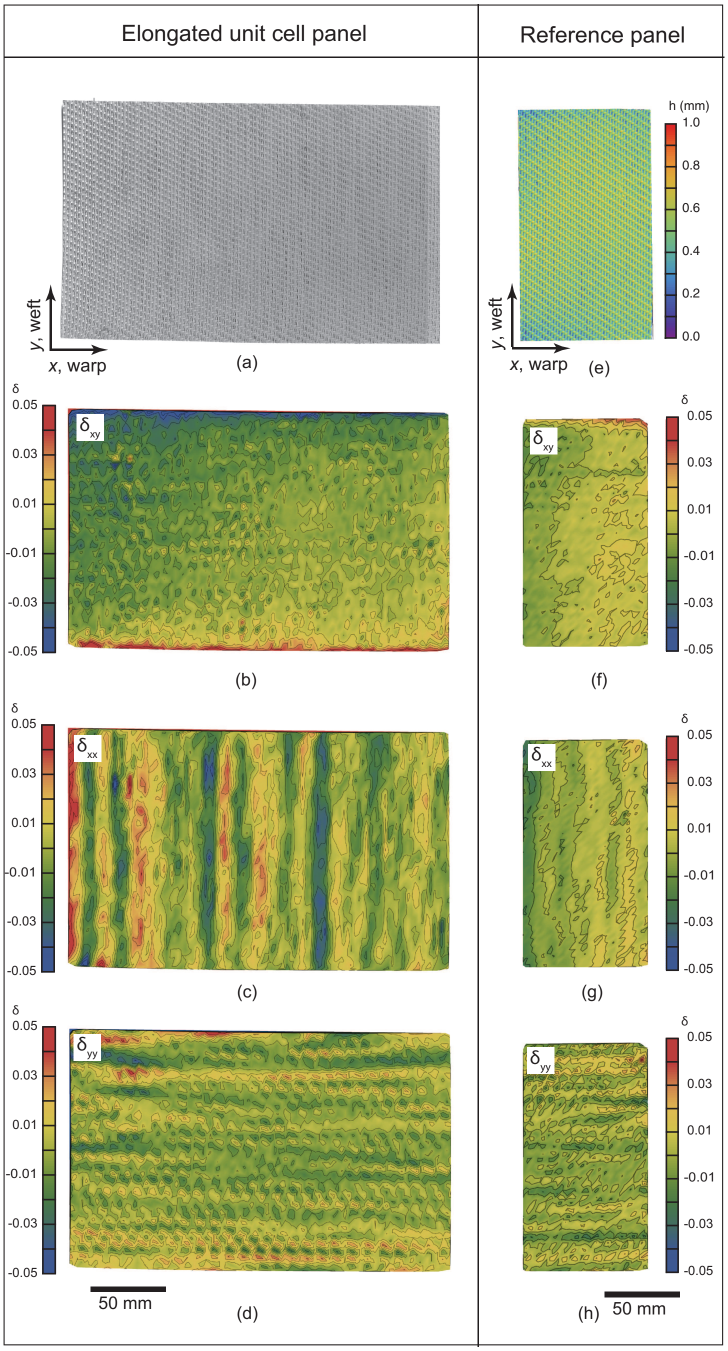

Figure 4.18: (a) Plan view of the panel with an elongated unit cell. (b-d) Spatial variations of computed δ_{xy}, δ_{xx} and δ_{yy}. (e-h) Corresponding results for the reference panel. Image in (e) was constructed using 3D digital image correlation. All figures are at approximately the same scale.

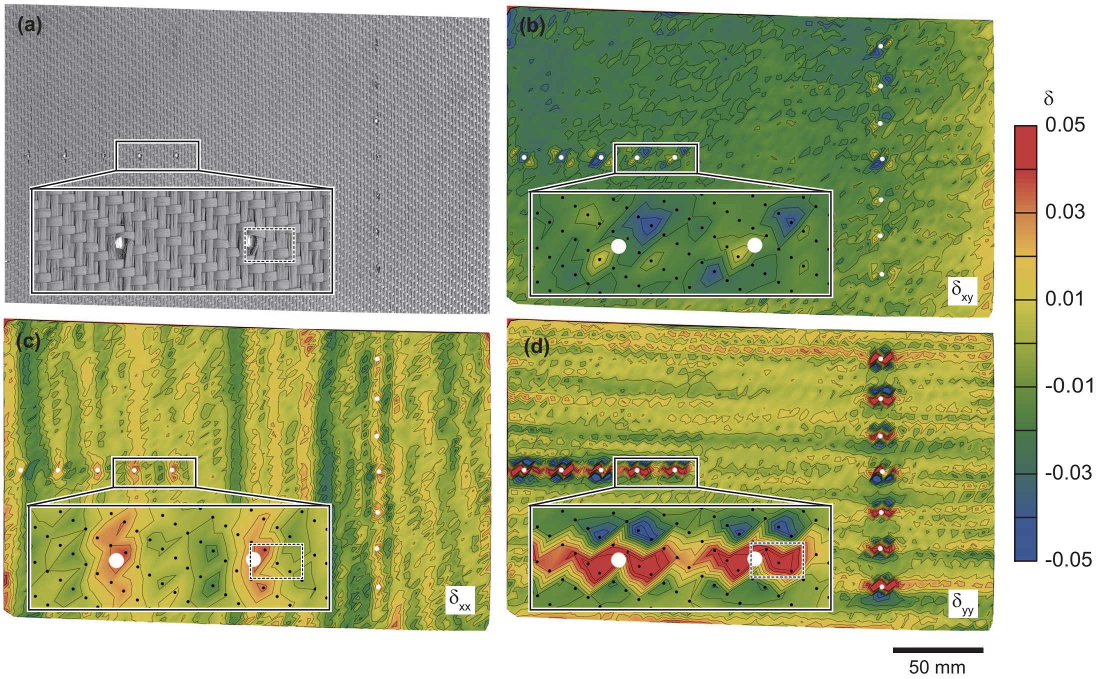

Figure 4.19: (a) Plan view of the panel with woven holes. (b,c,d) Spatial variations of computed δ_{xy}, δ_{xx} and δ_{yy}.

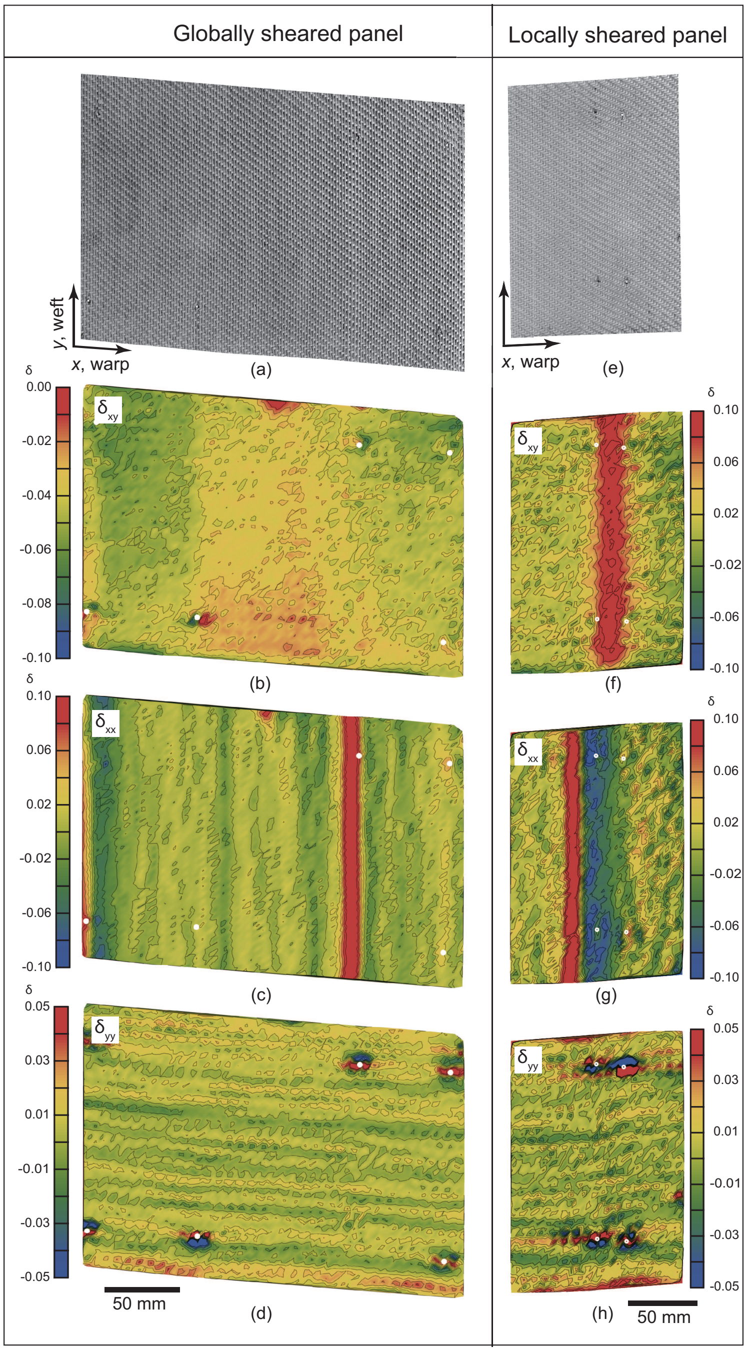

Figure 4.20: (a) Plan view of the globally sheared panel. (b-d) maps of δ_{xy}, δ_{xx} and δ_{yy}. (e-h) Corresponding results for the locally sheared panel. All figures are at approximately the same scale.

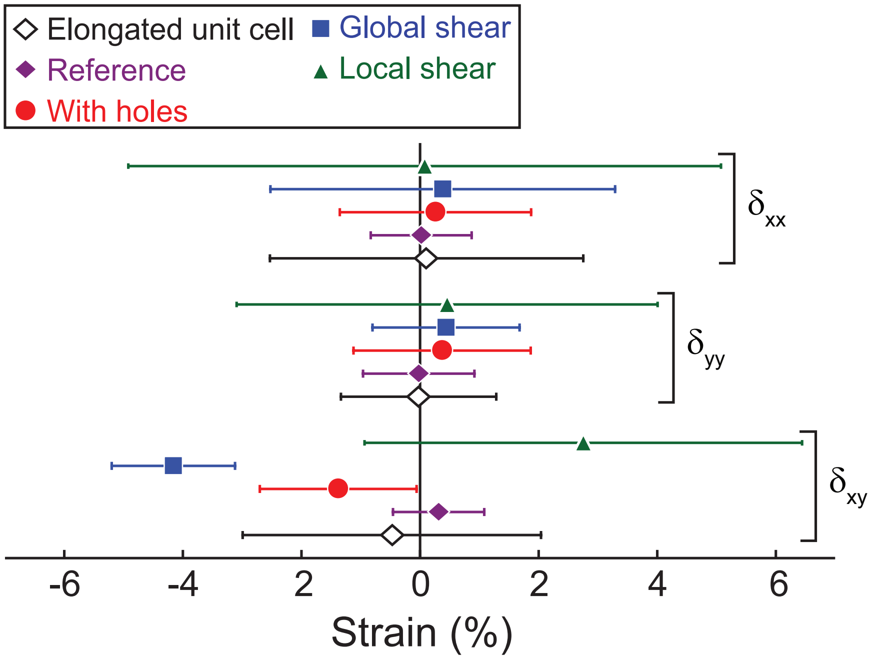

Figure 4.21: Summary of the averages and standard deviations of spatial derivatives δ_{xx}, δ_{yy} and δ_{xy} for the reference panel, elongated unit cell panel, panel with woven holes, globally sheared panel, and locally sheared panel.

Chapter 5

Intermediate temperature embrittlement of woven CMCs with polymer-derived matrices

5.1 Introduction

SiC/SiC composites are susceptible to embrittlement between 700° and 900 °C. In this regime, silica formation is sluggish, allowing for oxidant ingress through open matrix cracks or existing matrix porosity. The existing theories regarding intermediate temperature embrittlement are based on experimental studies in dry, ambient air environments, on composites with MI or CVI matrices. It has been shown that oxidation of SiC is an order-of-magnitude faster in water vapor than in dry air (Opila, 1999). Additionally, boron readily volatilizes in water vapor environments leading to recession of the BN fiber coatings (Jacobson et al., 1999a,b). With water vapor contents between 5 % to 10 % in the combustion environment (Jacobson et al., 2001), these effects are expected to have significant implications on the performance of SiC/SiC CMCs. Furthermore, residual porosity in PIP-based CMCs provides for the possibility of internal oxidation prior to the formation of matrix cracks. This is in contrast to the performance of composites with MI and CVI matrices, in which oxidant ingress only occurs at appreciable rates after matrix cracking has occurred (Heredia et al., 1995). Extending the understanding of intermediate temperature embrittlement to PIP-based CMCs in water vapor containing environments is the focus of this chapter.

In this chapter, an experimental study of intermediate temperature embrittlement in a PIP-derived SiC/SiCN CMC is presented. The effects of two oxidizing environments (dry air and water vapor) on embrittlement at 800 °C are investigated. Some intermediate temperature tests are performed under static loading, whereas others involve eight hour heat treatments followed by monotonic tensile tests to measure the retained strength. Embrittlement is assessed via detailed fractography, including measurements of the size of the fiber fracture mirrors. Microstructural evolution during intermediate temperature oxidation is investigated through detailed ceramatography. The findings are used to provide further insights into the embrittlement mechanisms and to guide future studies.

5.2 Material and experimental methods

5.2.1 Material

The composite material of interest in this study is S200H, described in Chapter 3. It comprises woven Hi-Nicalon (SiC) fibers in a PIP-derived matrix. The matrix was formed using a slurry of crystalline Si_3N_4 particles in a preceramic polymer intended to produce an amorphous SiCN phase upon pyrolysis. The polymer-derived matrix contains residual porosity and microcracks as illustrated in Figure 3.1.

5.2.2 Intermediate temperature testing

Mechanical tests were performed on hour-glass shaped tensile coupons 178 mm long. The gauge section was 44 mm long with a radius of curvature of 122 mm. The width of the coupon was 11 mm outside of and 7 mm at the center of the gauge section. The test coupons were mechanically ground to shape, exposing the internal composite microstructure to the test environment. Fiberglass tabs 25 mm long were adhered to the ends of the coupon with epoxy. The tabs facilitated load transfer within the grips.

The experimental setup is depicted schematically in Figure 5.1. The tensile coupons were loaded in a hydraulic load frame (MTS) using hydraulic wedge grips. The temperature of the grips was maintained below 50 °C. Two clam-shell IR heaters (Research Inc, Eden Prairie, MN) were attached to the test frame. The heaters contained three independently controlled pairs of IR lamps. With proper calibration, a uniform hot zone 25 mm in length was produced. The temperature in the hot zone was maintained at 800° ± 10 °C. The temperature was measured using three K-type thermocouples that spanned the hot zone.

The tensile coupons were suspended inside a quartz tube 25 mm in diameter and 75 mm in length. The tube was centered inside the IR heaters. Gas was continuously passed through the tube to achieve the desired environment. Two environments were investigated: dry air (AirGas, Radnor Township, Pennsylvania) and water vapor. The dry air contained 20–22 % O_2 and less then 7 ppm H_2O. Water vapor was produced by pumping liquid water through a stainless steel tube that passed through the hot zone (see Figure 5.1). The resulting water vapor was injected into the bottom of the quartz tube. A peristaltic pump was used to inject liquid water at 0.2 mL/min, producing

1 L/min of water vapor at the test temperature.

Two types of intermediate temperature tests were performed. The first were stress-rupture tests in the water vapor environment. Samples were tested at applied stresses of 200 and 300 MPa, 35 % and 55 % of the room temperature strength. The second were residual strength tests after eight hour heat treatments in water vapor or in dry air. Following heat treatment, the samples were tested to failure under monotonic tension. The monotonic tension tests were preformed at temperature, in the same environment as the heat treatment. The tests were performed at a rate of 65 MPa/min. The experimental setup was designed to minimize oxidation of the fracture surfaces by shutting off the heaters upon failure of the test coupons.

5.2.3 Microstructural analysis

The fracture surfaces were examined by scanning electron microscopy (SEM; XL30 Sirion FEG, FEI). Transverse cross-sections $\sim$ 3 mm below the fracture surface were prepared and polished. The cross-sections were analyzed by SEM. Lamellae suitable for transmission electron microscopy (TEM; Technia G2 Sphera, FEI, Hillsboro, OR) analysis were extracted from select specimens using a focused ion beam (FIB; Helios, FEI). Chemical analysis was conducted using energy-dispersive spectroscopy (EDS; Oxford, Concord, MA) and semiquantitative compositions were calculated with the Oxford INCA software. Due to known difficulties in quantifying EDS data for the light elements (i.e., B, N, C) in some instances the analysis relied primarily on direct comparison of the EDS spectra. The degree of crystallinity of each material in the composite was assessed using selected-area electron-diffraction (SAED).

5.3 Results

5.3.1 Intermediate temperature test results

The results from the intermediate temperature tests are shown in Figure 5.2 and are plotted as stress at rupture versus time at temperature. The room temperature strength reported in Chapter 3 is included for reference. All samples tested failed within the hot zone. For the stress-rupture tests (filled circles in Figure 5.2), the time to failure increased with decreasing applied stress. For the heat treated samples, exposure to water vapor resulted in greater strength degradation than exposure to dry air. Of note is the correspondence between the results for the 200 MPa stress rupture test (200SR) and the eight hour heat treatment in water vapor (8hrWV). The 200SR sample failed after 8.15 hours, while the residual strength of the 8hrWV sample was 208 MPa.

The fracture surface for a room temperature sample is shown in Figure

5.3(a). It exhibits fiber pull-out in the axial tows, characteristic of CMCs with weak fiber/matrix interphases. Substantial splaying of the transverse tows is also evident. This is consistent with weak bonding between the *tow* and the surrounding matrix, likely a result of heterogeneities in the PIP-derived matrix. The fracture surfaces for the samples tested at temperature are shown in Figure 5.3(b-c) and Figure 5.4. Each exhibits distinct features indicative of strength degradation. The fracture surface of the 300 MPa stress-rupture sample (300SR) (Figure 5.3(b)) indicates minimal pull-out or transverse splaying near the ground edges of the sample. In contrast, near the center of the sample the fracture surface is comparable to the room temperature fracture surface; substantial pull-out of the axial fibers and splaying of the transverse tows is evident. In the 200SR sample (Figure 5.3(c)), the fracture surface is flat up to $\sim$ 1 mm in from the ground edges, with little to no pull-out of the axial fibers. Near the sample center the axial fibers exhibit short pull-out lengths, 2–3 times shorter than in the room temperature sample. Transverse splaying is not evident in the 200SR sample.

The fracture surface for the 8hrWV sample(Figure 5.4(a)) is comparable to that of the 200SR sample. The fracture surface is flat up to $\sim$ 1 mm in from the ground edges, while limited fiber pull-out occurs near the center of the sample. Again little transverse splaying is evident. Unlike the sample tested in water vapor, the fracture surface for the sample heat treated in dry air for eight hours

(8hrDA) does not exhibit a flat fracture front (Figure 5.4(b)). Instead short fiber pull-out lengths are evident throughout the fracture surface. The pull-out lengths are 2–3 times shorter than in the room temperature sample. Splaying of the transverse tows is also evident across the entire fracture surface.

5.3.2 Analysis of fiber fracture mirrors

The size of the fiber fracture mirrors was measured within select regions of the room temperature, 200SR, and 8hrWV samples (highlighted regions in Figure 5.3 and 5.4). The regions investigated are shown in Figure 5.5. Examples of fracture mirrors from each region are shown in Figure 5.6. Within each region every visible fracture mirror was measured. The size of the regions varied depending on the number of images needed to capture all of the fracture mirrors. The number of mirrors measured varied from 51 in the room temperature sample to 276 near the edge of the 200SR sample. Mirrors emanating from internal flaws were distinguished from mirrors emanating from surface flaws. There were also cases in which the fracture mirror encompassed the entire fiber. In these cases the mirror size was equated to the average fiber diameter ($a = 2R = 13\,\mu\text{m}$).

The fiber strength, σ_f, can be related to the fracture mirror size, a, by the relationship

$$\sigma_f = c/\sqrt{a} \tag{5.1}$$

where c is a constant. Historically, for glasses a is a measure of the mirror-mist radius, while in poly-crystalline ceramics it is easier to measure the mist-hackle radius (Quinn, 2007). The mist-hackle radius was measured in this study. From Equation 5.1, qualitative comparisons of the fiber strength can be made using the cumulative probability distribution of $1/\sqrt{a}$ (Figure 5.7). Error bars indicate a relative error of 17 % for the measurement of a. The error was estimated from the largest and smallest estimates of the mist-hackle radii for five fracture mirrors chosen at random from each region. Mirrors emanating from internal versus surface flaws are illustrated with filled symbols and empty symbols, respectively.

For the room temperature sample, the cumulative probability distribution is centered about $1/\sqrt{a} = 1$. For fibers near the edge of both the 200SR and 8hrWV samples the distributions are centered around $1/\sqrt{a} =\sim 0.65$. The distribution for fibers near the center of the 200SR sample lies approximately halfway between the room temperature distribution and the distribution for the fibers near the edge. Fibers near the center of the 8hrWV sample have a similar distribution to the room temperature fibers.

The spatial distribution of the measured values of $1/\sqrt{a}$ for the embrittled samples are depicted in Figure 5.8. The value of $1/\sqrt{a}$ is denoted by the color maps, while the mirror locations are denoted by the symbols. Mirrors emanating from internal flaws are designated with filled circles, mirrors emanating from surface flaws are designated with empty circles, and mirrors that encompass the entire fiber ($a = 2R$) are designated with x's. The values of $1/\sqrt{a}$ appear to be randomly distributed within each region. There does appear to be a spatial correlation between the locations of mirrors with $a = 2R$ near the edge of the 200SR and 8hrWV samples. Their locations appear to form an inter-connected network. This suggests the presence of an inter-connected network of defects in the matrix, leading to accelerated embrittlement of the fibers locally. Further analysis is needed to confirm this hypothesis. Near the center of the 8hrWV sample, all of the fracture mirrors emanating from internal flaws are congregated near the top of the region analyzed. Within this sub-region, five of the ten mirrors emanating from internal flaws are clustered together. This is possibly a result of variations in the composite microstructure and merits further analysis.

The percentage of fibers within each region with internal flaws, surface flaws, and mirrors with $a = 2R$ are shown in Figure 5.9. In all regions the majority of fracture mirrors emanate from surface flaws. The largest percentage of internal flaws (25 %) was found in the room temperature sample. A single internal flaw was found near the edge of the 200SR sample, while no internal flaws were found near the edge of the 8hrWV sample. Internal flaws were found in 2 % of the fibers characterized near the center of the 200SR sample and 15 % of the fibers near the center of the 8hrWV sample. The opposite trend was found for mirrors encompassing the entire fiber, with the largest prevalence being near the edge of the 200SR and 8hrWV samples (30–40 %). Approximately 10 % of the mirrors analyzed near the center of the 200SR and 8hrWV samples and $< 5\,\%$ of mirrors in the room temperature sample encompassed the entire fiber.

5.3.3 Microstructural observations

Transverse cross-sections were prepared $\sim$ 3 mm below the fracture surfaces. The cross-sections were prepared through material that was within the hot zone and thus provides a comparable depiction of the microstructural evolution within the composite as would be expected at the fracture surface. SEM micrographs of regions near the edge and center of each sample are shown in Figure 5.10 and 5.11. Micrographs of a polished as-processed coupon are included for comparison. Near the center of each sample the BN coatings appear intact. Extensive oxide formation is evident between the fibers and the matrix near the edges of the 200SR and the 8hrWV samples. In both cases, oxide formation is spatially in-homogeneous: variations are seen from fiber to fiber and even around individual fibers. The BN coatings appear intact throughout the 8hrDA and 300SR samples.

A detailed investigation of the composite microstructure was conducted using TEM. Lamellae were extracted from a region between adjacent fibers near the middle of an internal tow, such that each specimen included portions of two fibers with associated interphases as well as the inter-fiber matrix. Locations for analysis included: *(i)* near the center of an as-processed CMC coupon, *(ii)* near the edge and *(iii)* center of the 8hrDA specimen, and *(iv)* near the edge and *(v)* center of the 200SR specimen. In each case the location was chosen to provide a best-case representation of the matrix, i.e., devoid of large pores and micro-cracks, and in which the matrix contained both particles and polymer-derived material.

As-processed microstructure

TEM micrographs of the as-processed composite microstructure are shown in Figure 5.12(a). Select SAED patterns are shown in Figure 5.12(b-e). The fibers were found to be crystalline SiC with grains 5–10 nm in size (Figure 5.12(a,d)). They contained minimal O ($\sim$ 2 %), consistent with the manufacturer specifications. They were coated with a bi-layer of BN and Si_3N_4. The nominal BN layer comprised: 23 % B, 22 % C, 35 % N, 17 % O, and 4 %

Si. SAED indicates the presence of a nano-crystalline phase within the BN layer. The diffraction rings are generally constituent with both hexagonal BN and graphite structures (Figure 5.12(e)). The diffuse nature of the rings makes it difficult to distinguish between the two structures and may imply that the material is only minimally crystalline. These observations support literature reports indicating that CVD BN consists of a network of turbostratic BN and C (Pippel et al., 2000). This network readily absorbs O to satisfy the dangling bonds on the turbostratic BN (Dietrich et al., 1998). The Si_3N_4 layer was found to be crystalline, with grains on the order of 50 nm in size (Figure 5.12(c)). EDS analysis suggested minimal O and C ($\sim$ 5 % and 7 %, respectively) within the Si_3N_4 layer. This may be accounted for in part by x-rays originating from the adjacent layers due to the use of a probe comparable in size to the layer thickness. The matrix consists of crystalline Si_3N_4 particles embedded in an amorphous polymer-derived phase (Figure 5.12(b)). The polymer-derived phase contains nearly equal parts Si, C, N, and O. Porosity is on the nm scale is distributed throughout the polymer-derived matrix, while clusters of μm sized pores are found adjacent to the Si_3N_4 particles.

Oxidation in dry air

TEM micrographs and select EDS spectra from the 8hrDA lamellae are shown in Figure 5.13 and 5.14. Few micro-structural changes were evident relative to the as-processed condition: the composition of the fibers was unchanged; oxide formation was not evident on the surface of the fibers; and the fiber coatings remained intact both near the edge and the center of the sample. EDS analysis indicates slight compositional variability in the BN coatings. In the 8hrDA sample, the BN layers have greater concentrations of Si and reduced concentrations of C and B in comparison to the as-processed sample (Figure 5.14(a)). These compositional variations are presumed to be inherent to the CVD processing. Of additional note is that the Si_3N_4 layer near the edge of the 8hrDA sample is amorphous. This is indicated by the lack of visible grains in the TEM micrograph in Figure 5.13(b) and was confirmed by SAED. EDS analysis indicates that the layer is still nominally pure Si_3N_4, suggesting that the lack of crystallinity is a result of variations in CVD processing rather than the result of microstructure evolution during the environmental exposure (i.e., oxidation). The PIP-derived matrix in the 8hrDA sample is comparable to the as-processed matrix. A slight reduction in C and N concentrations is suggested by EDS, but the ratio of the O and Si peaks is the same as in the as-processed matrix (Figure 5.14(b)). This indicates that the polymer-derived matrix has not been appreciably oxidized. The reduction in C and N could result either from intrinsic variations in the composition or limited, selective oxidation or out-gassing (i.e., pyrolysis).

Oxidation in water vapor

TEM micrographs and select EDS spectra from the 200SR lamellae are shown in Figure 5.15-5.16 and 5.17. EDS analysis of the fibers indicates that their composition is unchanged from the as-processed state. In both lamellae oxide layers formed on the fiber surfaces. EDS analysis indicates that the oxide is nominally pure silica. Near the center of the sample this layer was 20–40 nm thick and formed between the fiber and the BN coating. Near the edge of the sample the layer was 120–260 nm thick. The boundary between the oxide and the fiber was flat near the sample center. In contrast, near the edge the fiber/oxide interface was more diffuse. Darkfield imaging indicates that SiC grains are present throughout the fiber/oxide transition region, suggesting that this could be a two phase region with unoxidized SiC grains surrounded by silica.

The fiber coatings — BN and Si_3N_4 layers — remain intact near the center of the 200SR sample. SAED indicates that the BN layer remains nano-crystalline. Near the center of the 200SR sample, the relative heights of the B, C, O, and Si peaks are comparable to the as-processed sample, while an increased concentration of N is indicated (Figure 5.17(a)). This is suspected to be a result of inherent variations in the BN composition during CVD processing. Near the sample edge the fiber coatings have been oxidized considerably, resulting in the porous layer evident between the silica and matrix in Figure 5.15(b) and 5.16. EDS analysis indicates that in comparison to the as-processed BN, this layer has increased concentrations of Si, O, and N, with reduced concentrations of C and B (Figure 5.17(a)). SAED indicates that the crystalline component of the layer is similar to the original BN layer, i.e., containing hexagonal BN and/or graphite domains. Darkfield imaging using the (002) hBN ring, Figure 5.16(c), reveals a dispersion of fine crystallites in this layer. The relative ratios of the B and C peaks in the EDS spectra indicate that the reduction in C content is greater than the reduction in B. This suggests that the crystalline phase is likely residual turbostratic BN that has is dispersed in the Si-O(-N-B-C) glass. The extensive porosity in the layer is likely the result of N_2 and CO evolution as the Si_3N_4 layer oxidizes and graphite is removed from the BN layer.

The PIP-derived phase of the matrix in the 200SR sample has been oxidized. This is evident by increased concentrations of O, reduced concentrations of C and N, and coarsening of the porosity (Figure 5.17(b)). The extent of oxidation is greater near the edge than in the center of the sample.

5.4 Discussion

5.4.1 Effect of applied stress

In MI and CVI composites, intermediate temperature embrittlement occurs after the formation of matrix cracks (Heredia et al., 1995). In contrast, the results of this study indicate that in PIP-based CMCs embrittlement occurs even in the absence of an applied stress. This is evident by the comparable results of the 200SR and 8hrWV samples. Measurements of the size of the fiber fracture mirrors indicated that the strength of fibers within the flat fracture regions of these sample were uniformly degraded with respect to the room temperature fiber strengths. Strength degradation in the absence of an applied load also occurred, albeit to a lesser extent, in dry air. These results suggest that the embrittlement process is facilitated by oxidant ingress through existing porosity and micro-cracks formed during matrix processing. The implication is that embrittlement of PIP-based CMCs is controlled predominately by the time at temperature for a given exposure environment.

Oxidant ingress through the matrix microstructure is further evident through heterogeneity in the observed oxidation and embrittlement. This is manifest in the non-uniformity in oxide formation near the edges of the 8hrWV and 200SR samples (Figure 5.10 and 5.11), as well as the lack of spatial correlation between the measured fiber strengths (Figure 5.8). Heterogeneities in the matrix microstructure also appear to affect the depth of oxidant ingress. Oxidant ingress is evident throughout the 200SR sample: fibers near the center of 200SR sample exhibited reduced strengths with respect to fibers in the room temperature specimen; and microstructural analysis indicated the presence of a thin oxide layer between the fiber and the BN layer, as well as oxidation of the PIP-derived matrix. In contrast, the distribution in strength for fibers near the center of the 8hrWV sample were unchanged from the room temperature sample. While a TEM lamella was not extracted from the center of the 8hrWV sample, the lack of fiber embrittlement suggests that internal oxidation did not occur. It is therefore likely that within the as-processed microstructure, oxidant ingress is restricted to existing networks of interconnected porosity/micro-cracks that reach only a subset of fibers/tows. It is possible that the formation of matrix cracks during stress-rupture tests could connect isolated pathways within the matrix microstructure, allowing for oxidant ingress further into the composite. This does not, however, appear to effect the failure strength of the composite, likely because the matrix cracks do not appreciably increase the rates of oxidant ingress. In any case, the matrix microstructure was found to play an important role during internal oxidation and embrittlement.

5.4.2 Intermediate temperature oxidation

The mechanisms of intermediate temperature oxidation in the PIP-derived SiC/SiCN CMC studied here are inconsistent with the existing understanding in the literature. In this study, oxidation occurred preferentially within select constituents of the composite. The nature and rate of oxidation are dependent on both the environment and distance from the ground edge. Following exposure in dry air, evidence of oxidation was not found in the matrix or fiber coatings (BN and Si_3N_4). The reduction in retained strength of the 8hrDA sample, 55 % of the room temperature strength, however, suggests that an embrittlement mechanism is active. One plausible explanation is slow-crack growth due to oxidation of free-C within the fibers. Near the center of the sample exposed to water vapor, oxidation was restricted to the Si- and C-containing phases, namely the fiber and the polymer derived matrix phase. A silica scale was evident between the fiber and an intact BN coating. Measurements of the size of the fiber fracture mirrors indicated degradation in the fiber strengths, suggesting oxidation of free-C leading to slow-crack growth. Near the ground edge of the sample exposed to water vapor, oxidation was more severe: embrittlement of the fibers was evident; a silica scale had formed on the fibers; evidence of oxidation was found in the matrix; and the fiber coatings had been oxidized. The resulting oxide formed by the fiber coatings contained primarily Si, O, and N along with residual crystallites of BN. This suggests that even near the ground edge, oxidation is still occurring preferentially in the non B-containing phases.

However, the existing understanding in the literature is that the BN fiber coating oxidizes first (Morscher, 1997; Morscher et al., 2000; Ogbuji, 1998, 2003). The boria formed by the oxidation of BN is predicted to either volatilize in water vapor containing environments, exposing the fibers to oxidation, or react with neighboring SiC and SiO_2 to form a borosilicate glass (Jacobson et al., 1999a,b). Volatilization of the B from the borosilicate or continued addition of Si is predicted to increase the viscosity of the glass and eventual bond the fibers to the matrix. This understanding is derived from experimental results for model systems (Jacobson et al., 1999b) and mini-composites (Morscher, 1997). In the model systems, the BN layers are directly exposed to the environment, facilitating removal of the volatile boron-hydroxide species, the rate controlling step for B volatilization. The mini-composites, consisting of a CVD matrix, developed matrix cracks with openings on the order of 5–15 µm (Morscher, 1997). Additionally, the distance from the fiber coatings to the ambient environment is relatively short (10s of µm) due to the size and shape of the mini-composites. The direct diffusion paths in both cases (Jacobson et al., 1999b; Morscher, 1997) allow for relatively high flux of both oxidant to and volatile species from the reaction front. The conditions (i.e., a_{O_2})

within the oxidizing regions could therefore be similar to the surface environment. The present results meanwhile suggest that while PIP-derived matrix microstructure allows sufficient oxidant ingress to embrittle the composite, the BN is shielded against oxidation and volatilization, even over relatively short distances ($< 100\,\mu\mathrm{m}$).

The effect of the matrix microstructure on oxidant ingress was investigated first by comparing the thickness of the silica layer that formed on the fibers with predictions for parabolic oxidation of SiC (Figure 5.18). The oxidation of SiC to form silica has been demonstrated to be comparable to the oxidation of Si (Opila, 1994). The classic treatment of the oxidation of Si is provided by Deal and Grove (1965) and indicates that oxidation is controlled by the inward diffusion of the oxidant species through the growing oxide layer. The resulting parabolic oxidation kinetics follow the relationship $x^2 = Bt$, where x is the oxide thickness, B is the parabolic rate constant and t is time. The parabolic rate constant is defined as $B = \frac{2D_{eff}C^*}{N}$, where D_{eff} is the diffusivity of the oxidant through the oxide, C^* is the solubility of the oxidant in the oxide, and N is the number of oxidant molecules incorporated into a unit volume of oxide. The oxidation of SiC in dry air and water vapor has been well studied. Parabolic rate constants for oxidation in dry air were measured by Deal and Grove (1965) (for Si) and by Ogbuji and Opila (1995) (for SiC). Parabolic rate constants for oxidation in water vapor were measured by Deal and Grove (1965) (for Si) and by Opila (1999) (for SiC).

To compare the reported parabolic oxidation rates to the present observations, all rate constants were scaled for the oxidation of SiC at 800 °C in 0.2 atm of O_2 or 1 atm of water vapor. The predicted oxide thicknesses after eight hours are compared with the oxide thicknesses measured from the TEM micrographs (Figures 5.13 and 5.15). A significant difference was seen between the predicted and measured values (Figure 5.18). In water vapor, the predicted oxide thickness was 750–850 nm, three to five times greater than the measured values near the edge of the 200SR sample, and almost an order-of-magnitude greater than the values measured near the center of the 200SR sample. In dry air, the predicted oxide thickness, 30–100 nm, is an order-of-magnitude smaller than that in water vapor, but no visible oxide was found in the 8hrDA sample. These results suggest that the rate limiting step for internal oxidation is the transport of oxidants through the composite and not diffusion through the oxide layer on the fibers, as predicted by parabolic oxidation. This is consistent with the oxide thickness decreasing with increasing distance from the ground edge. If the comparatively slow transport of the oxidants through the composite microstructure is the rate controlling step, it is conceivable that the local O_2 activity could be considerably depressed relative to the external environment.

To determine the effect of O_2 activity on the oxidation process, the thermodynamics of SiC, Si_3N_4, and BN oxidation were considered. Calculations were performed using the FactPS pure substances database in the Equilibrium module of the FactSage software package. Oxidation of each constituent was simulated by initializing pure, SiC, Si_3N_4, or BN at 800 °C in an environment containing 1 atm argon (to generate an initial gas phase) and an oxygen activity sufficiently low to prevent oxidation of the constituent ($a_{O_2} = 10^{-40}$, $fugacity_{O_2} = 10^{-40}\,\text{atm}$). The equilibrium phase fraction was then calculated as a function of oxygen activity to a maximum a_{O_2} of 0.1 ($fugacity_{O_2} = 0.1\,\text{atm}$), which was sufficient to fully oxidize the starting components and produce a measurable excess of O_2 gas. The calculated phase fractions, excluding argon and minor gas constituents, are plotted as a function of oxygen activity in Figure 5.19 (a), (b), and (c) for SiC, Si_3N_4, and BN, respectively. In each diagram, the pure constituent is shown as the only phase on the left, representing the unoxidized condition, while the final oxidation products appear to the right.

Interpretation of the results for Si_3N_4 and BN is straightforward. Once a critical oxygen activity is reached (a_{O_2} of 1.5×10^{-29} and 4.0×10^{-23}, respectively), the Si_3N_4 and BN oxidize to produce a combination of condensed oxide (SiO_2 or B_2O_3) and N_2 gas. The equilibria for the oxidation of SiC is more nuanced. The thermodynamics suggest that the silicon oxidizes first, producing a mixture of C and SiO_2 once the oxygen activity reaches 1.6×10^{-32}. The carbon remains relatively resistant to oxidation, evidenced by a low CO:C molar ratio, until the oxygen activity is above $\sim 10^{-26}$. As the oxygen activity is further increased the graphite is progressively converted to CO and then the CO oxidizes to form CO_2. While the kinetics of SiC oxidation in the present system may not allow for graphite formation, the calculated oxidation of carbon provides additional information about the expected oxidation conditions for the constituent phases in the composite.

The thermodynamic calculations predict that with increasing a_{O_2} the constituents of the fiber/coating system will oxidize in the following order: SiC fibers, Si_3N_4 fiber coating, free C, and finally the crystalline BN within the fiber coating. The oxidation of the polymer-derived matrix phase is not explicitly modeled but the local Si-C and Si-N nanostructure may be expected to oxidize at a_{O_2} similar to that for SiC and Si_3N_4 oxidation. Oxidation caused by H_2O or OH- species were not explicitly modeled, but the oxidation hierarchy is expected to be similar.

The observed microstructural changes in Figures 5.13 and 5.15 are in general agreement with the calculations. There were no indications of oxidation within the 8hrDA sample. This suggests that a_{O_2} within the observed fiber tows is less than the critical value needed to oxidize any of the constituents (i.e., less than 1.6×10^{-32}). Near the center of the 200SR sample a thin silica scale was present on the fibers and evidence of oxidation was found in the PIP-matrix. This suggests that the effective a_{O_2} in the interior of the composite is between that needed to oxidize SiC and Si_3N_4. Near the edge of the 200SR sample oxidation was evident for all of the Si-based phases (SiC fibers, PIP matrix, and Si_3N_4 fiber coating), but residual crystallites of BN were present within the Si-O-N(-B) glass formed upon oxidation of the Si_3N_4. This indicates that the a_{O_2} is sufficiently high to oxidize the Si-based phases and is likely fixed near 4.0×10^{-23}, the value needed for BN oxidation.

The combination of the thermodynamic calculations and microstructure observations provide insight into the dynamics of internal oxidation of CMCs with PIP-derived matrices. First, it is evident that while both the BN fiber coating and the polymer derived matrix phase have a considerable oxygen concentration, the oxygen activity remains quite low. It would otherwise be expected that oxygen within the CMC would react with the Si_3N_4 or SiC fiber during either the processing heat treatments or the 8hrDA experiment. Second, if there are no kinetic limitations on the SiC or Si_3N_4 oxidation reactions, it is expected that both phases would oxidize preferentially to free-C and BN in an oxygen-starved environment. If inward oxidant flux is less than the SiC oxidation rate (governed either by the reaction rate or the local transport through the growing SiO_2 layer on the fibers) it is conceivable that the a_{O_2} could remain below that required to oxidize BN or free C for an extended period. If, however, oxidant penetration outpaces SiC oxidation, the a_{O_2} would rise until additional phases begin to oxidize. The findings of this study generally indicate that oxidant ingress is the rate controlling step in all cases except near the surface of the 200SR specimen. As such, the BN and Si_3N_4 layers are intact in the dry air specimen and in the center of the 200SR specimen. This result is apparently at odds with the proposed mechanism for fiber embrittlement: selective oxidation of free-C in the Hi-Nicalon fibers. Specifically, if a_{O_2} is too low to initiate SiC oxidation, it is unclear how carbon could be extracted from the fibers. One plausible explanation is that the nanostructure of the system (e.g., carbon layers between SiC grains) changes the thermodynamics relative to the bulk phases, leading to a different reaction hierarchy. For example, the extraction of carbon from the fibers could be more accurately viewed as the substitution of O for C at SiC grain boundaries rather than the oxidation of bulk graphite. The energetics of such situations have not been explicitly studied and merit investigation.

Regardless of the nuanced issues associated with the local environment within the composite, it is clear that the oxidation mechanisms put forth in the literature involving BN oxidation and volatilization are not active in the interior of these CMC specimens. This suggests that CVD BN is permeable to oxidants, enabling environmental attack of the fiber prior to BN oxidation/volatilization. Similar findings have been presented by More et al. (1999)

for the oxidation of thin section of SiC/BN/SiC composites prepared for TEM analysis. Oxidation at the BN/fiber interphase increased with increasing concentrations of O in the BN. These results suggesting that O within the BN plays an important role in oxidant transport and must be minimized to produce protective fiber coatings.

5.4.3 Intermediate temperature embrittlement

Four main theories, described in detail in Chapter 1, have been proposed to explain intermediate temperature embrittlement of SiC/SiC CMCs. The proposed mechanisms are: *(i)* oxidation induced slow-crack growth in the fibers due to removal of free-C from the grain boundaries, followed by subsequent oxide formation (Forio et al., 2004; Gauthier et al., 2009; Lamon and R'Mili, 2012); *(ii)* growth stresses caused by the molar volume expansion accompanying silica formation on the fiber surface (Xu et al., 2014); *(iii)* stress intensification caused by continued formation of oxide at the oxide/fiber interface after the gap between the matrix and the fiber has been filled (Xu et al., 2014); and *(iv)* stress concentration upon strong bonding of the fiber and matrix due to silica formation (Glime and Cawley, 1998; Morscher and Cawley, 2002). The implications of the results from this study on the efficacy of each proposed mechanism follows.

Fiber embrittlement was indicated by the fracture mirror analysis for samples tested in both dry air and water vapor. In dry air, strength degradation occurred in the apparent absence of additional fiber surface, fiber coating, or matrix oxidation. This suggests that the strength degradation was most likely caused by undetected internal oxidation of the fibers. Determination of the relative strength of the fibers from measurements of the size of the fiber fracture mirrors is ongoing and will be used to verify degradation of the fiber properties. Measurements of the size of the fiber fracture mirrors for samples tested in water vapor indicate a reduction in the fiber strength with respect to fibers in a sample tested at room temperature. Fiber embrittlement could be caused by slow-crack growth within the fibers.

Silica formation was evident on the fiber surface in the samples tested in water vapor. Silica was found to have formed between the fiber and the BN layer near the center of the 200SR sample. Near the edge of the sample the silica layer was between the fiber and the silica-based glass produced upon oxidation of the BN/Si_3N_4 fiber coating. The models developed by Xu et al. (2014) predicting stress elevation due to oxide formation on the fibers indicate that the extent of stress elevation is controlled by the competing rates of oxide formation and relaxation due to viscous flow. The oxidation rates of silica within the 200SR sample were found to be significantly reduced in comparison to the predicted parabolic oxidation rates. Additionally, the presence of water vapor has been shown to reduce the viscosity of silica (Opila, 1999), which would accelerate relaxation. In combination, this suggests that the mechanisms regarding oxide formation on the fiber surface will be inhibited.

Near the edge of the samples tested in water vapor, the BN/Si_3N_4 fiber coating has been fully oxidized. The resulting oxide contained significant N, crystallites of BN, and porosity. It is unknown to what extent this layer would bond the fibers to the matrix and prevent fiber slip. Additionally, embrittlement was found to be comparable for samples tested under static loading to those tested in monotonic tension after oxidation. This suggests that the dominant embrittlement mechanism does not require a change in applied stress as would be the case for fiber/matrix bonding.

The results of this study suggest that intermediate temperature embrittlement in PIP-based CMCs is dominated by degradation of the fibers. The leading theory as to the cause of embrittlement is oxidation-induced slow-crack growth in the fibers. Further study is needed to verify this hypothesis. Outstanding questions remain regarding the oxidation of free-C, which is the proposed mechanism by which slow-crack growth occurs.

Strength degradation was greater for samples exposed to water vapor than to dry air. Additionally, exposure to water vapor resulted in internal oxidation of the Si-based constituents, while no visible oxidation was evident after exposure to dry air. This suggests greater ingress of water vapor than dry air. It remains unclear if the accelerated degradation in strength is solely a result of greater ingress of water vapor with respect to dry air, or to what extent internal oxidation contributes to composite embrittlement, i.e., could it activate additional embrittlement mechanisms?

5.5 Conclusions

A preliminary experimental study of intermediate temperature embrittlement in a PIP-based SiC/SiCN CMC was presented. Test coupons were tested at 800 °C in dry air and water vapor environments. Some samples were tested under static stress-rupture, while others were heat treated for eight hours prior to the determination of their retained strength under monotonic tension. Intermediate temperature embrittlement in PIP-derived composites is a complex process with multiple competing phenomena occurring in a system with an inherently complex microstructure. Aspects of these phenomena and their relationship with the composite microstructure are not fully understood. While further study is needed several insights have been gained regarding intermediate temperature oxidation and embrittlement:

1) Oxidant ingress occurs at appreciable rates through the residual porosity and micro-cracks inherent to PIP-processing without the application of load.

2) Strength degradation is accelerated in water vapor containing environments versus dry air environments. The degradation in composite strength is a result of degradation in the fiber strengths.

3) Internal oxidation occurs preferentially in the Si and C containing constituents of the composite. This is in contrast to the current understanding in the literature which predicts BN oxidation/volatilization to occurred first.

4) The rate of internal oxidation is controlled by oxidant ingress through the composite microstructure. It is greater in water vapor containing environments than in dry air environments.

Further study is needed to elucidate the mechanisms controlling these observations. While degradation in the fibers strengths is surmised to be a result of oxidation-induced slow-crack growth in the fibers, further analysis is needed to verify this hypothesis. This includes determination of the fiber strengths via measurement of the size of the fiber fracture mirrors after oxidation in dry air. Supplementary information regarding the fracture process could be gleaned by measuring pull-out lengths of the fibers. These measurements could be facilitated using μCT. Additional stress-rupture tests are needed to confirm that for oxidation in dry air, as was found in water vapor, the effects of applied load on strength degradation are secondary to the time at temperature. Intermediate temperature tests in an Ar environment would help to deconvolution the effects of temperature and oxidation on the composite strength.

The results of this study provide a contrasting process for internal oxidation at intermediate temperatures to that presented in the literature. These observations are convoluted by the complexity of the constituent phases in the composite. While thermodynamic calculations provide insights to the hierarchy of oxidation as a function of O_2 activity, questions remain regarding the oxidation processes. Further study is needed to ascertain the role of the oxidation kinetics during oxidation, particularly as it relates to the complexity of the microstructure of the constituent phases. Controlled oxidation experiments on small coupons as well as on the individual constituents, or simplified systems, would be insightful. Studies of this type would also provide information regarding the mechanisms by which water vapor and dry air are transported through the matrix microstructure. A better understanding of the mechanisms and processes controlling internal oxidation would provide insight into the role of internal oxidation on the embrittlement process.

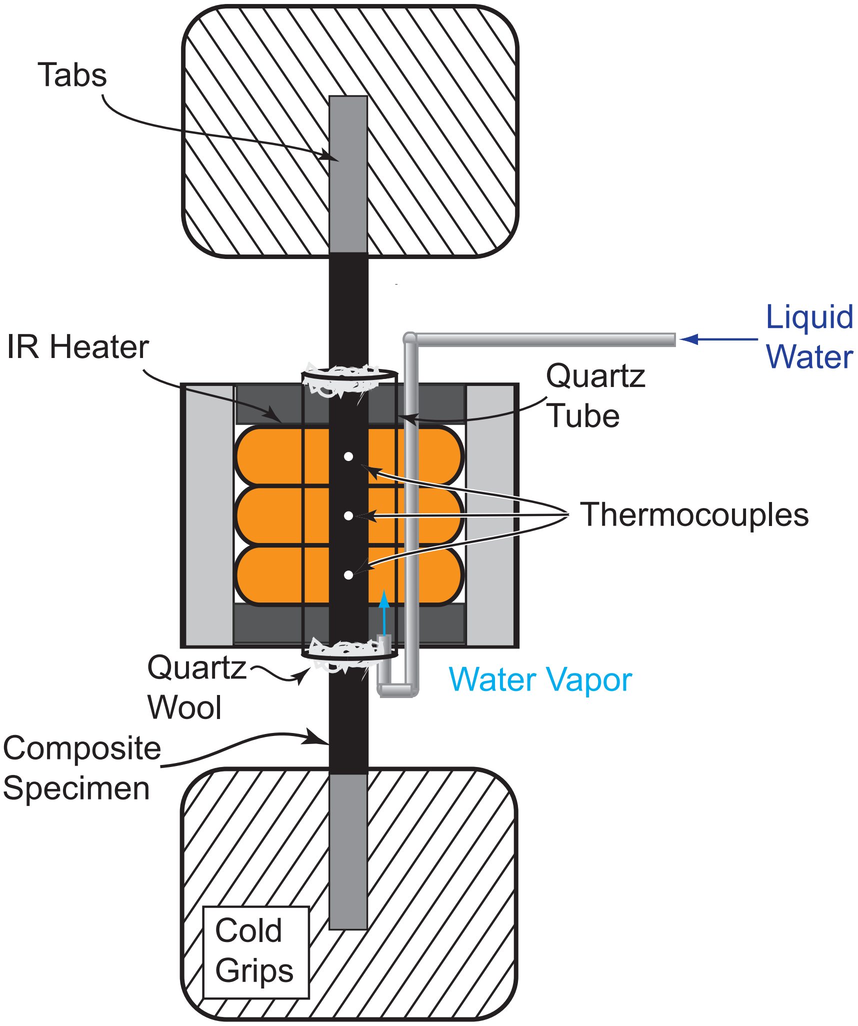

Figure 5.1: Experimental set up for intermediate temperature testing.

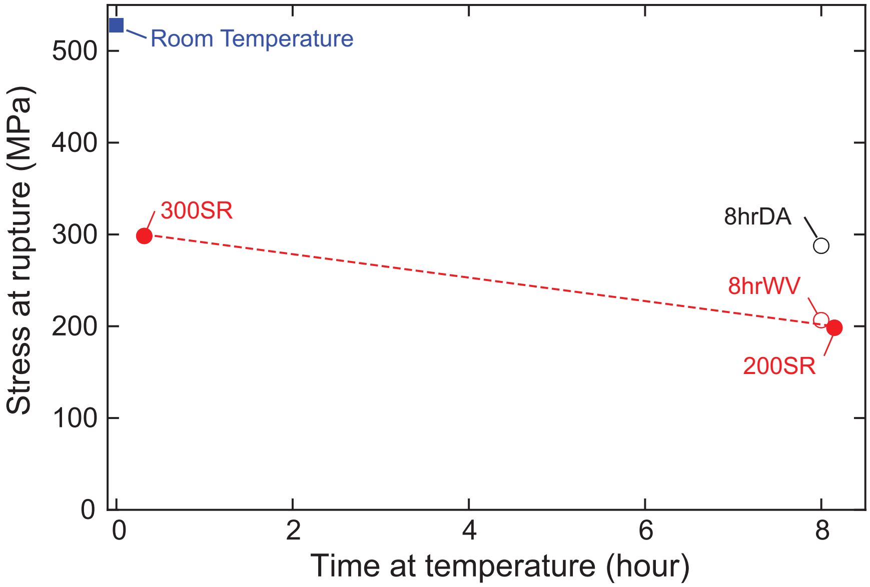

Figure 5.2: Results of intermediate temperature testing. The room temperature strength (blue square) is provided for reference. Stress-rupture tests are depicted by filled circles. Residual strength of heat treated samples are depicted with empty circles.

(a) Room temperature

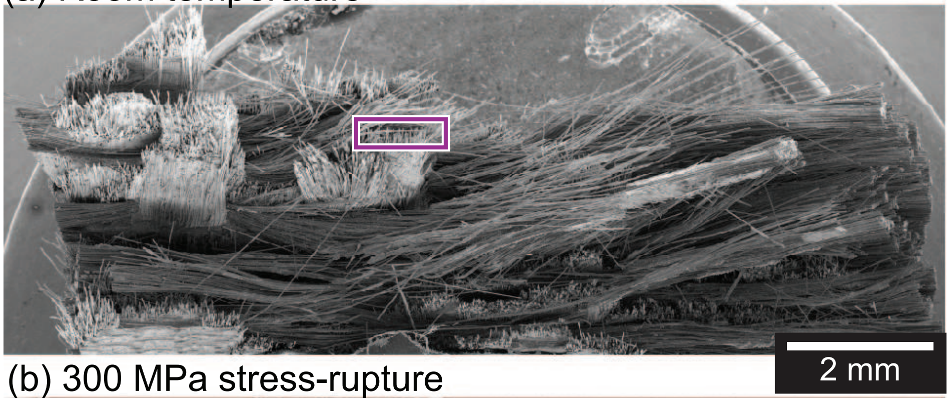

(b) 300 MPa stress-rupture

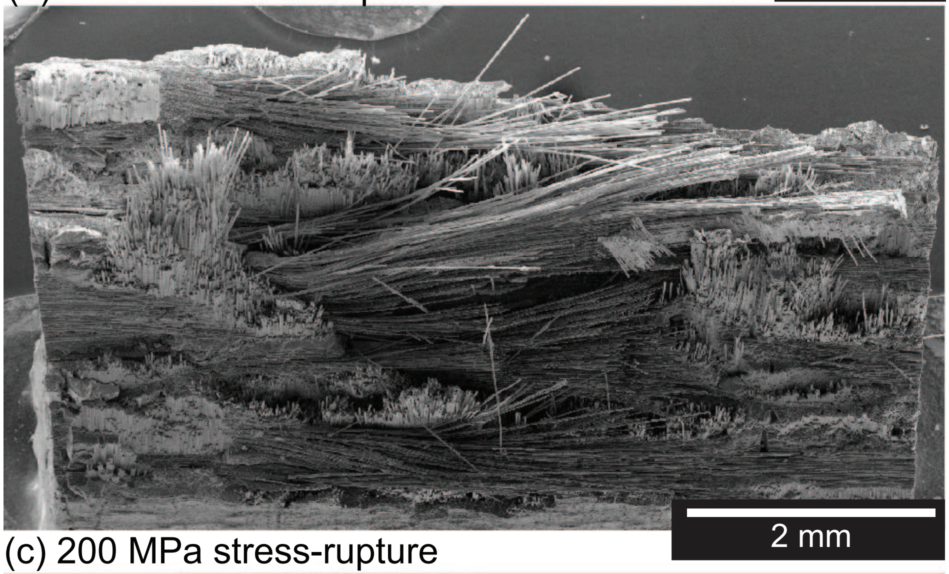

(c) 200 MPa stress-rupture

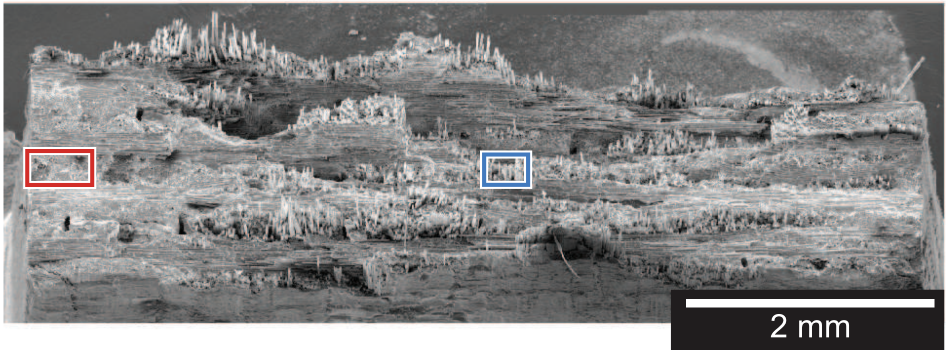

Figure 5.3: Fracture surfaces after: (a) room temperature tension and (b-c) intermediate temperature stress-rupture.

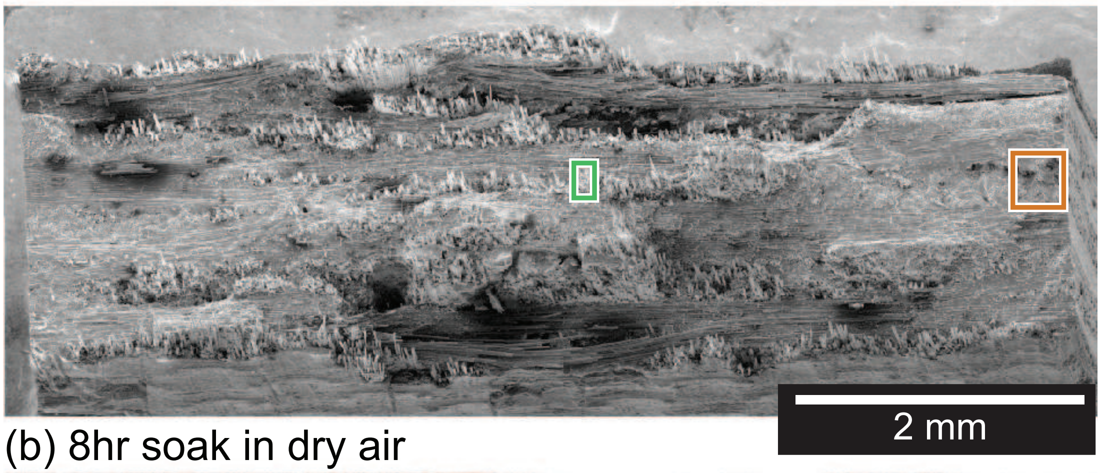
(a) 8hr soak in water vapor


(b) 8hr soak in dry air

Figure 5.4: Fracture surfaces after monotonic tension following eight hour heat treatment in (a) water vapor and (b) dry air.

(a) Room temperature

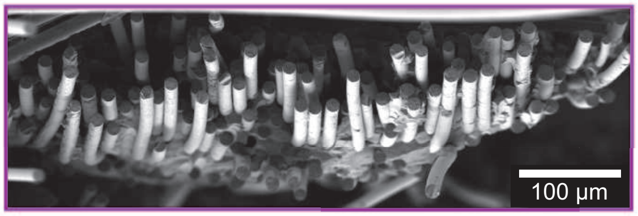

(b) 200SR - Edge

(c) 200SR - Center

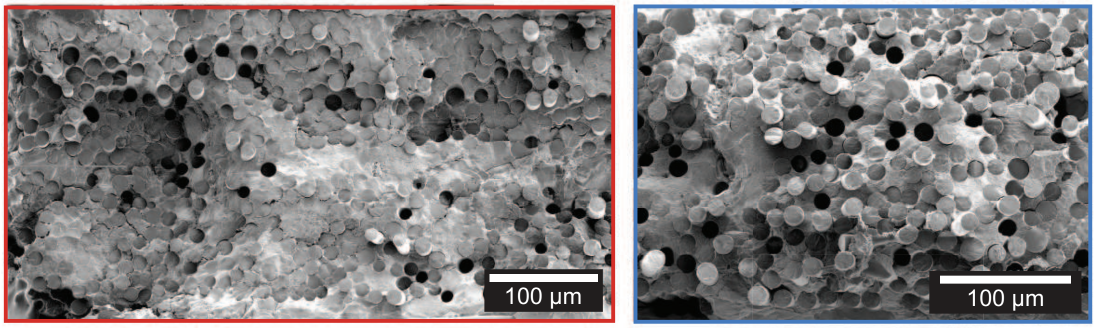

(d) 8hrWV - Center

(e) 8hrWV - Edge

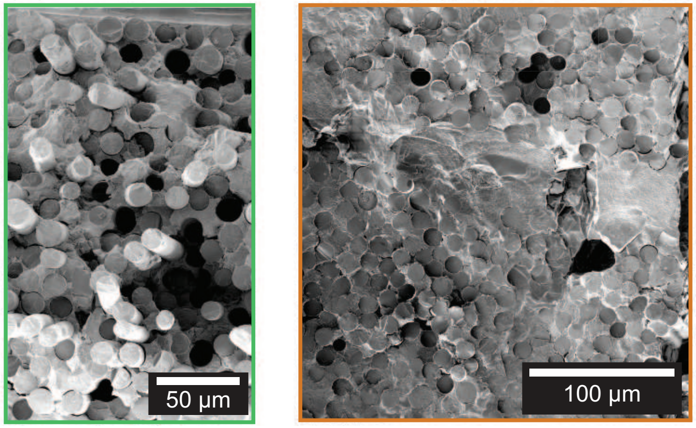

Figure 5.5: Regions of (a) room temperature tension sample, (b-c) 200SR sample, and (d-e) 8hrWV sample in which fracture mirrors were measured.

(a) Room temperature

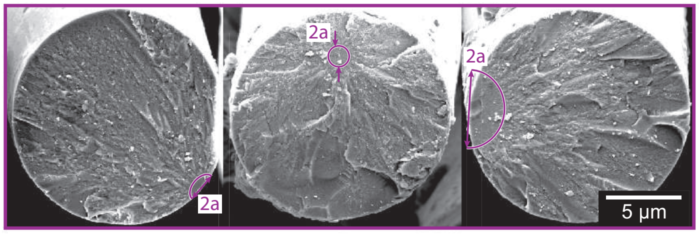

(b) 200SR - Edge

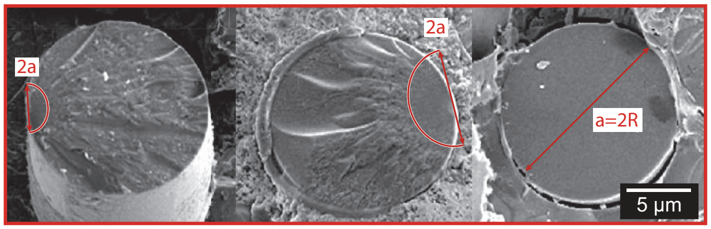

(c) 200SR - Center

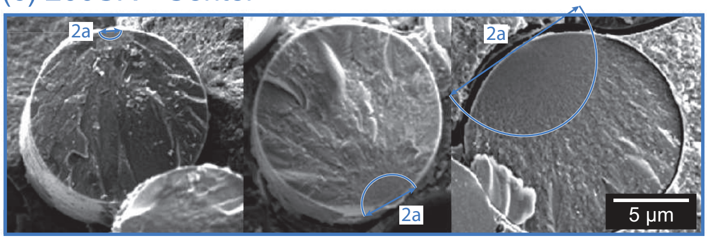

(d) 8hrWV - Center

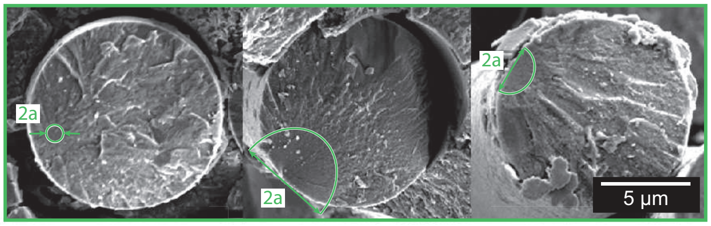

(e) 8hrWV - Edge

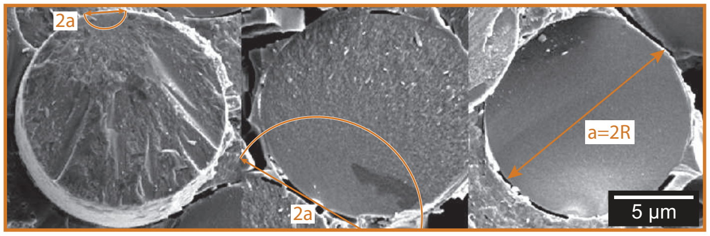

Figure 5.6: Examples of fracture mirrors from the (a) room temperature tension sample, (b-c) 200SR sample, and (d-e) 8hrWV sample.

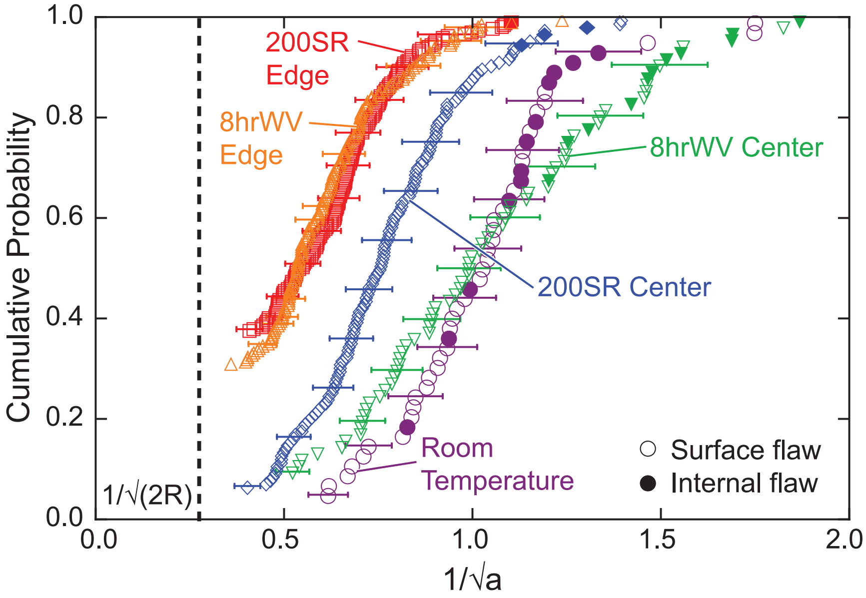

Figure 5.7: Cumulative probability distributions of $1/\sqrt{a}$. Error bars indicate a relative error of 17 % for the measurement of a.

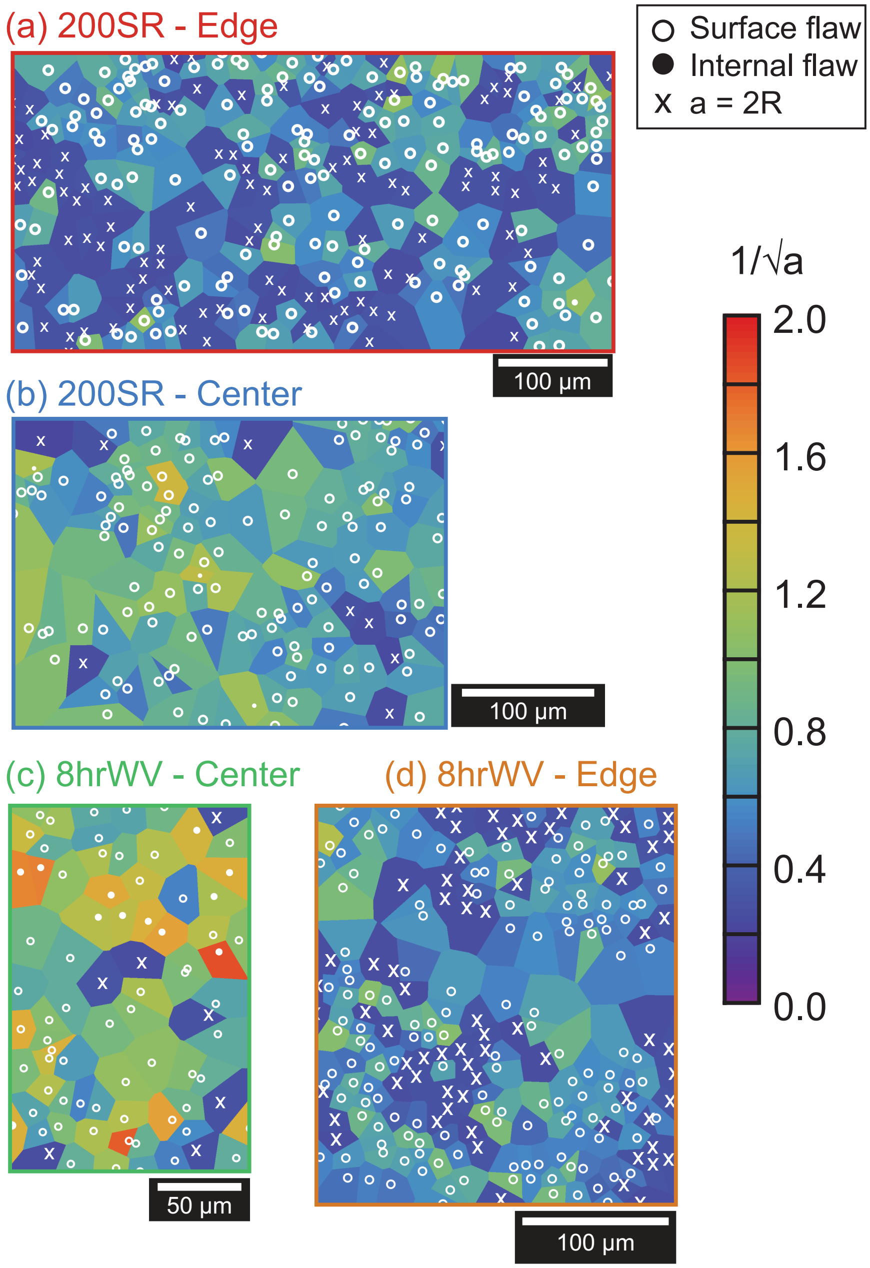

Figure 5.8: Spatial distribution of $1/\sqrt{a}$ for the 200SR and 8hrWV samples. $1/\sqrt{a}$ is denoted by the contour colors. Fracture mirror locations denoted symbolically with filled circles indicating mirrors emanating from surface flaws, empty circles indicating mirrors emanating from internal flaws, and x's indicating mirrors the encompass the entire fiber ($a = 2R$).

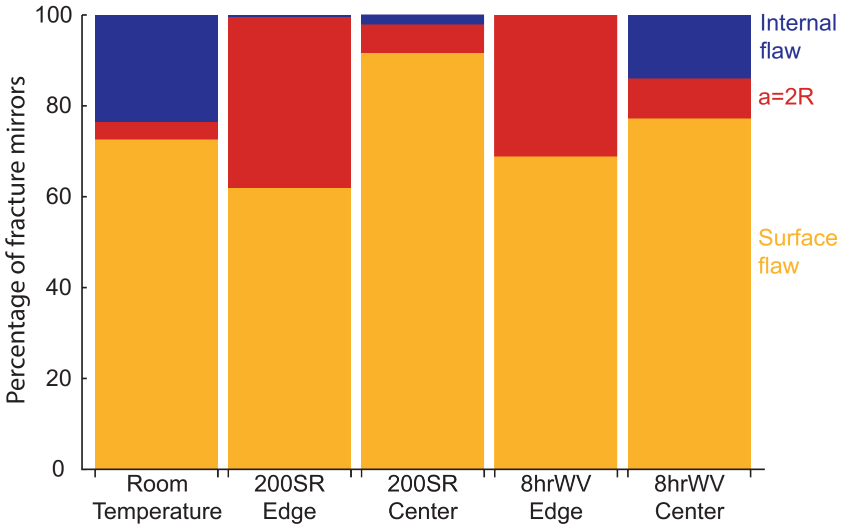

Figure 5.9: Percentage of fracture mirrors emanating from internal flaws, surface flaws, or with mirrors that encompass the entire fiber ($a = 2R$).

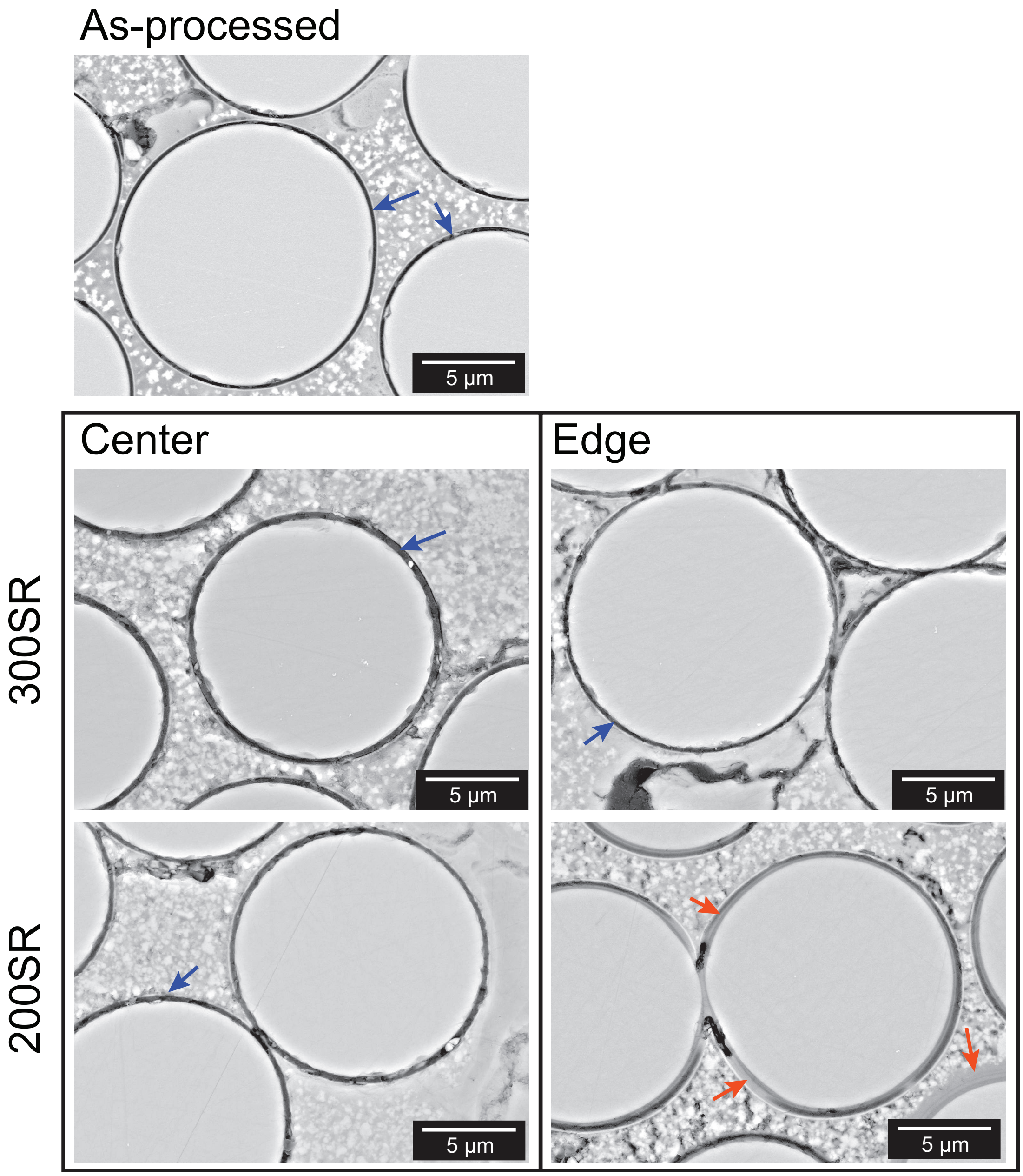

Figure 5.10: Electron micrographs of polished transverse cross-sections ∼ 3 mm below the fracture surfaces of the (a) room temperature tension sample, (b) 300SR sample and (c) 200SR sample. Blue arrows indicate intact BN fiber-coatings, red arrows indicate extensive oxide formation at the fiber/matrix interface.

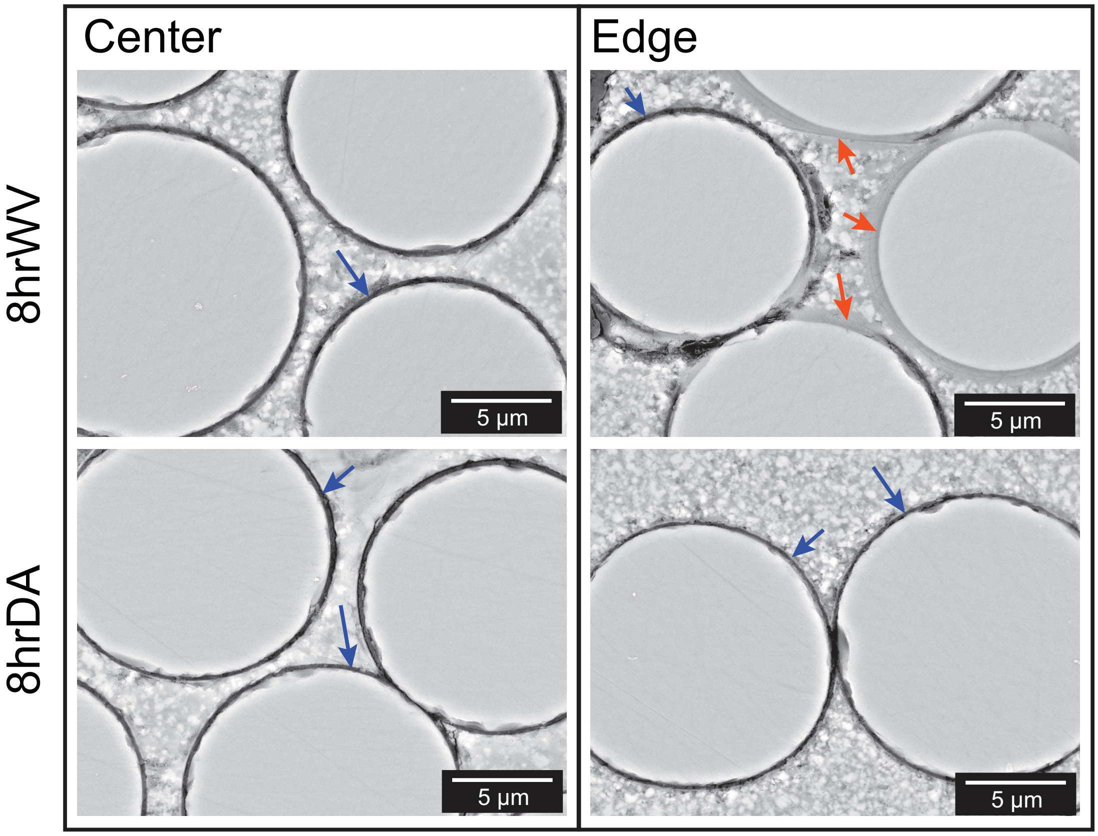

Figure 5.11: Electron micrographs of polished transverse cross-sections ∼ 3 mm below the fracture surfaces of the (a) 8hrWV sample and (b) 8hrDA sample. Blue arrows indicate intact BN fiber-coatings, red arrows indicate extensive oxide formation at the fiber/matrix interface.

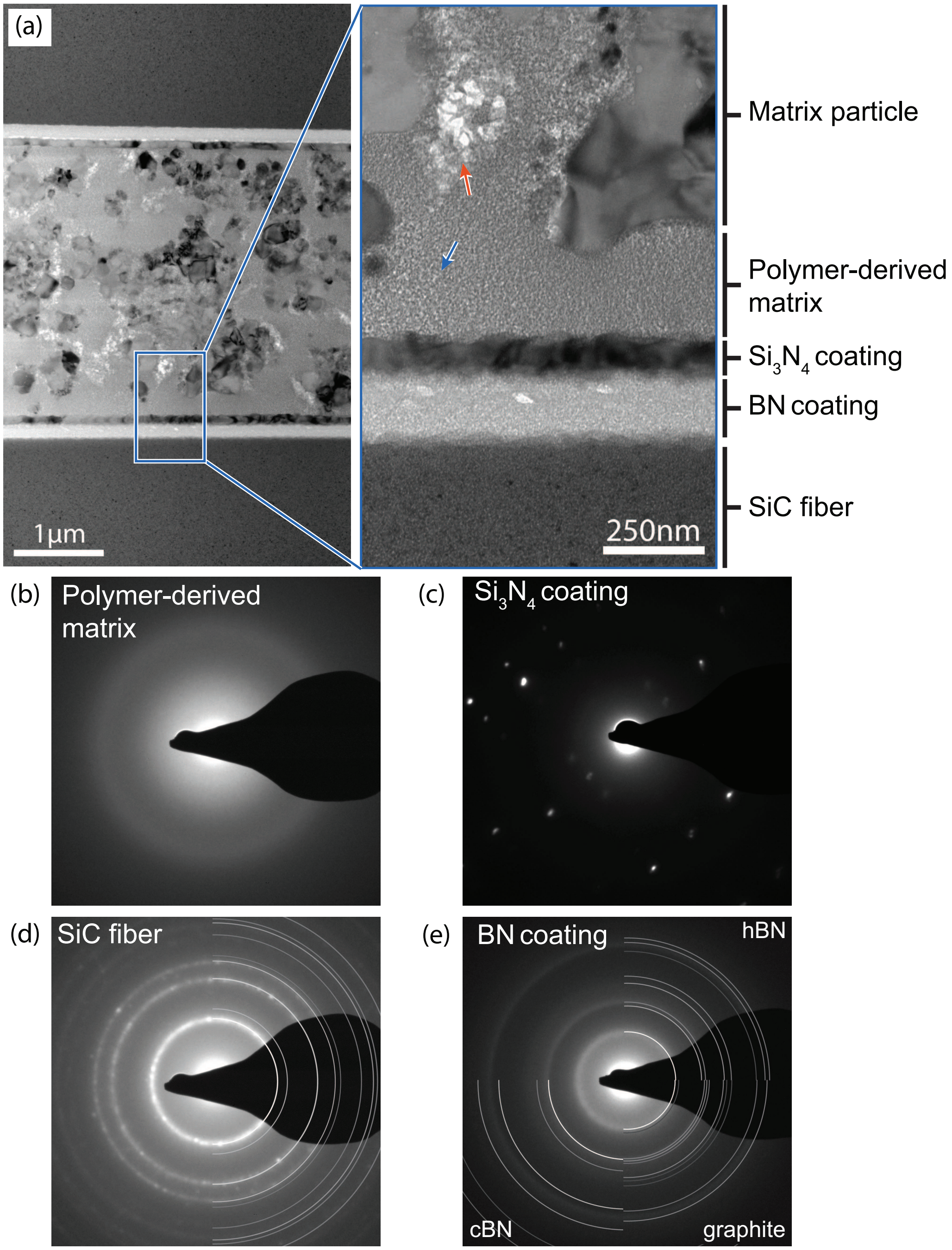

Figure 5.12: (a) TEM micrographs of as-processed COIC S200H indicating composite microstructure. Micro- and nano-sized porosity is indicated by the red and blue arrows, respectively. (b-e) SAED patterns for the different constituents of the composite.

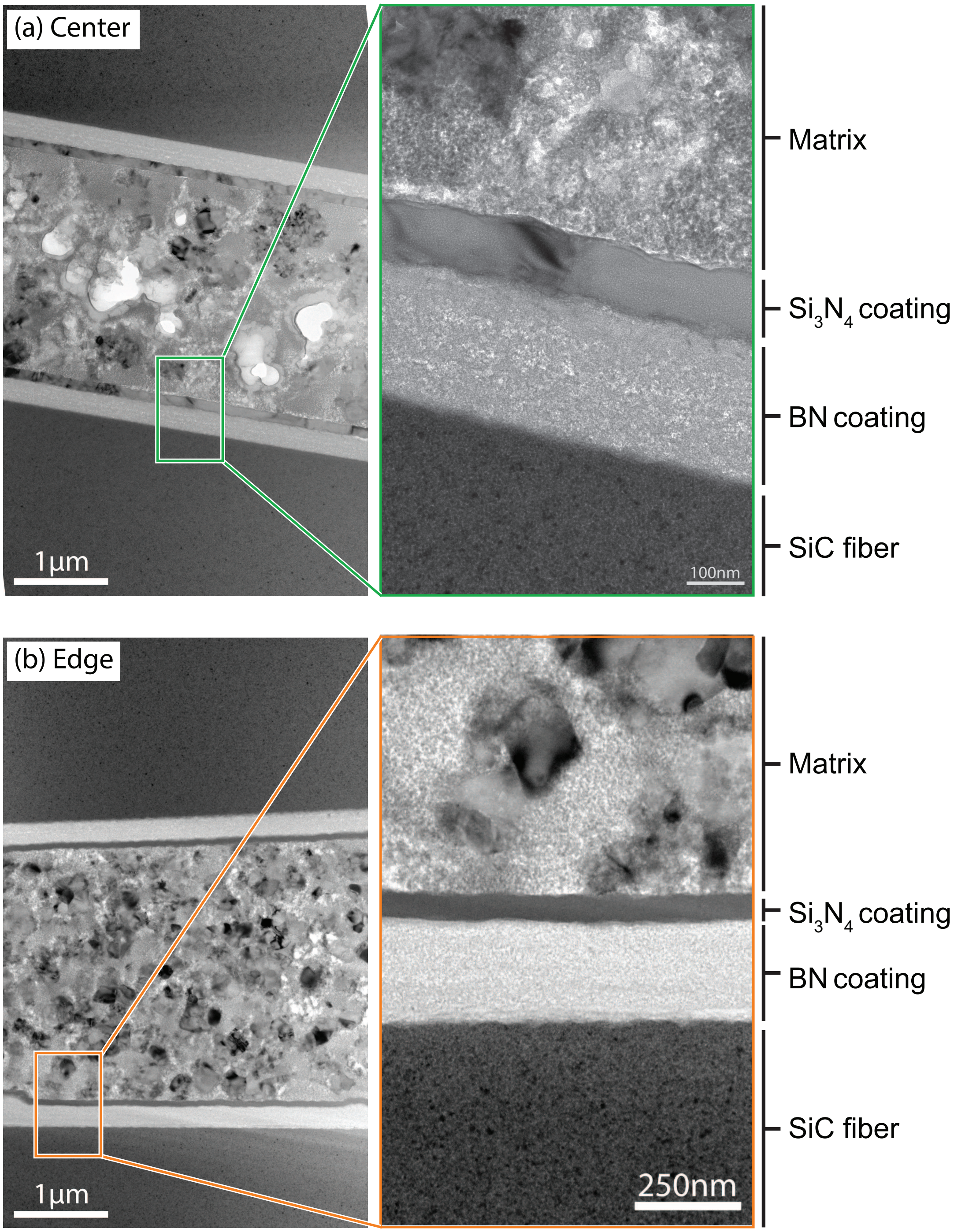

Figure 5.13: TEM micrographs from (a) the edge and (b) the center of the 8hrDA sample.

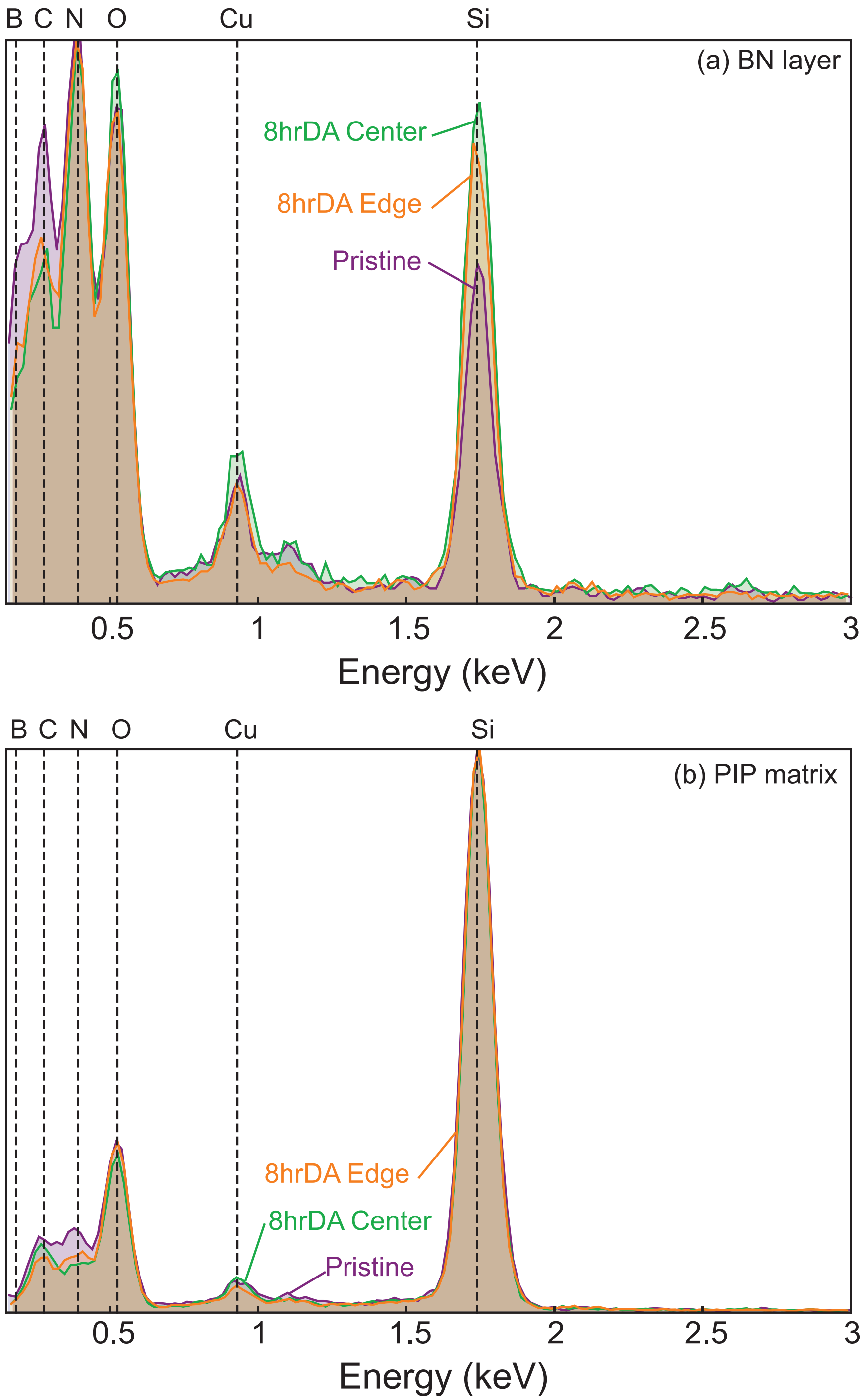

Figure 5.14: EDS spectra of (a) the BN layer and (b) the PIP-derived matrix for the 8hrDA sample.

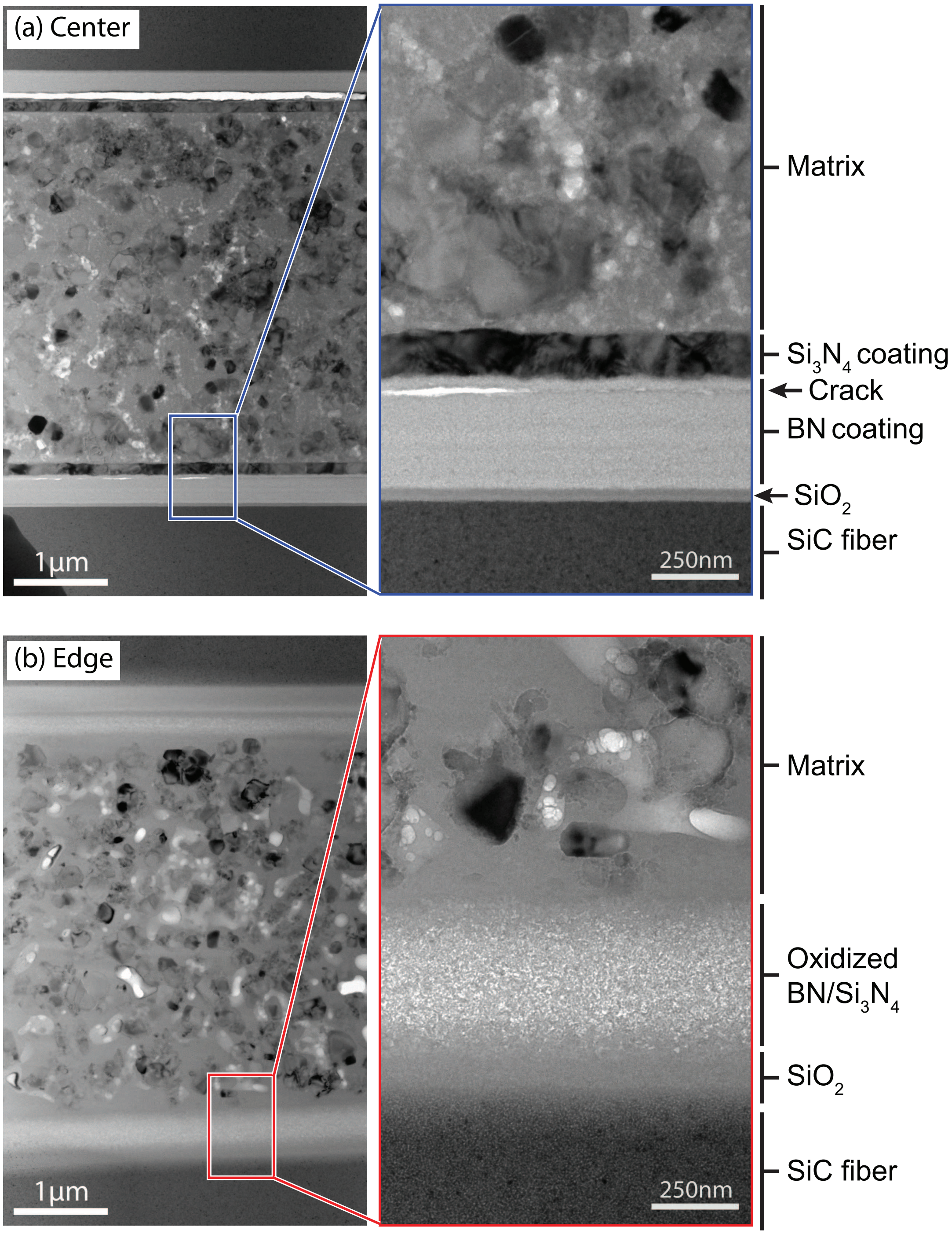

Figure 5.15: TEM micrographs from (a) the edge and (b) the center of the 200SR sample.

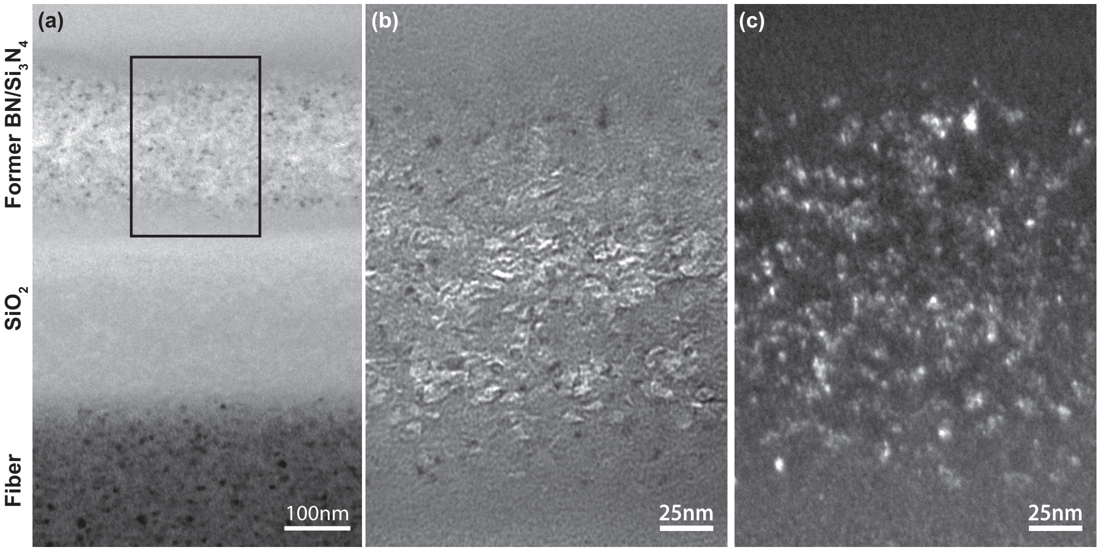

Figure 5.16: Additional detail of the fiber interphase region near the edge of the 200SR sample. The box in (a) indicates the approximate location of the higher magnification (b) bright field and (c) dark field images of the former BN/Si_3N_4 interlayer. The brightest features in (b) are presumed to be pores in the oxide while the bright particles in (c) are presumably unoxidized BN grains.

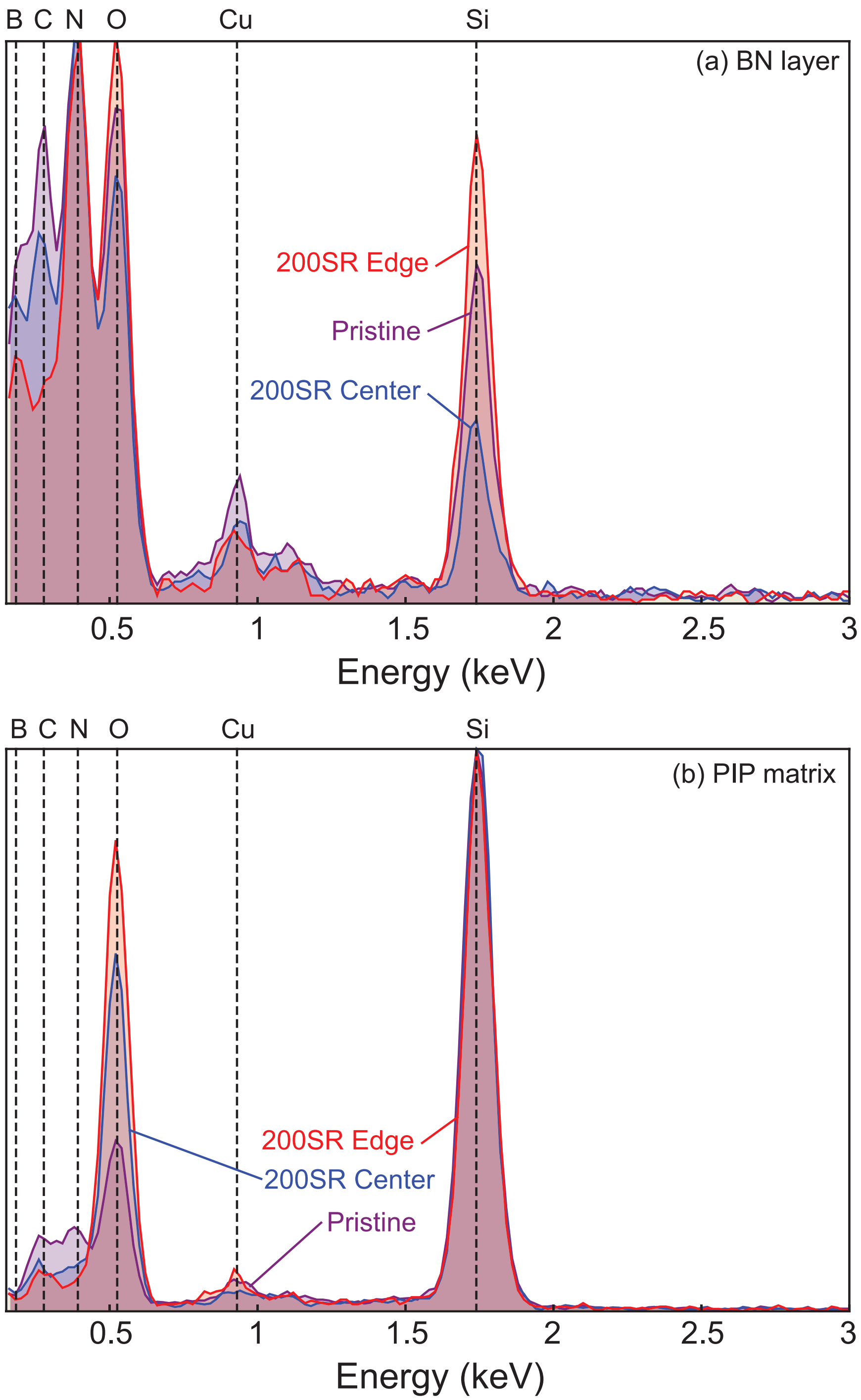

Figure 5.17: EDS spectra of (a) the BN layer and (b) the PIP-derived matrix for the 200SR sample.

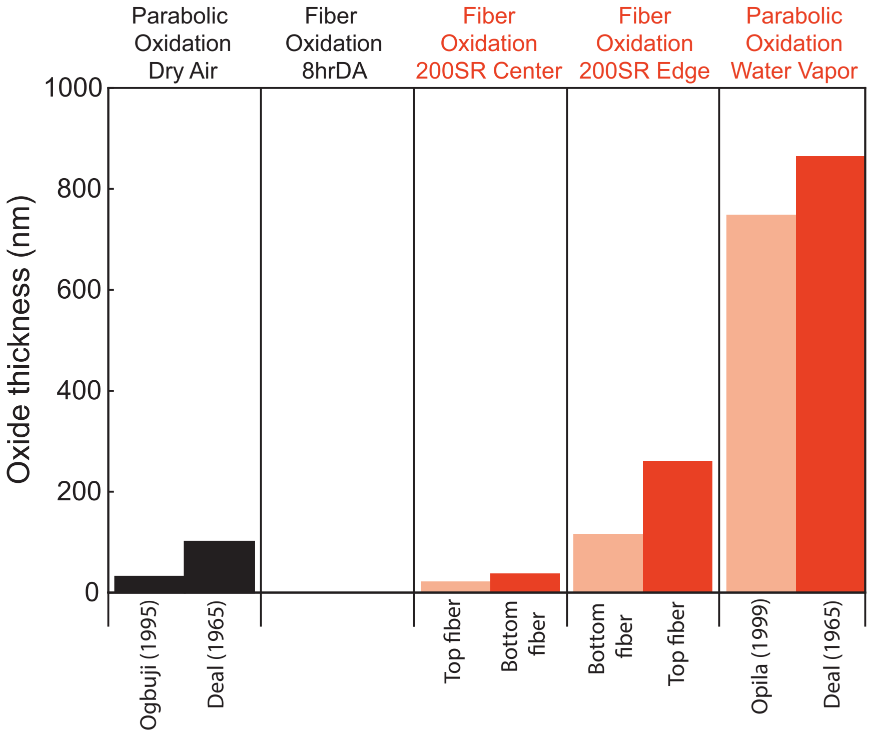

Figure 5.18: Comparison of predicted oxide thicknesses calculated using literature values of the parabolic oxidation rate of SiC and measurements made in the TEM. Parabolic rate constants for oxidation in dry air were measured by Ogbuji and Opila (1995) and Deal and Grove (1965). Parabolic rate constants for oxidation in water vapor were measured by Opila (1999) and Deal and Grove (1965).

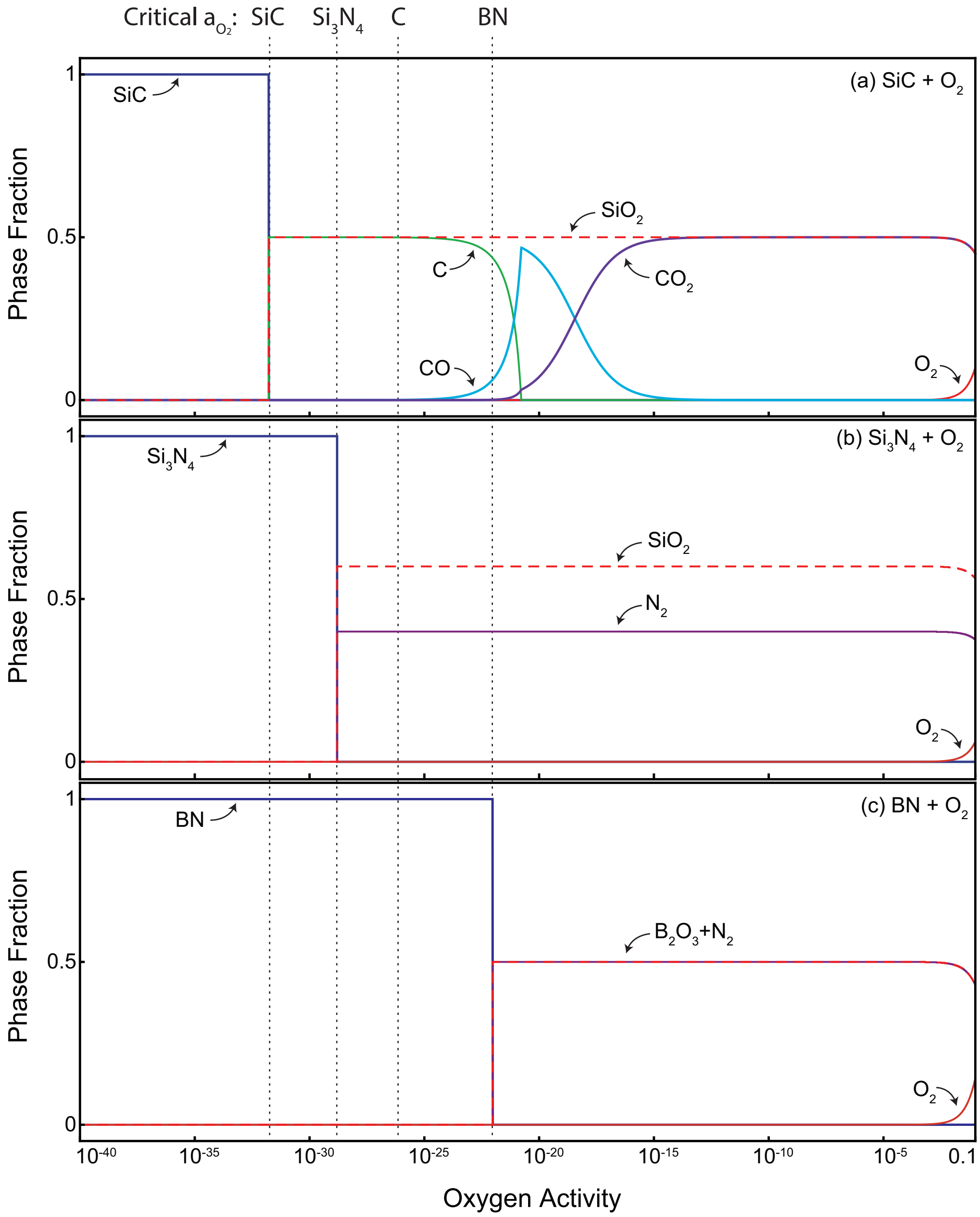

Figure 5.19: Thermodynamic calculations of the critical a_{O_2} needed to oxidize: (a) SiC, (b) Si_3N_4, and (c) BN.

Chapter 6

Conclusions

In the present study, the development and implementation of new characterization techniques (such as 3D DIC and high resolution optical scans) has enabled advancements in the understanding of the meso-scale structure of the fiber architecture and the mechanical and thermochemical response of woven CMCs. Through the judicious choice of the DIC parameters prior to testing, following the protocol developed in Chapter 2, DIC has been demonstrated to enable characterization of full-field strains and displacements with sub-tow resolution. This is of particular importance in woven CMCs where strain heterogeneities occur as a result of tow waviness in the weave architecture. Strain heterogeneities were found even in a seemingly ”flat” eight harness-satin weave. In addition, DIC has been demonstrated to allow for the the characterization of surface cracks that form at higher stresses. In these cases, the strains calculated near the cracks are non-physical in nature and DIC results are more meaningful when presented in terms of displacement discontinuities. Procedures have been developed to discern the location of cracks and to measure their opening displacement profiles.

Predictions from the meso-scale finite element model developed in Chapter 3, indicate that stress and strain concentrations in woven CMCs develop in response to bending and straightening of the axial tows at the crossovers. In unconstrained plies, bending and straightening are accommodated by out-of-plane displacement of the tows at the crossovers. This in turn leads to elevated stresses in the neighboring axial tows. The through-thickness constraint imposed by additional plies mitigates out-of-plane motion and reduces the stress elevations by 10–35 %.

Experimental results for an eight-harness satin SiC/SiCN composites with a PIP-derived matrix indicated substantial out-of-plane motion of the tows at the crossovers in the surface plies. As predicted by the model, tow straightening leads to elevated strains above the crossovers and elevated stresses in the neighboring axial tows. The elevated stresses result in preferential tow failure adjacent to the crossovers. The lack of through-thickness constraint is a result of residual porosity and micro-cracks inherent to the PIP-derived matrix. These processing defects are particularly prevalent in the matrix rich regions between the plies and are surmised to precipitate damage below the crossovers. The presence of heterogeneities in the matrix play an important role during damage initiation and evolution in woven CMCs.

The added complexity inherent to 3D woven CMCs leads to increased variability in the weave architecture. Using the characterization technique developed in Chapter 4, variations in a three-layer angle interlock C/SiC composite were found to consist of short-range and long-range components. Short-range variations are intrinsic to the weaving process and lead to variations (on the order of 2–5 %) in the local packing density of the tows. Long-range variations are attributable to deformation during handling after weaving. The three-layer angle interlock weave was found to be particularly susceptible to shear during handling. Shear deformations occur by sliding rotations of the tows at the crossovers.

The characterization technique was extended to panels with weave features, such as holes inserted through the weave, and systematically induced shear defects. The holes inserted through the weave only perturb the tows within the surrounding unit cell. Systematically induced shear defects result in correlated tow rotations over distances of 75–85 mm (10–11 unit cell lengths). During globally induced shear, tows rotate by $\sim 5^\circ$ before the weave "locksup" as a result of contact between neighboring tows. After lock-up, further deformation of the panel is enabled by extension of the weave locally along the warp direction. This results in a localized band of significant dilation ($\sim 9\,\%$ increase in the weft packing density) within the weave. During locally induced shear of a band two to three unit cells wide, the tows rotated by 10°. The additional rotation beyond 5° is accommodated by contraction of the weave in the warp direction.

The magnitude of the variations in the weave architecture were found to have minimal effect on the ultimate tensile strength and failure strain of fully dense composites tested by Shaw (2014). However, the local variations in tow packing density could affect the infiltration and densification of the matrix material within the composite. As indicated for the 8HSW SiC/SiCN composite, defects in the matrix affect the amount of constraint imposed on tow straightening. Therefore, the resulting variations in matrix density and pore distribution would influence the locations and loads for crack initiation.

The implications of the matrix microstructure on the intermediate temperature oxidation and embrittlement of SiC/SiC CMCs is particularly important. A preliminary experimental study of a PIP-derived SiC/SiCN CMC (presented in Chapter 5) indicated that oxidant ingress occurred at appreciable rates through the residual porosity and micro-cracks inherent to PIP-processing. This is in contrast to results in the literature for MI and CVI-based composites in which oxidant ingress only occurs after the initiation of matrix damage.

The transport of oxidants through the matrix microstructure was found to have substantial implications on the internal oxidation process. The findings are in contrast to the current understanding provided by the literature: that internal oxidation begins with the BN layer. Instead, internal oxidation occurs preferentially in the Si and C containing phases, then the Si_3N_4 fiber coating, with oxidation of the BN occurring last. This is a result of sluggish oxidant transport through the PIP-derived matrix microstructure, leading to reduced O_2 activity within the composite. Further study is needed to fully understand the role of O_2 activity during intermediate temperature oxidation. Embrittlement of the CMC studied here was found to be controlled by strength degradation in the fibers. It is surmised that strength degradation in the fibers is cause by slow-crack due to oxidation of free-C within the fibers, though further study is needed to verify this hypothesis.

Exposure to water vapor resulted in accelerated strength degradation and greater internal oxidation in comparison to exposure to dry air. Understanding the mechanisms by which water vapor versus O_2 diffuse through the matrix microstructure merits further investigation. Additionally, the role of internal oxidation on intermediate temperature embrittlement remains outstanding. It is unclear to what extent internal oxidation enables additional embrittlement mechanisms, or if accelerated oxidant ingress is the primary reason for accelerated embrittlement. In any case, the matrix microstructure has been shown to play an important role during intermediate temperature oxidation and embrittlement.

The interplay between the matrix microstructure, the weave structure, and the composite properties has been demonstrated in the present study. The results indicate the need for dense, strong matrices. The implementation of dense, strong matrices would mitigate the effects of weave architecture on stress and strain elevation by preventing tow straightening. Furthermore, dense matrices will inhibit oxidant ingress prior to the formation of matrix damage. Current routes for the production of dense matrices, namely MI and reactive-MI, are limited to use below 1400 °C due to the presence of residual Si. Current work focused on improving reactive-MI processing using eutectic Si alloys as well as understanding and controlling defect evolution during PIP-processing are promising first steps in the development of dense matrices for 1400 °C and beyond.

Appendix A

Statistical analysis and reconstruction algorithm

A.1 Statistical parameter set for DFT analysis

The stochastic variations in the amplitudes of the Fourier coefficients for mode s, associated with DFT analysis of weft tow density variations, $\delta_{xx}^{S}(x, y)$, transverse to the weft direction, are characterized by the mean and standard

---

This appendix is adapted from a peer-reviewed publication: M. N. Rossol, T. Fast, D. B. Marshall, B. N. Cox, and F. W. Zok. Characterizing In-Plane Geometrical Variability in Textile Ceramic Composites. *Journal of the American Ceramic Society*. Available at: `http://dx.doi.org/10.1111/jace.13275` deviation $M_A^{(y)}(s)$ and $\sigma_A^{(y)}(s)$ of the amplitude $A_m^{(y)}(s)$ and a correlation length κ_A derived from Pearsons correlation parameter $C_A(k)$ for amplitude values at pairs of scan lines separated by k:

$$\kappa_A^{(y)}(s) = \operatorname*{Mean}_{k \text{ small}} \left(\frac{1 - C_A^{(y)}(k)}{kd_y} \right)^{-1} \tag{A.1}$$

where d_y is the scan line spacing, weighted to sample the first few values of k only; and

$$C_A^{(y)}(k) = \frac{\sum_{m,m'} (A_m^{(y)}(s) - M_A^{(y)}(s))(A_{m'}^{(y)}(s) - M_A^{(y)}(s))/n_{mm'}}{\hat{\sigma}_A^{(y)}(s)\hat{\sigma'}_A^{(y)}(s)} \tag{A.2}$$

where the sum is over all $n_{mm'}$ pairs of scan lines m and m' for which $m - m' = k$ and the variances $\hat{\sigma}$ and $\hat{\sigma'}$ appearing in the denominator are formed using only those values of $A_m^{(y)}(s)$ or $A_{m'}^{(y)}(s)$ that appear in the numerator when forming the sum.

A.2 Random walk analysis of phase angles

Variations in the phase angle for mode s, again associated with DFT analysis of weft tow density variations transverse to the weft direction, are represented by a characteristic length λ_ϕ derived from a random walk analysis. The random walk is defined by

$$\begin{aligned} Prob\,\{\phi_m - \phi_{m-1} = \delta\phi\} &= 0.5 \\ Prob\,\{\phi_m - \phi_{m-1} = -\delta\phi\} &= 0.5 \end{aligned} \tag{A.3}$$

where ϕ_m is the value taken by the phase variable ϕ on the m^{th} of a sequence of scan lines. The values of ϕ are not confined to a single branch, e.g., $[0, 2\pi]$, but, since a Fourier transform comprises sums of trigonometric functions, the value of a transform is unchanged by $\phi \to \phi + 2\pi$. Further, if the values generated by the random walk are mapped onto $[0, 2\pi]$ by adding or subtracting multiples of $2pi$, the values will be uniformly distributed over $[0, 2\pi]$ for large enough walks.

For a given grid, the parameter available for calibration is the step size, $\delta\phi$, which is determined from the set of phase angles $\{\ \phi_m^{(y)}(s), m = 1, \ldots, n_y\ \}$. These data are first conditioned to remove any discontinuities introduced by their having been restricted to the interval $[0, 2\pi]$ by the algorithm used to compute the DFT:

$$\phi_m^{(y)}(s) \to \phi_m^{(y)}(s) + \Delta_m \tag{A.4}$$

where

$$\Delta_j = \begin{cases} \Delta_{j-1} + 2\pi & \text{if } \phi_s^{(j)} - \phi_s^{(j)} < \pi \\ \Delta_{j-1} - 2\pi & \text{if } \phi_s^{(j)} - \phi_s^{(j)} > \pi \\ \Delta_{j-1} & \text{otherwise} \end{cases} \tag{A.5}$$

and $\Delta_1 = 0$. (For example, the case might arise that on one grid point a phase of $2\pi - \varepsilon$ exists and on the next grid point a phase of $2\pi - \varepsilon'$. If the angles were restricted to $[0, 2\pi]$, then the latter phase would have been recorded as ε', leading to the appearance of a jump in value of approximately 2π. Such jumps would invalidate the following analysis.) Using the conditioned data, the average distance walked, d, between two data points separated by k (i.e., the average of the absolute value of the change in ϕ between two line scans) is compiled:

$$d(k) = \frac{1}{n_k} \sum_m |\phi^{(y)}_{m+k}(s) - \phi^{(y)}_m(s)| \tag{A.6}$$

where the summation is performed over all available pairs of points in $\{\ \phi^{(y)}_m(s), m = 1, \ldots, n_y\ \}$, with number $n_k = n_y - k - 1$. If the phases are indeed governed by a random walk, then the expectation value of $d(k)$ is given by (wol)

$$\langle d(k) \rangle = \delta\phi \cdot ff(k) \tag{A.7}$$

where

$$ff(k) = \begin{cases} \frac{(k-1)!!}{(k-2)!!} & n \text{ even} \\ \\ \frac{k!!}{(k-1)!!} & n \text{ odd} \end{cases} \tag{A.8}$$

with$X!!$ indicating the double factorial $X(X-2)(X-4)\ldots 1$ with $0!! = 1$. The step size of the random walk is therefore calibrated from the data by fitting the experimental values for $d(k)$ according to

$$\delta\phi = \frac{\sum_k w_k \frac{d(k)}{ff(k)}}{\sum_k w_k} \tag{A.9}$$

where the weight factors $w_k = n_y - k - 1$. Finally, the deduced value $\delta\phi$ is normalized by the distance δ_y between line scans on the experimental specimen to yield the characteristic length

$$\kappa_{\phi}^{(y)}(s) = 1/\frac{\delta\phi}{\delta y} \tag{A.10}$$

Formulae for the Fourier decomposition of the warp packing density $\delta_{yy}^{S}(x, y)$ in the y-direction can be obtained from the preceding analysis by permuting x and y in all subscripts and superscripts. The resulting complex Fourier coefficients have amplitudes $A_m^{(x)}(s)$ possessing mean $M_A^{(x)}(s)$, standard deviation $\sigma_A^{(x)}(s)$ and correlation length $\kappa_A^{(x)}(s)$; and phase angles $\phi_m^{(x)}(s)$ possessing characteristic length $\kappa_{\phi}^{(x)}(s)$.

A.3 Reconstruction algorithm - generating virtual specimens

Virtual replicas of the experimentally measured stochastic textile are generated by the Monte Carlo method (Metropolis and Ulam, 1949) using the statistical information described above. To generate positional variations for any genus of tows, the reconstruction algorithm generates instantiations of the amplitudes and phases of the Fourier components for a sequence of scan lines normal to the tow direction. This is done by progressing from one member of the sequence of scan lines to the next, using a Markov Chain algorithm developed in (Blacklock et al., 2012) to generate amplitude values and the random walk model described in Section A.2 to generate phase values. The Markov Chain is governed by a Probability Transition Matrix (PTM), which is calibrated separately for each Fourier component s using the prescribed values of the mean and standard deviation, e.g., $M_A^{(y)}(s)$ and $\sigma_A^{(y)}(s)$ for weft deviations, as described in (Blacklock et al., 2012). The random walk is governed by Eqn. (A.3). The process of generating amplitude values for the sequence of scan lines is initiated at the first scan line by choosing a value for the amplitude that is weighted by a normal distribution function with mean and standard deviation, e.g., $M_A^{(y)}(s)$ and $\sigma_A^{(y)}(s)$. The process of generating phase angles is initiated by choosing a phase value for the first scan line that is weighted by a uniform distribution over $[0, 2\pi]$.

When the amplitudes and phases have been generated for all Fourier components, the variations of δ_{xx}^S, etc., along the scan lines is found by an inverse DFT. Given these spatial derivatives, the positional deviations of the tows are found by integrating over the specimen from a chosen origin.

The positional deviations describe only the deviations of tows where they appear on the outer surfaces of the specimen. However, for thin specimens typical of textile ceramic matrix composites (Marshall and Cox, 2008), this information, when used in conjunction with the reconstruction algorithm for unit-cell scale deviations described in (Blacklock et al., 2012) and (Rinaldi et al., 2012), should suffice to generate positional deviations for the entire 3D fabric.

References

URL `http://mathworld.wolfram.com/RandomWalk1-Dimensional.html.`

G. Anzelotti, G. Nicoletto, and E. Riva. Mesomechanic strain analysis of twill-weave composite lamina under unidirectional in-plane tension. *Composites Part A: Applied Science and Manufacturing*, 39(8):1294–1301, 2008.

J. Aveston, G. A. Cooper, and A. Kelly. Single and multiple fracture. In *The Properties of Fiber Composites*, pages 15–24. National Physical Laboratory, IPC Science and Technology Press Ltd., 1971.

S. Avril, M. Bonnet, A.-S. Bretelle, M. Grédiac, F. Hild, P. Ienny, F. Latourte, D. Lemosse, S. Pagano, E. Pagnacco, and F. Pierron. Overview of identification methods of mechanical parameters based on full-field measurements. *Experimental Mechanics*, 48(4):381–402, 2008.

H. Bale, M. Blacklock, M. R. Begley, D. B. Marshall, B. N. Cox, and R. O. Ritchie. Characterizing Three-Dimensional Textile Ceramic Composites Using Synchrotron X-Ray Micro-Computed-Tomography. *Journal of the American Ceramic Society*, 95(1):392–402, 2012.

G. Bao and Z. Suo. Remarks on crack-bridging concepts. *Applied Mechanics Reviews*, 45(8):355–366, 1992.

M. Z. Berbon, K. L. Rugg, M. S. Dadkhah, and D. B. Marshall. Effect of weave architecture on tensile properties and local strain heterogeneity in thin-sheet C-SiC composites. *Journal of the American Ceramic Society*, 85(8):2039–2048, 2002.

D. S. Beyerle, S. M. Spearing, and A. G. Evans. Damage mechanisms and the mechanical properties of a laminated 0/90 ceramic/matrix composite. *Journal of the American Ceramic Society*, 75(12):3321–3330, 1992.

D. S. Beyerle, S. M. Spearing, F. W. Zok, and A. G. Evans. Damage and failure in unidirectional ceramic matrix composites. *Journal of the American Ceramic Society*, 75(10):2719–2725, 1992.

C. Bisagni and C. Walters. Experimental investigation of the damage propagation in composite specimens under biaxial loading. *Composite Structures*, 85 (4):293–310, 2008.

M. Blacklock, H. Bale, M. Begley, and B. Cox. Generating virtual textile composite specimens using statistical data from micro-computed tomography:

1D tow representations for the Binary Model. *Journal of the Mechanics and Physics of Solids*, 60(3):451–470, 2012.

M. Bornert, F. Brémand, P. Doumalin, J.-C. Dupré, M. Fazzini, M. Grédiac, F. Hild, S. Mistou, J. Molimard, J.-J. Orteu, L. Robert, Y. Surrel, P. Vacher, and B. Wattrisse. Assessment of digital image correlation measurement errors: methodology and results. *Experimental Mechanics*, 49(3):353–370, 2009.

B. Budiansky, J. W. Hutchinson, and A. G. Evans. Matrix fracture in fiber-reinforced ceramics. *Journal of the Mechanics and Physics of Solids*, 34(2):167–189, 1986.

C. Cady, F. E. Heredia, and A. G. Evans. In-plane mechanical properties of several ceramic-matrix composites. *Journal of the American Ceramic Society*, 78(8):2065–2078, 1995.

J. G. Campbell and F. Murtagh. Automatic visual inspection of woven textiles using a two-stage defect detector. *Optical Engineering*, 37(9):2536–2542, 1998.

C.-h. Chan and G. K. H. Pang. Fabric Defect Detection by Fourier Analysis. *IEEE Transactions on Industry Applications*, 36(5):1267–1276, 2000.

G. S. Corman and K. L. Luthra. Silicon Melt Infiltrated Ceramic Composites (HiPerComp$^{\text{TM}}$). In N. Bansal, editor, *Handbook of Ceramic Composites*, chapter 5, pages 99–115. Kluwer Academic, NY, 2005.

B. N. Cox and G. Flanagan. Handbook of analytical methods for textile composites. NASA Contractor Report 4750, 1997.

B. N. Cox, W. C. Carter, and N. A. Fleck. A binary model of textile composites–I. Formulation. *Acta Metallurgica et Materialia*, 42(10):3463–3479, 1994.

B. N. Cox, H. A. Bale, M. Begley, M. Blacklock, B.-C. Do, T. Fast, M. Naderi, M. Novak, V. P. Rajan, R. G. Rinaldi, R. O. Ritchie, M. N. Rossol, J. H. Shaw, O. Sudre, Q. Yang, F. W. Zok, and D. B. Marshall. Stochastic virtual tests for high-temperature ceramic matrix composites. *Annual Review of Materials Research*, 44(1):479–529, 2014.

W. A. Curtin. Theory of mechanical properties of ceramic-matrix composites. *Journal of the American Ceramic Society*, 74(11):2837–2845, 1991.

W. A. Curtin. Stochastic damage evolution and failure in fiber-reinforced composites. volume 36 of *Advances in Applied Mechanics*, pages 163–253. Elsevier, 1999.

S. Daggumati, E. Voet, W. Van Paepegem, J. Degrieck, J. Xu, S. V. Lomov, and I. Verpoest. Local strain in a 5-harness satin weave composite under static tension: Part I — experimental analysis. *Composites Science and Technology*, 71(8):1171–1179, 2011.

B. E. Deal and A. S. Grove. General Relationship for the Thermal Oxidation of Silicon. *Journal of Applied Physics*, 36(12):3770–3778, 1965.

D. Dietrich, S. Stockel, and G. Marx. XPS investigations on boron nitride fibre coatings prepared by chemical vapour deposition in comparison to their hydrolytic rate. *Fresenius' Journal of Analytical Chemistry*, 361:653–655, 1998.

A. J. Eckel, J. D. Cawley, and T. A. Parthesarathy. Oxidation Kinetics of a Continuous Carbon Phase in a Nonreactive Matrix. *Journal of the American Ceramic Society*, 78(4):972–980, 1995.

R. Eldrid, L. Kaufman, and P. Marks. The 7FB: The next evolution of the F gas turbine. Technical report, GE Power Systems, Schenectady, NY, 2001.

C. Epstein. GE's Passport 20 Engine program is on schedule for 2016 entry into service, 2013. URL `http://www.ainonline.com/aviation-news/nbaa-convention-news/2013-10-22/ges-passport-20-engine-program-schedule-2016-entry-service`.

S. Flores, A. G. Evans, F. W. Zok, M. Genet, B. Cox, D. Marshall, O. Sudre, and Q. Yang. Treating matrix nonlinearity in the binary model formulation for 3D ceramic composite structures. *Composites Part A: Applied Science and Manufacturing*, 41(2):222 – 229, 2010.

P. Forio, F. Lavaire, and J. Lamon. Delayed Failure at Intermediate Temperatures (600700C) in Air in Silicon Carbide Multifilament Tows. *Journal of the American Ceramic Society*, 87(5):888–893, 2004.

P. F. Fuchs and Z. Major. Experimental determination of cohesive zone models for epoxy composites. *Experimental Mechanics*, 51(5):779–786, 2010.

W. Gauthier and J. Lamon. Delayed Failure of Hi-Nicalon and Hi-Nicalon S Multifilament Tows and Single Filaments at Intermediate Temperatures (500-800C). *Journal of the American Ceramic Society*, 92(3):702–709, 2009.

W. Gauthier, F. Pailler, J. Lamon, and R. Pailler. Oxidation of Silicon Carbide Fibers During Static Fatigue in Air at Intermediate Temperatures. *Journal of the American Ceramic Society*, 92(9):2067–2073, 2009.

W. H. Glime and J. D. Cawley. Stress Concentration Due to Fiber Matrix Fusion in Ceramic-Matrix Composites. *Journal of the American Ceramic Society*, 81 (10):2597–2604, 1998.

C. González and J. Llorca. Stiffness of a curved beam subjected to axial load and large displacements. *International Journal of Solids and Structures*, 42(5-6): 1537–1545, 2005.

H. Haddadi and S. Belhabib. Use of rigid-body motion for the investigation and estimation of the measurement errors related to digital image correlation technique. *Optics and Lasers in Engineering*, 46(2):185–196, 2008.

F. E. Heredia, J. C. Mcnulty, F. W. Zok, and A. G. Evans. Oxidation Embrittlement Probe for Ceramic-Matrix Composites. *Journal of the American Ceramic Society*, 78(8):2097–2100, 1995.

C.-Y. Hui, S. L. Phoenix, M. Ibnabdeljalil, and R. L. Smith. An exact closed form solution for fragmentation of Weibull fibers in a single filament composite with applications to fiber-reinforced ceramics. *Journal of the Mechanics and Physics of Solids*, 43(10):1551–1585, 1995.

D. Ivanov, S. Ivanov, S. Lomov, and I. Verpoest. Strain mapping analysis of textile composites. *Optics and Lasers in Engineering*, 47(3–4):360–370, 2009.

N. Jacobson, S. Farmer, A. Moore, and H. Sayir. High-Temperature Oxidation of Boron Nitride : I , Monolithic Boron Nitride. 98, 1999.

N. S. Jacobson, G. N. Morscher, D. R. Bryant, and R. E. Tressler. High-Temperature Oxidation of Boron Nitride : II , Boron Nitride Layers in Composites. *Journal of the American Ceramic Society*, 82(6):1473–1482, 1999.

N. S. Jacobson, E. J. Opila, and K. N. Lee. Oxidation and corrosion of ceramics and ceramic matrix composites. 5:301–309, 2001.

W. J. Jasper and H. Potlapalli. Image Analysis of Mispicks in Woven Fabric. *Textile Research Journal*, 65(11):683–692, 1995.

S. Kazemahvazi, J. Kiele, and D. Zenkert. Tensile strength of UD-composite laminates with multiple holes. *Composites Science and Technology*, 70(8):1280–1287, 2010.

X.-D. Ke, H. W. Schreier, M. A. Sutton, and Y. Q. Wang. Error assessment in stereo-based deformation measurements, Part II: Experimental validation of uncertainty and bias estimates. *Experimental Mechanics*, 51(4):423–441, 2011.

H. J. Kim and C. C. Swan. Voxel-based meshing and unit-cell analysis of textile composites. *International Journal for Numerical Methods in Engineering*, 56(7): 977–1006, 2003.

W. G. Knauss, Y. Huang, and I. Chasiotis. Mechanical measurements at the micron and nanometer scales. *Mechanics of Materials*, 35(3-6):217–231, 2003.

F. Lagattu, J. Brillaud, and M.-C. Lafarie-Frenot. High strain gradient measurements by using digital image correlation technique. *Materials Characterization*, 53(1):17–28, 2004.

J. Lamon and M. R'Mili. Resistance to Fatigue at Intermediate Temperatures in Air for SiCHi-Nicalon Fibers: Statistical Distributions of Lifetimes and Strength Degradation. *Journal of the American Ceramic Society*, 95(11):3613–3621, 2012.

D. Lecompte, A. Smits, S. Bossuyt, H. Sol, J. Vantomme, D. Van Hemelrijck, and A. M. Habraken. Quality assessment of speckle patterns for digital image correlation. *Optics and Lasers in Engineering*, 44(11):1132–1145, 2006.

S. V. Lomov, A. V. Gusakov, G. Huysmans, A. Prodromou, and I. Verpoest. Textile geometry preprocessor for meso-mechanical models of woven composites. *Composites Science and Technology*, 60(11):2083–2095, 2000.

S. V. Lomov, G. Huysmans, Y. Luo, R. S. Parnas, A. Prodromou, I. Verpoest, and F. R. Phelan. Textile composites: modelling strategies. *Composites Part A*, 32(10):1379–1394, 2001.

S. V. Lomov, D. S. Ivanov, I. Verpoest, M. Zako, T. Kurashiki, H. Nakai, J. Molimard, and A. Vautrin. Full-field strain measurements for validation of meso-FE analysis of textile composites. *Composites Part A: Applied Science and Manufacturing*, 39(8):1218–1231, 2008.

K. Mak, P. Peng, and K. Yiu. Fabric defect detection using morphological filters. *Image and Vision Computing*, 27(10):1585–1592, 2009.

D. B. Marshall and B. N. Cox. Integral Textile Ceramic Structures. *Annual Review of Materials Research*, 38(1):425–443, 2008.

N. Metropolis and S. Ulam. The Monte Carlo Method. *Journal of the American Statistical Association*, 44(247):335–341, 1949.

K. L. More, K. S. Ailey, R. a. Lowden, and H. T. Lin. Evaluating the effect of oxygen content in BN interfacial coatings on the stability of SiC / BN / SiC composites. *Composites Part A: Applied Science and Manufacturing*, 30:463–470, 1999.

G. N. Morscher. Tensile Stress Rupture of SiCf / SiCm Minicomposites with Carbon and Boron Nitride Interphases at Elevated Temperatures in Air. *Journal of the American Ceramic Society*, 80(8):2029–2042, 1997.

G. N. Morscher and J. D. Cawley. Intermediate temperature strength degradation in SiC / SiC composites. *Journal of the European Ceramic Society*, 22: 2777–2787, 2002.

G. N. Morscher, J. Hurst, and D. Brewer. Intermediate-Temperature Stress Rupture of a Woven Hi-Nicalon, BN-Interphase, SiC-Matrix Composite in Air. *Journal of the American Ceramic Society*, 83(6):1441–1449, 2000.

R. Naslain. Design, preparation and properties of non-oxide {CMCs} for application in engines and nuclear reactors: an overview. *Composites Science and Technology*, 64(2):155 – 170, 2004.

O. Nazarian and F. W. Zok. Constitutive model for the shear response of Dyneema® fiber composites. *Composites Part A: Applied Science and Manufacturing*, 24:73–81, 2014.

N. N. Nemeth, S. Mital, and J. Lang. Evaluation of solid modeling software for finite element analysis of woven ceramic matrix composites. Technical Report NASA/TM-2010-216250, E-17237, 2010.

G. Nicoletto, G. Anzelotti, and E. Riva. Mesoscopic strain fields in woven composites: experiments vs. finite element modeling. *Optics and Lasers in Engineering*, 47(3-4):352–359, 2009.

L. U. J. T. Ogbuji. A Pervasive Mode of Oxidative Degradation in a SiC SiC Composite. *Journal of the American Ceramic Society*, 81(11):2777–2784, 1998.

L. U. J. T. Ogbuji. Pest-resistance in SiC / BN / SiC composites. *Journal of the European Ceramic Society*, 23:613–617, 2003.

L. U. J. T. Ogbuji and E. J. Opila. A Comparison of the Oxidation Kinetics of SiC and Si3N4. *Journal of The Electrochemical Society*, 142(3):925–930, 1995.

E. J. Opila. Oxidation Kinetics of Chemically Vapor-Deposited Silicon Carbide in Wet Oxygen. *Journal of the American Ceramic Society*, 77(3):730–736, 1994.

E. J. Opila. Variation of the Oxidation Rate of Silicon Carbide with Water-Vapor Pressure. *Journal of the American Ceramic Society*, 82(3):625–636, 1999.

J.-J. Orteu, T. Cutard, D. Garcia, E. Cailleux, and L. Robert. Application of stereovision to the mechanical characterisation of ceramic refractories reinforced with metallic fibres. *Strain*, 43(2):96–108, 2007.

M. Pankow, B. Justusson, A. Salvi, A. M. Waas, C.-F. Yen, and S. Ghiorse. Shock response of 3D woven composites: an experimental investigation. *Composite Structures*, 93(5):1337–1346, 2011.

S. Patil and B. Ravi. Voxel-based representation, display and thickness analysis of intricate shapes. Computer Aided Design and Computer Graphics, 2005. Ninth International Conference on, IEEE, 2005.

E. Pippel, J. Woltersdorf, D. Dietrich, S. Stöckel, K. Weise, and G. Marx. CVD-coated boron nitride on continuous silicon carbide fibres: Structure and nanocomposition. *Journal of the European Ceramic Society*, 20:1837–1844, 2000.

L. Qin, Z. Zhang, X. Li, X. Yang, Z. Feng, Y. Wang, H. Miao, L. He, and X. Gong. Full-field analysis of shear test on 3D orthogonal woven C/C composites. *Composites Part A*, 43(2):310–316, 2012.

G. D. Quinn. Guidelines for Measuring Fracture Mirrors. In J. R. Varner, G. D. Quinn, and M. Wightman, editors, *Fractography of Glasses and Ceramics V: Ceramic Transactions, Volume 199*, pages 163–187. John Wiley & Sons, Inc., Hoboken, NJ, 2007.

V. P. Rajan and F. W. Zok. Matrix cracking of fiber-reinforced ceramic composites in shear. *Journal of the Mechanics of Physics of Solids, in Press*, 2014.

V. P. Rajan, M. N. Rossol, and F. W. Zok. Optimization of Digital Image Correlation for High-Resolution Strain Mapping of Ceramic Composites. *Experimental Mechanics*, 52(9):1407–1421, 2012.

V. P. Rajan, J. H. Shaw, M. N. Rossol, and F. W. Zok. An elastic-plastic constitutive model for ceramic composite laminates. *Composites Part A*, 66:44–57, 2014.

C. Ramault, A. Makris, D. Van Hemelrijck, E. Lamkanfi, and W. Van Paepegem. Comparison of different techniques for strain monitoring of a biaxially loaded cruciform specimen. *Strain*, 2010.

W. S. Rasband. ImageJ, U.S. National Institutes of Health, Bethesda, Maryland, USA. URL `http://imagej.nih.gov/ij/,1997-2011`.

R. G. Rinaldi, M. Blacklock, H. Bale, M. R. Begley, and B. N. Cox. Generating virtual textile composite specimens using statistical data from micro-computed tomography: 3D tow representations. *Journal of the Mechanics and Physics of Solids*, 60(8):1561–1581, 2012.

L. Robert, F. Nazaret, T. Cutard, and J.-J. Orteu. Use of 3-D digital image correlation to characterize the mechanical behavior of a fiber reinforced refractory castable. *Experimental Mechanics*, 47(6):761–773, 2007.

D. M. Rubin. A simple autocorrelation algorithm for determining grain size from digital images of sediment. *Journal of Sedimentary Research*, 74(1):160–165, 2004.

H. W. Schreier and M. A. Sutton. Systematic errors in digital image correlation due to undermatched subset shape functions. *Experimental Mechanics*, 42(3): 303–310, 2002.

H. W. Schreier, J. R. Braasch, and M. A. Sutton. Systematic errors in digital image correlation caused by intensity interpolation. *Optical Engineering*, 39 (11):2915–2921, 2000.

J. H. Shaw. *Effects of Fiber Architecture on Damage and Failure in C/SiC Composites*. PhD thesis, University of California Santa Barbara, 2014.

J. H. Shaw, V. P. Rajan, M. Blacklock, and F. W. Zok. Towards a virtual test for C/SiC textile composites: Calibration of thermoelastic tow properties. *Journal of the American Ceramic Society*, 97(4):1209–1217, 2014.

J. H. Shaw, M. N. Rossol, D. B. Marshall, and F. W. Zok. Effects of tow-scale holes on the mechanical performance of a 3d woven C/SiC composite. *Journal of the American Ceramic Society*, In Press, 2014.

M. A. Sutton, S. R. Mcneill, J. D. Helm, and Y. J. Chao. Advances in Two-Dimensional and Three-Dimensional Computer Vision. *Photomechanics, Topics Appl. Phys.*, 372(77):323–372, 2000.

M. A. Sutton, J. Yan, X. Deng, C.-S. Cheng, and P. Zavattieri. Three-dimensional digital image correlation to quantify deformation and crack-opening displacement in ductile aluminum under mixed-mode I/III loading. *Optical Engineering*, 46(5):1–16, 2007.

M. A. Sutton, J.-J. Orteu, and H. W. Schreier. *Image correlation for shape, motion, and deformation measurements*. Springer, 2009.

A. Vanaerschot, B. N. Cox, S. V. Lomov, and D. Vandepitte. Stochastic characterisation of the in-plane tow centroid in textile composites to quantify the multi-scale variation in geometry. International Union of Theoretical and Applied Mechanics, 2014.

Y.-Q. Wang, M. A. Sutton, X.-D. Ke, H. W. Schreier, P. L. Reu, and T. J. Miller. On error assessment in stereo-based deformation measurements, Part I: Theoretical developments for quantitative estimates. *Experimental Mechanics*, 51 (4):405–422, 2011.

K. Wood. Ceramic-matrix composites heat up. *High-Performance Composites*, 21 (6), 2013.

Z. Xia, Y. Zhang, and F. Ellyin. A unified periodical boundary conditions for representative volume elements of composites and applications. *International Journal of Solids and Structures*, 40(8):1907–1921, 2003.

Z. C. Xia and J. W. Hutchinson. Matrix cracking of cross-ply ceramic composites. *Acta Metallurgica et Materialia*, 42(6):1933–1945, 1994.

Z. C. Xia, R. R. Carr, and J. W. Hutchinson. Transverse cracking in fiber-reinforced, brittle matrix cross-ply composites. *Acta Metallurgica et Materialia*, 41(8):2365–2376, 1993.

J. Xu, B. N. Cox, M. A. McGlockton, and W. C. Carter. A binary model of textile composites—II. The elastic regime. *Acta Metallurgica et Materialia*, 43 (9):3511–3524, 1995.

W. Xu, F. W. Zok, and R. M. McMeeking. Model of Oxidation-Induced Fiber Fracture in SiC/SiC Composites. *Journal of the American Ceramic Society*, In Press, 2014.

Q. D. Yang and B. N. Cox. Predicting failure in textile composites using the binary model with gauge-averaging. *Engineering Fracture Mechanics*, 77(16): 3174–3189, 2010.

Q. D. Yang, K. L. Rugg, B. N. Cox, and D. B. Marshall. Evaluation of macroscopic and local strains in a three-dimensional woven C/SiC composite. *Journal of the American Ceramic Society*, 88(3):719–725, 2005.